



The Europa Imaging System (EIS) Investigation

E.P. Turtle¹ · A.S. McEwen² · G.W. Patterson¹ · C.M. Ernst¹ · C.M. Elder³ · K.A. Slack^{1,4} · S.E. Hawkins¹ · J. McDermott¹ · H. Meyer¹ · R. DeMajistre¹ · R. Espiritu¹ · H. Seifert¹ · J. Niewola¹ · M. Bland⁵ · M. Becker¹ · J. Centurelli¹ · G.C. Collins⁶ · P. Corlies⁷ · H. Darlington¹ · I.J. Daubar⁸ · C. Derr¹ · C. Detelich⁹ · E. Donald^{1,10} · W. Edens¹ · L. Fletcher¹¹ · C. Gardner¹ · F. Graham¹ · C.J. Hansen¹² · C. Haslebacher¹³ · A.G. Hayes⁹ · D. Humm¹ · T.A. Hurford⁴ · R.L. Kirk⁵ · N. Kutsop⁹ · W.J. Lees¹ · D. Lewis¹ · S. London¹ · A. Magner¹ · M. Mills² · A.C. Barr Mlinar¹² · F. Morgan¹ · F. Nimmo¹⁴ · A. Ocasio Milanese¹ · S. Osterman¹⁵ · C.B. Phillips³ · A. Pommerol¹³ · L. Prockter¹ · L.C. Quick⁴ · G. Robbins¹ · J.M. Soderblom⁷ · B. Stewart¹ · A. Stickle¹ · S.S. Sutton² · N. Thomas¹³ · I. Torres⁷ · O.J. Tucker⁴ · R.B. Van Auken^{1,2} · K.A. Wilk^{4,8}

Received: 5 May 2024 / Accepted: 4 October 2024

© The Author(s) 2024

Abstract

The Europa Imaging System (EIS) consists of a Narrow-Angle Camera (NAC) and a Wide-Angle Camera (WAC) that are designed to work together to address high-priority science objectives regarding Europa's geology, composition, and the nature of its ice shell. EIS accommodates variable geometry and illumination during rapid, low-altitude flybys with both framing and pushbroom imaging capability using rapid-readout, 8-megapixel (4k × 2k) detectors. Color observations are acquired using pushbroom imaging with up to six broadband filters. The data processing units (DPUs) perform digital time delay integration (TDI) to enhance signal-to-noise ratios and use readout strategies to measure and correct spacecraft jitter. The NAC has a $2.3^\circ \times 1.2^\circ$ field of view (FOV) with a 10- μ rad instantaneous FOV (IFOV), thus achieving 0.5-m pixel scale over a swath that is 2 km wide and several km long from a range of 50 km. The NAC is mounted on a 2-axis gimbal, $\pm 30^\circ$ cross- and along-track, that enables independent targeting and near-global ($\geq 90\%$) mapping of Europa at ≤ 100 -m pixel scale (to date, only $\sim 15\%$ of Europa has been imaged at ≤ 900 m/pixel), as well as stereo imaging from as close as 50-km altitude to generate digital terrain models (DTMs) with ≤ 4 -m ground sample distance (GSD) and ≤ 0.5 -m vertical precision. The NAC will also perform observations at long range to search for potential erupting plumes, achieving 10-km pixel scale at a distance of one million kilometers. The WAC has a $48^\circ \times 24^\circ$ FOV with a 218- μ rad IFOV, achieving 11-m pixel scale at the center of a 44-km-wide swath from a range of 50 km, and generating DTMs with 32-m GSD and ≤ 4 -m vertical precision. The WAC is designed to acquire three-line pushbroom stereo and color swaths along flyby ground-tracks.

Keywords Europa · Europa Clipper Mission · Icy satellite · Ocean world · Camera · Mapping · Plumes

Europa Clipper: A Mission to Explore Ocean World Habitability

Edited by Haje Korth, Bonnie J. Buratti and David Senske

Extended author information available on the last page of the article

1 Introduction

1.1 EIS Overview

The Europa Imaging System (EIS) onboard the Europa Clipper spacecraft combines a Narrow-Angle Camera (NAC) and a Wide-Angle Camera (WAC) to explore Europa and address high-priority science objectives for the Europa Clipper mission (Pappalardo et al. 2024, this collection). EIS is designed to make observations of Europa that will:

- constrain formation processes of landforms by characterizing geologic structures, units, and global cross-cutting relationships (e.g., Leonard et al. 2021; Daubar et al. 2024, this collection);
- identify relationships of surface landforms to subsurface structures and potential near-surface water (e.g., Schmidt et al. 2011) detected by ice-penetrating radar (Blankenship et al. 2024, this collection);
- investigate compositional variability among landforms and correlate composition between individual features and regional units (e.g., Becker et al. 2024, this collection);
- search for evidence of recent and current activity, including potential erupting plumes (e.g., Quick et al. 2013; Roth et al. 2014; Sparks et al. 2017; Jia et al. 2018; Daubar et al. 2024, this collection);
- constrain Europa's long-wavelength shape and ice-shell thickness (e.g., Nimmo et al. 2003a, 2007, 2011; Roberts et al. 2023, this collection);
- characterize surface clutter to aid interpretation of deep and shallow radar sounding (e.g., Blankenship et al. 2024, this collection); and
- characterize scientifically compelling landing sites and hazards by determining the nature of the surface at meter scales (e.g., Pappalardo et al. 2013; Hand et al. 2022; Phillips et al. *in review*).

EIS data will be used to generate a variety of geospatial data products, including Geographic Information System (GIS) compatible data products, cartographic and geologic maps; regional and high-resolution topographic models; color and photometric data products; a database of plume-search observations; and limb profiles, shape models, and control networks tied to radar altimetry.

The purpose of this paper is to document aspects of the EIS design and operations to provide a guide to the science community, including current and future participants in the Europa Clipper mission.

1.2 EIS Investigation Concept

NASA's 2014 call for Europa Clipper instrument investigation proposals described both orbital and multiple-flyby mission architectures. The major science objectives were accompanied by a reconnaissance goal to characterize scientifically compelling sites and hazards for a potential future landed mission to Europa. The candidate payload developed by the Science Definition Team (SDT) for the multiple-flyby mission included a wide-angle camera to map topography along the ground-track and a narrow-angle camera that could achieve 0.5-m pixel scale to address the reconnaissance goal. Although the camera investigations could have been proposed separately, we considered an integrated investigation with both cameras to be more efficient by taking advantage of common hardware developments, mission operations, data processing, and science analyses.

While an orbiter mission with a nadir-pointed camera could achieve global coverage at better than the few hundred m/pixel needed to map major surface features, the multiple-flyby mission could only map $\sim 30\%$ of Europa at such scales with a nadir-pointed camera. In addition, achieving high-resolution stereo mapping (for science as well as reconnaissance) with a nadir-pointed NAC would be impossible unless the mission plan was changed to point the spacecraft. Both limitations could be addressed by mounting the NAC telescope on a two-axis gimbal for independent pointing. This addition represented a significant increase in technical complexity and resources, but provided the benefits of near-global mapping and high-resolution stereo without operational complexity.

Known challenges for designing a camera for Europa Clipper included the high-radiation environment for hardware that cannot be located in the heavily shielded spacecraft vault and, in the case of the multiple-flyby mission, the need to image from greatly varying ranges and ground-track speeds. A framing camera like the Cassini Imaging Science Subsystem (ISS; Porco et al. 2004) or Galileo Solid State Imaging (SSI; Belton et al. 1992) is best for distant, long-exposure observations such as searching for plumes, whereas a pushbroom camera with time delay integration (TDI) like the Mars Reconnaissance Orbiter (MRO) High Resolution Imaging Science Experiment (HiRISE; McEwen et al. 2007) is needed to acquire very high-resolution images with a high signal-to-noise ratio (SNR) during low-altitude, high-speed flybys. The solution to accomplishing wide-ranging imaging objectives under rapidly changing observational geometries was to use complementary metal oxide semiconductor (CMOS) detectors combined with capable electronics that enable operational flexibility and are highly radiation tolerant. The NAC and WAC each use rolling shutter exposures to operate for either framing or pushbroom imaging.

Adding broadband stripe filters to the WAC focal-plane module (FPM) for pushbroom color imaging was part of the original proposal. The original NAC instrument concept did not include color filters due to concern about the potential impact of in-field scattered light for imaging faint plumes against Europa's bright limb. Following later analysis (see Sect. 4) that showed scattered light effects met requirements for imaging faint plumes, especially when Europa's bright limb is well away from the color stripes in the array, color filters identical to those for the WAC were added to the NAC FPM.

1.3 History and Key Technology Development

The challenges of (1) acquiring both distant images in framing mode and fast low-altitude flyby images in pushbroom mode with TDI, and (2) designing for Jupiter's high radiation environment, including transient noise, are met with new CMOS detectors with active pixel sensors (Korendyke et al. 2013; Janesick et al. 2014). The extremely fast detector readout also limits transient radiation noise during imaging. Technology development needed for a Europa mission was supported via NASA's Planetary Instrument Definition and Development Program (PIDDP), NASA's Instrument Concepts for Europa Exploration (ICEE) Program, and Johns Hopkins Applied Physics Laboratory (APL) internal research and development (IRAD). EIS technology development included the stitching process enabling larger detector arrays ($2k \times 4k$) needed to achieve the field of view (FOV) of the WAC for ground-track stereo mapping and the NAC for reconnaissance coverage requirements.

Under the ICEE Program, development of the interface between the detector electronics and a precursor CMOS detector with heritage from the Solar Orbiter Heliospheric Imager (SoloHI) was performed to demonstrate framing and TDI modes, low read noise and the high readout rate necessary for Europa flyby operations (<15 e- root mean square (RMS) at 10 Mpixel/s). A digital readout board was fabricated, assembled, and tested. Field-programmable gate array (FPGA) designs for framing mode and the TDI mode logic were

used to demonstrate the imaging modes. Aspects of radiation modeling and thermal design were also matured under this program. Thinned and backside-illuminated (BSI) detectors also underwent radiation testing as a potential alternative to frontside illumination (FSI).

2 EIS Science Investigation

2.1 Overview

Europa Clipper Level-1 (L1) requirements and relevance to understanding the habitability of Europa are described by Pappalardo et al. (2024, this collection) with expanded discussions in the thematic working-group papers (Vance et al. 2023, this collection; Daubar et al. 2024, this collection; Becker et al. 2024, this collection; Roberts et al. 2023, this collection). Level-2 (L2) requirements that flow from Level-1 requirements and define the EIS datasets, are summarized in Table 1, along with Planning Guidelines that are used as less formal metrics in assessing the science return when evaluating trajectories and observation scenarios (Daubar et al. 2024, this collection). Mapping from the Level-1 and Level-2 requirements to the EIS datasets is organized related to science objectives and imaging scale (Table 2; Fig. 1), and some key EIS Measurement Requirements are summarized in Table 3. Measurement Requirements specific to each observation type are described in the relevant sections below.

2.2 Geology at Various Scales

2.2.1 Global Scale

EIS global-scale imaging is designed to meet the Level-1 requirement to map at least 80% of the surface at pixel scales ≤ 100 m. Galileo images (Belton 2000) demonstrated that this imaging scale is excellent for geologic studies of Europa's landforms whereas lower resolution images miss many key surface features. However, Galileo mapped less than 16% of Europa at better than 900-m pixel scale, and less than 0.6% at better than 200-m pixel scale (Table 4).

The EIS global-scale dataset will be used to map cross-cutting relationships and interactions between endogenic and exogenic (impact crater) geologic structures, which will also inform the relative ages of surface features. Global imaging at these scales will enable complete characterization of the population of impact craters larger than 1 km in diameter. The dataset includes observations of surface morphology, structural geology, albedo, and color. Combined, the cameras will also acquire stereo imaging of at least 30% of Europa (required; current imaging plan achieves $> 70\%$), providing topography with a ground sample distance (GSD) of ≤ 300 m and vertical precision ≤ 50 m. GSD refers to the pixel scale of the DTMs, and is typically 3–4 \times the pixel scale of the source stereo images. This factor is chosen to ensure that the DTM grid oversamples the true horizontal resolution, which for stereo DTMs has been found to be as large as 10–20 image pixels (Kirk et al. 2021). The global-scale imaging dataset will also serve as a coordinate-controlled basemap for other datasets.

2.2.2 Regional Scale

The EIS regional-scale dataset will be used to investigate a representative variety of Europa's geological surface features to test hypotheses regarding their formation. Regional-scale data

Table 1 Level-1 and Level-2 Requirements and Planning Guidelines that flow to EIS datasets. Dataset designations: P = Primary; I = Independent; S = Supportive; E = Enhancing (Pappalardo et al. 2024, this collection)

Goal	L1 EIS Requirements	L2 EIS Requirements (<i>Planning Guidelines in italics</i>)	EIS datasets
Ice Shell & Ocean	Map the vertical subsurface structure in regions of potential surface-ice-ocean exchange to >3 km depth along globally distributed ground tracks achieving a total cumulative length ≥30,000 km.	(Although there are no formal L2 requirements, EIS observations support and enhance the following: shallow subsurface dataset; full depth subsurface exchange dataset; ice-ocean interface dataset; <i>tidal deformation dataset; gravity science dataset</i>)	<ul style="list-style-type: none"> • Radar sounding clutter characterization (S,E)
	Constrain our knowledge of the average thickness of the ice shell, and the average thickness and salinity of the ocean, each to ±50%.	<i>The geodesy dataset shall consist of ≥100 globally distributed control points at ≤50-m pixel scale with repeat coverage at different orbital phases, in order to constrain the amplitudes of forced librations and obliquity and thereby the thickness of the ice shell.</i>	<ul style="list-style-type: none"> • Geodesy (I,E)
Composition	Create a compositional map at ≤10-km spatial scale, covering ≥70% of the surface, sufficient to identify non-ice materials, especially organic compounds.	<i>The limb profile imaging dataset shall characterize the topography along the limb at ≤1-km pixel scale and distributed in longitude to measure long-wavelength static topography indicative of ice-shell thickness variations.</i>	<ul style="list-style-type: none"> • Limb profile (P,E)
	Characterize the composition of ≥0.3% of the surface, globally distributed at ≤300 m spatial scale, sufficient to identify non-ice materials, especially organic compounds.	(Although there are no formal L2 requirements, EIS observations support and enhance the following: global-scale infrared imaging spectroscopy dataset; <i>global-scale ultraviolet surface composition dataset; regional-scale infrared imaging spectroscopy dataset; regional-scale ultraviolet imaging spectroscopy dataset; shallow composition dataset.</i>)	<ul style="list-style-type: none"> • Recent-activity color (E) • Global-scale color (E) • Regional-scale color (E) • Small-scale color (E)
Geology	Produce a controlled photomosaic map of ≥80% of the surface at ≤100-m spatial scale.	The global-scale panchromatic and stereo DTM imaging datasets shall, in combination, consist of observations that characterize visible reflectance, morphology, and albedo of ≥80% of the surface at ≤100-m pixel scale, with associated topographic coverage to support radar sounding clutter characterization at ≤300-m horizontal scale and a vertical precision ≤50 m, in order to characterize endogenic structures, surface units, and the potential for shallow subsurface water, and to constrain formation processes, 3-dimensional (3D) structures, and history of geologic landforms.	<ul style="list-style-type: none"> • Global-scale panchromatic (P) • Global-scale stereo (E) • Global-scale color (E)

Table 1 (Continued)

Goal	L1 EIS Requirements	L2 EIS Requirements (<i>Planning Guidelines in italics</i>)	EIS datasets
<p>Characterize the surface at ≤ 25-m spatial scale across $\geq 5\%$ of the surface with global distribution, including measurements of topography at ≤ 15-m vertical across $\geq 1\%$ of Europa's surface.</p>	<p>The regional-scale panchromatic, color, and stereo DTM imaging datasets shall, in combination, consist of observations that characterize visible reflectance, morphology, albedo, and color of $\geq 5\%$ (30% for <i>Planning Guideline</i>) of the surface with global distribution at ≤ 25-m pixel scale, with associated topographic coverage at ≤ 100-m horizontal scale and a vertical precision ≤ 15 m across $\geq 1\%$ of the surface, in order to characterize endogenic structures, surface units, and the potential for shallow subsurface water, and to constrain formation processes, 3D structures, and history of geologic landforms.</p>	<p>The small-scale panchromatic and color imaging datasets shall, in combination, consist of observations that characterize visible reflectance, morphology, albedo, and color of globally distributed sites ≥ 10 km by ≥ 10 km in area at ≤ 10-m pixel scale, in order to characterize resurfacing and degradation by processes such as weathering and erosion as context for interpreting the local-scale imaging dataset.</p>	<ul style="list-style-type: none"> • Regional-scale panchromatic (P) • Regional-scale color (E) • Regional-scale stereo (P,E)
<p>Search for and characterize any current activity, notably plumes or thermal anomalies, in regions that are globally distributed.</p>	<p>The plume search imaging dataset shall consist of limb and terminator images obtained at high phase angle at a ≤ 10-km pixel scale across a range of longitudes and true anomalies in order to search for active plumes via forward scattering by entrained particles.</p>	<ul style="list-style-type: none"> • Plume search (P,I) 	<ul style="list-style-type: none"> • Recent activity color (P,I) • Recent activity photometry (P,E)

Geology

Current Activity

Table 2 Basic categories of EIS observations, pixel scales, and typical ranges to Europa. (*Planning Guidelines in italics*)

Dataset	Pixel Scale	NAC range (km)	WAC range (km)	Notes
Plume Search	≤10 km	≤1,000,000	≤45,800	Primarily framing
<i>Limb Profile (planning guideline)</i>	≤1 km (<i>gap fill: 2 km</i>)	≤100,000 (≤200,000)	≤4600 (≤9200)	<i>Primarily framing</i>
Recent Activity	≤500 m	≤50,000	≤2300	Mostly pushbroom (PB) color
Global-scale	≤100 m	≤10,000	≤450	NAC framing, WAC PB
<i>Geodesy (planning guideline)</i>	≤50 m (<i>gap fill ≤300-m</i>)	≤5000 (≤30,000)	≤230 (≤1400)	<i>Also gap fill for true anomaly (TA)</i>
Regional-scale	≤25 m	≤2500	≤115	NAC framing, WAC PB
Small-scale	≤10 m	≤1000	≤45	NAC & WAC PB
Local-scale	≤1 m	≤100	N/A	NAC PB, often stereo
REASON Clutter Characterization & Gravity Crossover	≤500 m (Steinbrügge et al. 2018)	1000–2000	<1000	NAC mapping and WAC & NAC stereo coverage

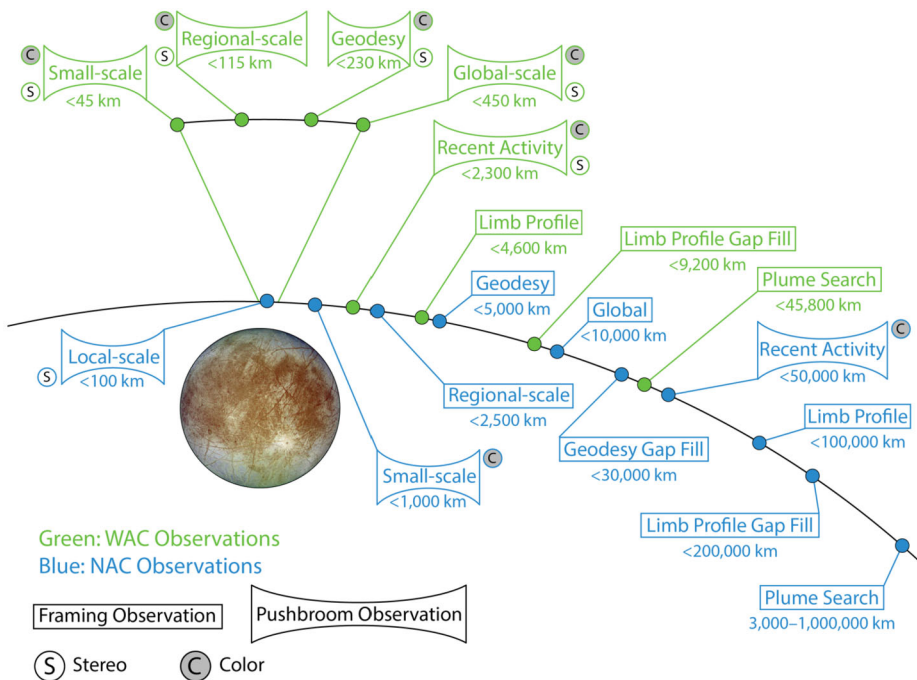


Fig. 1 EIS datasets. Sequence of observation types during a flyby as a function of range to Europa. Although only shown once here for clarity, observations are made both inbound and outbound depending on illumination. (Not to scale)

Table 3 Key EIS Measurement Requirements apply to multiple datasets. (See Sect. 3.3.2 for more information on the color filters)

Parameter	Requirement	Notes
SNR for panchromatic imaging of Europa surface ($I/F \geq 0.2$)	$\geq 50:1$	Some images achieve SNR 50:1 only after pixel averaging on the ground (margin exists on resolution requirements)
SNR for color imaging of Europa surface ($I/F \geq 0.2$)	$\geq 100:1$ RED, GRN, BLU	Some bandpasses (NUV, IMC) often achieve SNR only after pixel averaging on the ground (margin exists on resolution requirements)
	$\geq 20:1$ NAC NUV, IR1, IMC (1- μm)	(WAC optical throughput is low at short wavelengths due to radiation-tolerant glasses used for lenses – the cerium oxide added to increase radiation hardness absorbs NUV light (Centurelli et al. 2018, 2023))
SNR for imaging of faint plumes	$\geq 10:1$	Sufficient for detection of plumes with $I/F \geq 0.01$
Image smear (many image types)	< 10 microrad, 2-sigma, per axis	Less than 1 pixel of smear in $> 99\%$ of NAC image pixels
Stereo convergence angles	22–32 degrees	For required coverage; additional stereo coverage at smaller and larger convergence angles will be acquired
Image overlap for mosaics	> 100 pixels	To ensure sufficient match points for seamless mosaics and for geodesy

Table 4 Comparison of coverage of Europa from Galileo SSI to the planned coverage by EIS in the nominal mission (trajectory 21F31_V6 (Pappalardo et al. 2024, this collection))

Pixel scale	Galileo coverage	EIS requirement	Expected EIS coverage through flyby E49
≤ 1 m	none	≥ 18 sites (sites are ≥ 2 km \times 4 km)	70 sites
≤ 10 m	< 10 images	Panchromatic: ≥ 20 sites Color: ≥ 10 sites (sites are ≥ 10 km \times 10 km)	171 panchromatic sites 210 color sites
≤ 200 m	0.54%	$\geq 80\%$ at ≤ 100 m	90.1% at ≤ 100 m
≤ 900 m	15.3%	N/A	$> 95\%*$
≤ 6 km	82.4%	N/A	$\sim 100\%*$

*Depends on opportunities to acquire polar coverage

will be collected with pixel scales of ≤ 25 m (Table 2). The small amount of Galileo SSI coverage at better than 25 m pixel scale revealed relatively recent narrow surface fractures, as well as fine details of landforms observed at coarser resolution. Crater populations in Galileo images obtained at this scale revealed apparently paradoxical age relationships between cross-cutting features and crater density (Bierhaus et al. 2009). Substantially more coverage at this scale is necessary to understand the statistics of the primary and secondary crater populations on Europa and potentially target property effects on crater size. The requirement is to image $\geq 5\%$ of Europa's surface at this scale, with a planning guideline to achieve $\geq 30\%$ coverage. EIS coverage at regional scales during the prime mission is estimated to be $\geq 37.1\%$, exceeding the planning guideline.

A portion of the regional-scale dataset will be collected as overlapping images with convergence angles between 22° and 32° in order to derive stereo topography of Europa landforms. The WAC along-track FOV of 24° enables three-line (forward, nadir, and aft) stereo imaging in pushbroom mode, and the NAC uses the gimbal to target repeat framing images during a single flyby or on successive flybys with similar illumination. Regional-scale stereo imaging will be used to generate DTMs with $GSD \leq 100$ m and vertical precision ≤ 15 m, sufficient to characterize slopes and relief across individual landforms. At least 1.67% (required; current plan covers $>7\%$) of Europa's surface will be covered by regional-scale stereo images.

WAC imaging will cover $\sim 6\%$ of Europa at regional scale; WAC stereo and color pushbroom images are acquired at the same time (color imaging may be subject to detector readout data rate limitation at low altitudes). Color data at this scale will help to correlate ice-rich and ice-poor surfaces with specific parts of observed landforms, e.g., the interiors of fractures, exposed scarps, or material ponded in local topographic lows.

Regional-scale imaging is acquired at an altitude where the NAC may be used in either framing or pushbroom mode, based on the relative motion between the spacecraft and Europa. (At high altitudes, the relative motion is too slow for pushbroom imaging, and at low altitudes the motion is too fast for sufficient framing exposure times without smear.) The choice will trade off color coverage, which requires pushbroom imaging, and spatial coverage, for which framing is more efficient. Another consideration for regional-scale imaging is that framing imaging at this scale can also be used for the geodesy dataset (Sect. 2.4.2).

An important subset of the imaging at this scale is preview or look-ahead imaging. To target future small-scale and local-scale EIS images and MISE (Blaney et al. 2024, this collection) spectral cubes at sites of the most interest, it will be key to have coverage over the future ground-track at scales ≤ 25 m/pixel, at which there is currently extremely little coverage (Table 4). Such previews require careful planning, at least two orbits in advance, to use for targeting the NAC at areas along the ground-tracks of future flybys. Ideally, look-ahead coverage would include at least three colors; stereo look-ahead imaging would be a trade-off with more areal coverage.

2.2.3 Small Scale

At small scales, ≤ 10 m/pixel (Table 2), EIS will acquire panchromatic (clear) and color data to characterize visible reflectance, morphology, albedo, and color of globally distributed sites ≥ 10 km by ≥ 10 km in area. (The NAC cross-track FOV exceeds 10 km above 250-km range.) These data are intended to characterize resurfacing and degradation by space weathering and erosion processes and, where possible, to provide context for interpreting data acquired at local scales (Sect. 2.2.4). The requirement is to acquire ≥ 20 sites with panchromatic data and ≥ 10 sites with ≥ 3 color filters. At least three sites are to be acquired within each of the latitude bins of 90°N – 30°N , 30°N – 30°S , and 30°S – 90°S for both the anti- and sub-Jovian hemispheres. The goal will be to acquire as much data at this scale, and using as many available colors, as spacecraft data volume and SNR constraints will allow. Current planning includes imaging of 173 panchromatic sites and 215 color sites. These data are acquired primarily by the NAC at spacecraft altitudes of 1000 to 100 km, but can also be acquired with the WAC at altitudes of <46 km.

2.2.4 Local Scale

The EIS local-scale dataset will enable understanding of Europa's surface at the meter scale. Imaging at least 18 globally distributed sites at 1-m pixel scale or better is a Level-1 requirement (Table 1), with specification at Level-2 of site sizes of at least 2×4 km with stereo

GSD ≤ 4 m and vertical precision ≤ 0.5 m. These data will be used to interpret regolith, thermophysical, and erosion/weathering processes, as well as to reveal subsurface layering/structure. During the nominal mission, we anticipate being able to observe at least 73 sites at high resolution, with at least 34 of them in stereo. EIS will acquire multiple relevant datasets: high-resolution (< 1 m/pixel) images, DTMs, and information on the color and photometry via concurrent WAC context coverage. Any surface that is less modified by impact gardening, sputtering, and sublimation is likely to have been recently emplaced (Daubar et al. 2024, this collection). So, finding such locations is a high priority both for the habitability goal of the Europa Clipper mission and for future landed exploration. For Europa's average-age surface, we expect the small-scale structure to be dominated by impact gardening from secondary and sesquinary cratering (Zahnle et al. 2008); EIS will test that prediction. The local-scale data from EIS and other instruments can be used to test a range of other hypotheses about Europa. For example, recent mass wasting typically leaves characteristic deposits at the bases of steep slopes, and recently active tectonics could produce very small-scale cracks or other structures that have not yet been erased by impact gardening or other diffusive processes.

Depending on illumination and ground speed, the NAC can potentially acquire images down to a pixel scale of 0.25 m at 25-km altitude, although along-track summing to increase SNR may result in a ground sample dimension of 0.25 m (cross-track) \times 0.5–0.75 m (along-track). Such high-resolution images will reveal surface features such as blocks, craters, mounds, cracks, fine layering, and other structures. Regolith thickness can be estimated from the density of small craters (Hörz and Cintala 1997; Costello et al. 2018), block abundances around craters (Rennilson et al. 1966; Shoemaker and Morris 1970; Wilcox et al. 2005, Elder et al. 2019), and based on the morphology of craters that encounter a strength contrast between loose regolith and a strong substrate (e.g., Oberbeck and Quaide 1967; Bart 2014). The amount of imaging at ≤ 1 m/pixel will be limited by overall data volume, as well as the number of dayside Europa passes below 100 km altitude. On a flyby with the closest approach well below 100 km, acquisition of up to ~ 10 high-resolution NAC images may be possible. The NAC can acquire two-look stereo images by using the along-track gimbal (Sect. 3.4.1) when the altitude is as low as ~ 50 km (0.5 m/pixel), for production of DTMs with ~ 4 -m GSD and vertical precision ~ 0.5 m. If gimbal slew and settle performance exceeds requirements, NAC stereo below 50 km might be possible.

The NAC will typically not image in color below ~ 200 km altitude due to detector readout and electronics data rate limits; the WAC will acquire stereo images, and color when downlink rates allow, at $\sim 21\times$ coarser pixel scale than the NAC, down to 5.5 m/pixel at 25-km altitude. Color variations may correlate with fine-scale structures, enabling extrapolation or interpretations outside of NAC coverage. The WAC acquires continuous stereo coverage for DTMs ranging from ~ 20 to 80 m GSD and typically better than 5–20 m vertical precision from data acquired below 100 km altitude, which aids interpretation of the fine-scale structures and again may facilitate extrapolation to larger areas.

2.2.5 Reconnaissance for Future Missions

A lander or similar in-situ mission is a likely next step in Europa exploration following the Europa Clipper mission. Such a landed mission may or may not resemble the Europa Lander mission concept (Hand et al. 2022), but any such mission will have similar reconnaissance (recon) needs. Data collected by Europa Clipper will be critical for the identification and assessment of potential future landing sites, both for scientific value and landing/operational safety. The top-level requirements of the Europa Clipper investigations are well-aligned with the science needs for future exploration. The data needs for landing/operational

safety (measurements of slopes, detection/characterization of boulders, and surface roughness) are largely satisfied by the local-scale surface characterization requirements, but there are additional requirements on lighting angles and latitudes needed for the Europa Lander concept, which are captured by our Planning Guidelines for recon (see Phillips et al. [in review](#)).

Landing successfully on Europa requires two key datasets from EIS: wide-area stereo coverage at 10–20 m/pixel for terrain relative navigation (TRN), and high-resolution (<1 m/pixel) stereo data to assess landing hazards. EIS can provide such data simultaneously with the WAC for TRN and the NAC for hazards. In theory the NAC could be used for TRN in place of the WAC, but that would require a tour design with paired low (50–100 m) and high (1000–2000 m) altitude flybys over recon sites, which is not expected.

TRN would be used onboard the lander during the deorbit, descent, and landing to localize the spacecraft and precisely navigate to the planned landing site, e.g., Mars 2020 (Nelessen et al. [2019](#)) and OSIRIS-REx (referred to as Natural Feature Tracking; Lauretta et al. [2017, 2019](#)). EIS WAC stereo images obtained at ≤ 22 m/pixel scale and surrounding the landing region by ≥ 22 km on all sides of the landing ellipse will allow creation of a map that makes TRN possible for the ~ 200 -m-diameter landing region anticipated for a Europa lander. This small landing ellipse size increases the number of potential sites observable and improves the probability of finding landing areas that have both high science value and are also safe from an engineering perspective (Johnson et al. [2015](#)).

Landing safely on the surface of Europa will require assessments of local surface properties such as slope and vertical topographic relief (including abundances of blocks ≥ 1 m). Hazard assessments using MRO HiRISE have shown that 0.3-m/pixel images detect nearly 100% of hazards larger than 2-m diameter (Golombek et al. [2008](#)). Although many 1-m-scale boulders are detected, the counts are incomplete, much as crater counts are incomplete except for craters with diameters at least ~ 8 – 10 times larger than the pixel scale. Based on Golombek et al. ([2008](#)), we predict that 0.5–1.0 m/pixel EIS images will provide complete statistics on blocks larger than ~ 3 – 7 m diameter. Data for Earth and Mars facilitate extrapolation from the size-frequency distribution of boulders larger than 2-m diameter to accurately predict the abundance of 1-m boulders (Golombek and Rapp [1997](#)). However, it may not be safe to assume that the density of 1-m blocks on Europa can be predicted based on blocks larger than 3–7 m because of the different material properties and weathering processes on Europa compared to Earth and Mars. To address this limitation, a future Europa lander would likely use onboard hazard detection and avoidance (HDA), using LIDAR, to bridge the gap between Europa Clipper images and the lander's hazard tolerance capabilities. Terminal hazard avoidance has been demonstrated by China's lunar and Mars landings (Jiang et al. [2018](#); Liu et al. [2021](#)). Europa Clipper data from multiple investigations can be used to identify terrains with a high probability of sufficiently smooth areas, with the exact landing site to be located via HDA during descent.

There will be science objectives that require targeting of rough areas that are not likely to contain safe landing sites. We can expect debate about the relative priority of targeting for science vs. landing-site reconnaissance, although in many cases these objectives are compatible (for example, sites of recent activity). An extended Europa Clipper mission would provide opportunities for targeted, follow-on observations of potential landing sites. See Phillips et al. ([in review](#)) for a full discussion of the reconnaissance strategy for landing on Europa.

2.3 Recent Activity

2.3.1 Plume Search

Gas emission off Europa's limb detected by the Hubble Space Telescope (HST) at ultraviolet wavelengths suggested that Europa may have plumes extending hundreds of kilometers above the surface (Roth et al. 2014). Possible detections by Sparks et al. (2016, 2017) suggested plumes on the order of 50-km tall. More recently, ground-based observations by Paganini et al. (2020) suggest that plumes that are hundreds of kilometers tall may be the exception rather than the rule on Europa, in concert with previous plume searches in Galileo image data (Phillips et al. 2000) and modeling (Fagents et al. 2000; Quick et al. 2013), which suggest that plume activity on Europa may be small-scale and/or sporadic in nature. An initial survey using the James Webb Space Telescope (JWST) found no evidence for European plumes (Villaneuva et al. 2023). All plume data collected to-date are consistent with gas eruptions, so particulate content and altitudes thereof are unknown. EIS can detect scattering by small particles, but not transparent gas, unless excited (see below). A basic goal for EIS will be to search for plumes with particulates, and if they are detected to characterize their locations, properties, and eruption frequencies.

Owing to the broad range of possible plume geometries on Europa, several methods and a variety of viewing geometries will be used to search for plumes to maximize our chances of observing active venting on this enigmatic moon. These methods include: (1) imaging along Europa's terminator, (2) imaging of Europa's bright limb, especially at high phase angles, and (3) imaging during eclipses. Europa's plumes may be markedly different from those at Enceladus in terms of the amount of material erupted (Hansen et al. 2019), so the most effective detection methods for Europa's plumes may differ. For Enceladus, phase angles $>140^\circ$ were needed to confidently detect the erupting jets with Cassini ISS (Spitale et al. 2015); plumes on Io are also best seen and sometimes only seen at high phase angles (Geissler and McMillan 2008). Terminator and limb imaging with EIS will be undertaken at $60\text{--}170^\circ$ phase angles, and up to 180° phase angle during solar eclipses (when the spacecraft is in Europa's shadow), in order to search for irregularities along the limb or just beyond the day-night boundary. If enough particles are present then active plumes will manifest as bright areas above the limb and/or terminator. The particle size distribution is likely to be dominated by very small particles, so the highest phase angles are most promising, but we will also target lower phase angles to increase the cadence of the search, especially early in the mission. Although a bright plume beyond the terminator is smaller than when seen along the limb, a terminator detection allows more accurate location of the source; either limb or terminator detections allow us to calculate minimum heights.

Gas venting from Europa might also be detected from emissions excited by energetic electrons, which can be seen during eclipses, when Europa passes through Jupiter's shadow. An attempt to image emissions with ISS when Europa was in eclipse during Cassini's Jupiter gravity assist (Porco et al. 2003) was inconclusive due to secondary illumination, low resolution, and low SNR, as well as a lack of temporal coverage, being only a single snapshot in time. Such gaseous emissions are clearly detected on Io during eclipses (Geissler et al. 2004). Avoiding secondary illumination from Jupiter, Ganymede, Callisto, and Io is needed to obtain more definitive results.

The EIS NAC will usually acquire limb and terminator images at 10-km pixel scale or better, which is sufficient to image both small plumes that may extend <30 km above the surface (Fagents et al. 2000; Quick et al. 2013), and large plumes that may be hundreds of kilometers tall. In the phase before Europa flybys begin (and potentially later as well),

we may extend this search to lower-resolution images because of the value of early plume detections in planning future observations.

The team defined Measurement Requirements to optimize the plume-search dataset. First, the SNR should exceed 10:1 in the panchromatic (clear) bandpass for an I/F greater than 0.01 ($4\times$ brighter than the jets on Enceladus, but we expect to exceed 10:1 SNR even for $I/F = 0.001$). The image scale should be ≤ 10 km/pixel, although lower resolution images will also be acquired. Terminator images require phase angles from $90\text{--}120^\circ$, and limb images require phase angles of at least $130\text{--}170^\circ$, but again images outside these ranges will also be acquired. The separation between sampled Europa orbital true anomalies shall be less than every 30° across the full range of orbital true anomalies, because the plumes may vary in intensity throughout Europa's orbital cycle, as at Enceladus (Hedman et al. 2013). Based on possible plume detections by Roth et al. (2014), a true anomaly of $\sim 120^\circ$ may be best due to maximal tensile stresses at the inferred active fracture (Rhoden et al. 2015). Finally, the separation between sampled longitudes within 60° of the equator shall be less than every 10° across the full range of longitudes, to ensure a thorough global search. However, geometric constraints limit the number of phase angles and true anomalies at which each longitude bin can be imaged.

2.3.2 Surface Changes over Time

Change detection with EIS color filters will also enable a search for fresh plume deposits on Europa's surface. The extent to which Europa's plume activity will be accompanied by thermal signatures is unknown (Rathbun and Spencer 2020), and both observations and modeling suggest that if they exist, Europa's plumes may have markedly different intensity and output than those of Enceladus (Rhoden et al. 2015; Hansen et al. 2019). Furthermore, the scale heights and particle components of plumes could vary from one eruption to another (Quick and Hedman 2020). In the absence of direct imaging of active plumes, the identification of plume deposits could provide evidence of recent and/or ongoing plume activity on Europa. Indeed, deposits from plumes ≤ 30 km tall could grow to be 1–10 m thick over a relatively short timescale (\sim tens of years). Such deposits will be detectable by EIS (Quick and Hedman 2020), especially if there is a brightness, color, or photometric (Sect. 2.3.3) contrast with the surrounding surface. Deposits emplaced by much larger plumes could also accumulate enough mass to be detected by EIS, provided that they are composed of large particles (e.g., 2–3 microns in radius) and/or resist compaction (Quick and Hedman 2020).

Other types of surface changes might be seen in addition to plume deposits, especially in high-resolution images. These could include topographic changes due to tectonic activity or mass wasting, albedo or color changes from an effusive eruption or thermal alteration, or changes from new impact events. Comparisons between EIS, Juno, Galileo, and Voyager data will make it possible to identify surface changes that have occurred over a 30-year period. However, these comparisons will be limited by the low amount of high-resolution coverage obtained by the previous missions. EIS will therefore make a special effort to re-image prior high-resolution coverage, ideally with similar illumination and phase angles. Surface features imaged with very different illumination conditions may appear to have changed (Becker et al. 2023), but images that better match the original illumination would be necessary to verify that change had occurred. Comparisons of EIS imaging at very high resolution over the duration of the mission, even if separated by only a few years, could reveal small-scale changes and are also planned. The current imaging plan includes color imaging at ≤ 500 -m pixel scale of $\geq 80\%$ of the surface (requirement is $\geq 50\%$). This coverage includes repeat coverage, with at least 0.5 Earth years between observations, of $\geq 40\%$ of

the surface (requirement is $\geq 12.5\%$). It also re-images $\geq 80\%$ of the area imaged by Voyager and Galileo at ≤ 1 -km pixel scale (requirement is $\geq 50\%$).

2.3.3 Photometric Properties

Regions of unusual photometric brightness or behavior will be identified from overlapping images and targeted to search for recent deposition indicative of eruptions or impacts. Sites of recent activity could exhibit color and albedo anomalies (best observed at low phase angles) and/or textural anomalies (best seen at high phase angles). Increased reflectance at high phase angles may indicate areas of recent activity. Low-phase ($< 0.1^\circ$) observations are very limited, but will be used to look for photometric effects related to near-uniform particle sizes that might indicate fresh plume deposits (Nelson et al. 2002). Fitting photometric models is also important for normalizing image brightness for mosaics and for derivation of Bond albedo, described below.

2.4 Ice Shell and Ocean

2.4.1 Topography

Three kinds of topographic data will be generated by the Europa Clipper mission: two-dimensional (2D) topographic maps from EIS stereo images, 1D profiles from REASON altimetry (Blankenship et al. 2024, this collection) and EIS limb profiles, and points on the limb from Europa-UVS occultations (Retherford et al. 2024 this collection). The 2D maps have a different primary science justification from the profile and point data.

EIS topographic maps will assist in geological interpretation and permit geophysical modeling. Topographic data can help to clarify cross-cutting or stratigraphic relationships between geologic landforms, and identify subtle features that are not evident in imaging data, such as the broad depressions on Enceladus (Schenk and McKinnon 2009) or some normal faults on Europa (Nimmo and Schenk 2006). For geophysical analysis, topographic data can be used to test quantitative models of structures; examples include collapse and relaxation of impact craters (Dombard and McKinnon 2006; Turtle and Pierazzo 2001), intrusive diapirism (Manga and Michaut 2017), band support (Nimmo et al. 2003b), double-ridge formation (Dombard et al. 2013; Johnston and Montési 2014; Cashion et al. 2024), elastic flexure at chaos margins (Figueredo et al. 2002), and topographic rises (Nimmo et al. 2003a).

Another science objective for EIS topographic data is to assist in interpretation of REASON sounding data. Surface topography can result in off-nadir radar reflections that are hard to distinguish from sub-surface echoes; because of the large impedance contrast, this surface “clutter” can overwhelm the other signals and make interpreting the subsurface structure difficult or impossible. However, if the surface topography within the area illuminated by radar can be measured, the surface clutter can be modeled, thus permitting subsurface echoes to be identified. This technique has been used successfully at Mars by combining Mars Orbiter Laser Altimeter (MOLA) gridded altimetry with Shallow Radar (SHARAD) sounding data (Choudhary et al. 2016). Removal of clutter and accurate horizontal registration of the radar profiles are also important to allow accurate, repeat altimetric measurements to be made, in order to determine the amplitude of Europa’s tidal deformation (Steinbrügge et al. 2018).

The primary science objective for the 1D limb profiles and occultation data is to constrain the long-wavelength shape of Europa (the stereo patches are too small to do so). The natural

way to represent long-wavelength topography is by using spherical harmonics; the maximum spherical harmonic degree that can be recovered from a series of 1D profiles depends on the maximum gap distance between profiles (Nimmo et al. 2011). Long-wavelength topography can be used to investigate different aspects of Europa. First, it can be used to test predictions of long-wavelength topographic variations arising from spatial variations in tidal heating (Nimmo et al. 2007) and constrain ice-shell properties (Sect. 2.4.3). Second, individual topographic profiles can be compared with the corresponding inferred shell thickness (from radar sounding) to determine whether the shell follows an Airy isostatic balance, as is expected for Europa. If it does not, flexural effects or lateral density variations must be occurring. Third, the long-wavelength topography can be compared with the long-wavelength gravity to probe the ice shell structure. This technique is only likely to be successful at high spherical harmonic degrees, where the gravity contribution of the mantle is attenuated (e.g., Koh et al. 2022).

2.4.2 Geodesy

An important EIS objective is to establish a geodetic framework for Europa into which observations can be placed for spatial analysis and to facilitate co-analysis with other investigations. To do so, the rotation state (orientation as a function of time) of Europa needs to be established. Some aspects of this rotation state also contain physical information about the state of the interior.

The rotation rate of Europa is not constant, but varies periodically over the orbital timescale (diurnal librations) and also at longer periods, notably the 460–480-day Laplace resonance and a 30-year period (Rambaux et al. 2011). The expected amplitude of the diurnal librations is ~ 150 m; because of the tradeoffs involved, this amplitude is not likely to be diagnostic of Europa's shell structure (Van Hoolst et al. 2013), unlike the case at Enceladus (Thomas et al. 2016). The longer-period librations are expected to be larger (amplitude ~ 1 km). Both librations could make image mosaicking challenging unless properly accounted for. Europa's shell may also experience non-synchronous rotation, although at present only upper bounds on the rotation rate exist (Hoppa et al. 1999).

Europa is expected to exhibit a small obliquity, $\sim 0.05^\circ$ (Chen et al. 2014), or about 1-km pole offset at the surface; ignoring this offset would lead to variations in apparent latitude of surface features of as much as 2 km. An obliquity larger than this value would strongly suggest a decoupled shell, as at Titan (Bills and Nimmo 2011). The spin pole will also precess to track Europa's orbit pole precession (~ 30 -year timescale). The current best estimate of the spin pole direction is 270° (90° is defined as a spin pole inclined in the direction of Jupiter at pericenter), and $\sim 120^\circ$ of precession is recorded in the cycloidal fracture patterns (Rhoden et al. 2021), which is consistent with the spin pole precessing rapidly with respect to Europa's surface age.

Globally distributed EIS images will be the primary dataset for constructing a geodetic control network for Europa. The foundation of the geodetic control network will be a globe-circling geodesy image dataset, optimized as described below for measuring the diurnal libration. Images from global mosaics will be included in the adjustment, so that controlled mosaics with optimal (and known) spatial accuracy can be constructed. The images will be used in a photogrammetric bundle adjustment, along with additional constraints from the global shape observations described above. The outputs of the bundle adjustment will be mutually consistent estimates for a network of ground coordinates of features located in overlapping images, updated camera pointing, and improved or newly estimated rotational parameters.

2.4.3 Constraining Ice Shell Thickness

Tidal heating within Europa's ice shell is expected to vary spatially (Ojakangas and Stevenson 1989). As a result, shell thickness variations may arise, which in turn could give rise to topographic relief of order 1 km (Nimmo et al. 2007). These variations will be at long wavelengths (spherical harmonic degree $l=2$ and $l=4$) and can thus be probed by altimetric profiles. If the predicted long-wavelength variations are observed, they will provide a constraint on the shell thickness and viscosity structure. If they are not observed, then either the shell is conductive but thin, or the shell is sufficiently thick that lateral flow of ice is rapid enough to erase thickness variations. The latter would be the case if the shell were convecting.

The structure of large impact craters also provides constraints on ice shell thickness over time (Turtle and Pierazzo 2001; Schenk 2002; Bray et al. 2014). Local ice shell thickness can also be modeled from elastically supported topography (Nimmo et al. 2003a).

2.5 Surface Composition

Key to understanding Europa's chemistry and astrobiological potential is identifying chemical and mineralogic species exposed on Europa's surface in regions of disruption or recent activity (e.g., Greenberg et al. 1999; Head and Pappalardo 1999; Nimmo and Gaidos 2002; Schmidt et al. 2011) and determining whether these materials originate from ocean brines or brine lenses in the ice shell. The EIS investigation contributes to these efforts in three ways: 1) mapping global-scale surface variations, 2) constraining the composition of materials exposed on Europa's surface, and 3) extrapolating compositional information gleaned by other instruments to finer scales and wider areas than are accessible in those data.

2.5.1 Mapping Global-Scale Surface Variations

The asymmetry between Europa's leading and trailing hemispheres (Nelson et al. 1986; McEwen 1986) likely results from heterogeneous radiation effects and material from Io (Paranicas et al. 2002), both of which are concentrated on the trailing hemisphere, as well as cometary impacts, which are greatest on the leading hemisphere (Zahnle et al. 1998). These processes act on a surface that, itself, is being modified by endogenic processes including some that likely deposit and/or expose fresh materials on the surface. Comparing EIS global-scale color observations that reveal global patterns correlated with exogenic processes to EIS small-scale and local-scale observations that resolve geologic features correlated with endogenic material will provide critical information needed to distinguish between these processes. Such comparisons will be completed using a variety of EIS observations including color mosaics, color ratios, and derived photometric properties.

Expected color coverage by EIS includes (1) near-global coverage at ~ 250 – 400 m/pixel acquired by the NAC during joint scans acquired while approaching and receding from Europa; (2) $\geq 20\%$ coverage acquired by the WAC along-track imaging, ranging from 5.5 to >400 m/pixel; and (3) color coverage acquired with the NAC as part of small-scale imaging. The amount of NAC color coverage at small-scale (and potentially regional- or global-scale) will depend on data volume allocations and science tradeoffs with other objectives such as additional panchromatic and stereo coverage.

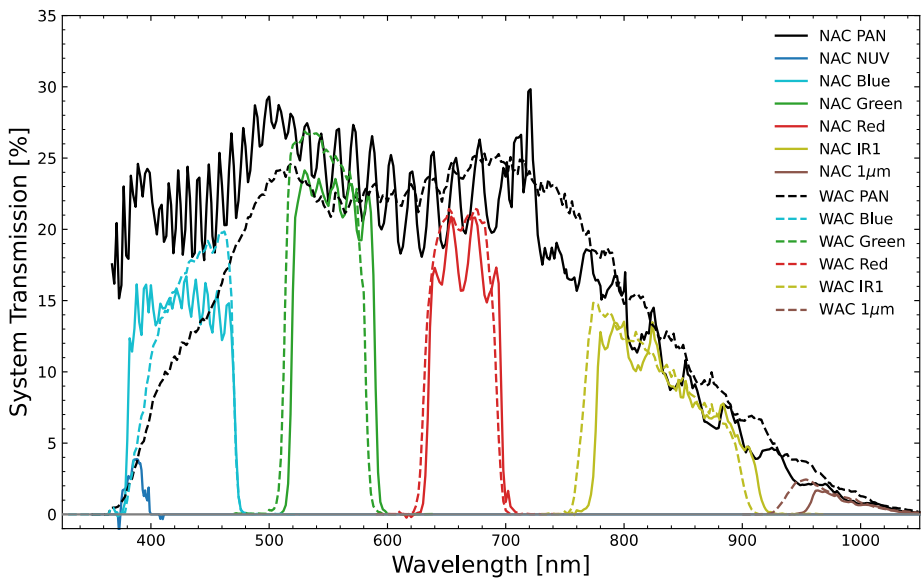


Fig. 2 EIS panchromatic and color-filter system transmission for NAC (solid lines) and WAC (dashed lines). NAC NUV is derived from component-level measurement. WAC NUV is not shown here due to very low transmission at these wavelengths through the WAC optics. The periodic nature of the NAC transmission is related to the anti-reflection coatings

2.5.2 Constraining the Compositions of Materials Exposed on Europa's Surface

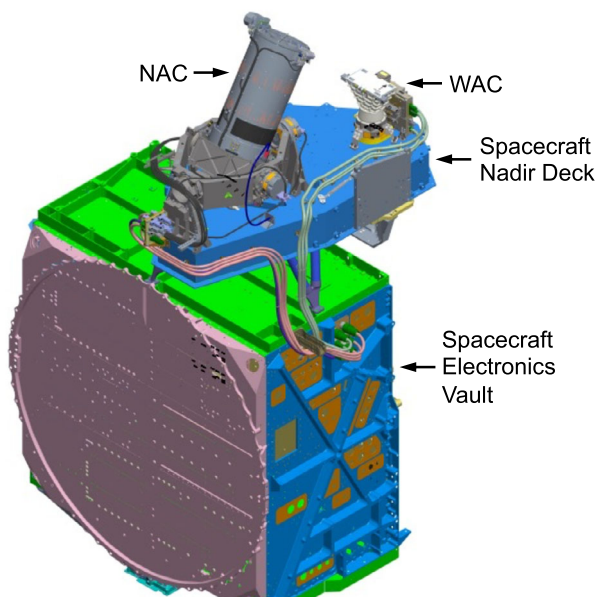
The NAC spectral response covers 358–1050 nm, that of the WAC covers 370–1050 nm, and their color filters (Fig. 2) provide broadband spectral coverage of this wavelength range. The WAC has a similar iFOV to many of the other Europa Clipper remote-sensing instruments (Daubar et al. 2024, this collection, Figs. 6 and 7), which will aid in comparing these data and facilitate combining WAC data with Europa UVS, MISE, and E-THEMIS data to analyze spectra covering UV to IR wavelengths. The EIS spectral range is particularly well suited to observe color centers that form in irradiated salts allowing, for example, differentiation between irradiated MgSO_4 and NaCl (Hibbitts et al. 2019).

The EIS color data, especially from the joint scans, will result in observations over a wide range of phase angles, important for improved photometric models (e.g., to normalize mosaics or perform photoclinometry) and Bond albedo maps. Photometric anomalies may be indicative of recent activity.

2.5.3 Extrapolating Compositional Information

Multiple Europa Clipper instruments will contribute to determining the composition of Europa's surface, including MISE, SUDA, MASPEX, Europa UVS, REASON, and EIS. By correlating this information with EIS color observations at comparable regional scales, we will be able to extrapolate color–composition correlations to finer-scale geological features identified in high-resolution images and topography to provide important constraints on potential endogenic origins of surface materials. These correlations can also be used to provide insight into the composition at potential landing sites (Sect. 2.2.5).

Fig. 3 Configuration of the NAC and WAC, spacecraft nadir deck, harnesses (NAC harness in pink and WAC in green), and electronics vault with additional radiation shielding. The NAC is shown with the gimbal in the launch orientation (Sect. 3.4.1)



2.6 Europa's Connection to the Jupiter System

Europa is part of an interrelated system. Jupiter's magnetosphere, carrying material from Io, modifies Europa's surface and ionosphere. The orbits of Io, Europa, and Ganymede are connected via the Laplace resonance, resulting in tidal heating of Europa that helps to maintain its interior ocean. Europa Clipper remote sensing observations are concentrated on Europa, but observations acquired for calibrations or rehearsals during flybys of other satellites and monitoring activity on Io, which has effects at Europa, will also have direct science value, providing system context. In particular, an early dayside flyby of Ganymede may prove extremely helpful to improving science planning and data processing procedures needed for the Europa flybys.

3 Instrument Description

3.1 Overview

The EIS cameras achieve Europa science objectives (Sect. 2) with capability to image across a wide range of scenarios spanning high-altitude faint scenes to low-altitude, fast flybys with rapidly changing geometry and illumination. The EIS system consists of a narrow-angle camera (NAC) and a wide-angle camera (WAC) mounted on the spacecraft nadir deck (Fig. 3). The detector configurability can accommodate spacecraft ground-track speeds of up to ~ 4.5 km/s at closest approach as low as 25-km altitude (at faster speeds imaging is possible with lower SNR), scene brightness (a function of albedo and illumination) ranging from 99% to 1% I/F, and illumination geometry for several datasets varying in range from > 1 million km to < 50 km (Fig. 1).

The NAC (Sect. 3.4) field of view (FOV) is $2.3^\circ \times 1.2^\circ$ and instantaneous FOV (IFOV) is $10 \mu\text{rad}$, achieving very high-resolution 0.5-m pixel-scale over 2-km-wide swaths from

50-km range. The NAC optical telescope assembly (OTA) is mounted on a two-axis gimbal supporting independent targeting for mapping mosaics and stereo observations without impacting spacecraft operations. The gimbal enables near-global ($\sim 90\%$ with the observation plan for the baseline trajectory, 21F31_V6) mapping of Europa at ≤ 100 -m pixel scale and high-resolution stereo imaging producing digital terrain models (DTMs) with ≤ 4 -m ground sample distance (GSD) and ≤ 0.5 -m vertical precision.

The WAC (Sect. 3.5) has a $48^\circ \times 24^\circ$ FOV, and IFOV of 218 μrad , achieving 11-m pixel scale over a 44-km-wide swath from 50-km range. The 24° along-track FOV enables three-line (forward, nadir, and aft) stereo swaths, producing DTMs with ≤ 32 -m GSD and ≤ 4 -m vertical precision.

Each camera has identical digital electronic chains from the detector through the SpaceWire transfer to the spacecraft, with identical focal plane modules (FPMs, Sect. 3.3.1) and detector electronics (DE, Sect. 3.3.3). The only difference between the two data processing units (DPUs, Sect. 3.3.4) is the power and circuitry to drive the NAC gimbal.

Design, integration, and testing of the instruments was performed at APL. The NAC OTA (Sect. 3.4), procured from L3 Harris-Integrated Optical Systems (formerly known as L3-SSG), is based on flight heritage from the New Horizons Long Range Reconnaissance Imager (LORRI) telescope (Cheng et al. 2008). The CMOS detectors (Sect. 3.3.1), procured from SRI International, are based on a version of their active pixel sensor, space qualified for Solar Orbiter SoloHI and the Wide-field Imager for Solar PRobe (WISPR). APL built the detector interface board (DIB), DE (Sect. 3.3.3) and DPU (Sect. 3.3.4), which carry design heritage from the LORRI, Compact Reconnaissance Imaging Spectrometer for Mars (CRISM), and Juno Energetic-particle Detector Instrument (JEDI) instruments.

3.2 Instrument Performance Requirements, Design Drivers, and Capabilities

The EIS NAC and WAC complement each other to achieve Europa science objectives (Sect. 2). Performance requirements driving each camera's design include image resolution, signal-to-noise ratio, and stereo and color imaging capability. Simultaneous acquisition of multiple images (color and WAC stereo) during high-speed flybys drives the overall EIS data rate requirements (from the FPM to the DPU and from the DPU to the spacecraft bulk data storage (BDS)).

3.2.1 Signal-to-Noise Ratio

High-phase-angle, low-illumination plume-search observations to detect plumes as faint as $I/F = 0.01$ at phase $\geq 160^\circ$ drive the NAC and WAC stray light and low light SNR requirements. Photometry, panchromatic and stereo topography observations, and closest-approach imaging drive the panchromatic SNR requirement. Regional-scale and small-scale observations and recent-activity color data drive the color SNR requirements for all filters. Science objectives include distinguishing subtle color differences in similarly colored surface units. Similarity to other imaging systems used at Europa drives the wavelength range requirement and spectral characteristics of each color band. Adequate contrast distinguishing typical 2-pixel features drives the requirement of ≥ 0.05 modulation transfer function (MTF) for the system at Nyquist for both cameras.

3.2.2 Distortion

The NAC average radial distortion is characterized to < 0.16 pixel prelaunch (0.9-pixel maximum distortion). The WAC distortion has been characterized to 0.3 pixels; WAC geometric

distortion is required to be $<10\%$ across the full FOV and achieves 3.1% maximum distortion in the corners. The expectation is for in-flight radial distortion characterization to be <0.1 pixel, which is needed for stereo imaging and geodesy objectives.

3.2.3 Europa Clipper Environmental Requirements and EIS Mitigations

The Europa Clipper spacecraft environment during cruise and Jupiter orbit presents specific challenges to the EIS design. Potential direct solar exposure and the thermal environment drove the need for a flight cover assembly and blanket design modifications. Shielding for the Jovian radiation environment increased the mass of EIS significantly. Interactions between payload elements drove specific and challenging outgassing and electromagnetic radiation (Sect. 3.2.5) requirements.

3.2.4 Thermal Design

The initial cruise trajectory included a Venus flyby, which increased the required maximum survival temperature. The trajectory was later changed to a Mars gravity assist, which reduced the survival temperature range and improved the margin for the NAC thermal design. The Flight Cover Assembly (FCA) pin pullers required blanketing to prevent unintended release at high temperature. The thermal blanket material required lower absorptivity/emissivity ratios to reduce surface temperatures. The WAC and NAC covers remain in place until ≥ 2 and 3 AU, respectively, to protect against direct solar intrusion into the telescopes.

3.2.5 Electromagnetic Interference and Compatibility (EMI/EMC)

To prevent interference during concurrent observations by the REASON instrument, the EIS design had to meet challenging radiative and conductive emission requirements. External vault emission limits at the REASON HF and VHF 9 and 60 MHz bands were particularly challenging. The oscillator frequency selected for EIS satisfied the SERDES (Serializer/Deserializer) and detector clock needs, but the REASON VHF 60 MHz bandwidth increased after procurement of the EIS oscillators and overlapped the third harmonic for the 19.5 MHz detector clock. To reduce the amplitude of the 60-MHz violation, both NAC and WAC integrated a mechanical clamp at the DIB flex cables, which fixed the location and separation of the cables. In order to reduce NAC motor noise in both the 9 and 60 MHz bands, an additional board populated only with inductors was required for the NAC DPU. The additional electronics box is housed within the spacecraft electronics vault and interfaces between the DPU and the NAC gimbal. Finally, the power gimbal board layout was modified for the flight model (FM) to reduce the emissions in these bands.

3.2.6 Radiation Design and Mitigation

The Jovian radiation environment drove many design decisions for the EIS instrument. Areas of concern included internal charging, electrostatic discharge, and total ionizing dose (TID). Electrical, electronic, and electromechanical (EEE) parts were rated to 300 krad, driving packaging material and mass for boxes outside the vault. The spacecraft electronics vault provides much of the shielding for boxes mounted inside. Thick, fused silica protective optics for both NAC and WAC and ~ 5 kg of titanium surrounding the WAC telescope optics reduce darkening of the lens materials and lower the TID to 40 krad for the NAC FPM, and 20 krad for the WAC FPM, for a radiation design factor (RDF) of two. To avoid any build-up of charge, the harnessing required multiple layers of metal shielding grounded to the backshells, allowing for static bleed off of charge, and all heaters required taping and grounding.

Table 5 EIS camera characteristics and parameters

Key Parameters	Narrow-Angle Camera (NAC)	Wide-Angle Camera (WAC)																																				
Telescope	Reflective, Ritchey Chrétien: 2 mirrors, 3 lenses	Refractive: 8 lenses																																				
Effective Focal Length	1000 mm	46 mm																																				
F number	6.58	5.75																																				
Detector		2048 × 4096 CMOS, 10- μ m pixels																																				
SNR		Plume Search: 10:1 for I/F \geq 0.01 Panchromatic: 50:1 for I/F \geq 0.2 RED, GRN, BLU: 100:1 for I/F \geq 0.2 NUV, IR1, IMC: 20:1 for \geq 0.2																																				
In-field Stray Light	3.0–8.0% at end of life (EOL) depending on specific plume illumination and collection geometry	6.0–10.0% at EOL depending on specific plume illumination and collection geometry																																				
Out-of-field Stray Light	<table border="1"> <thead> <tr> <th>Angle</th> <th>Point Source Transmittance (PST)</th> <th>Angle</th> <th>PST</th> <th>Scatter</th> <th>Ghosts</th> </tr> </thead> <tbody> <tr> <td>> 30°</td> <td>< 2 × 10⁻⁴</td> <td>> 80°</td> <td>< 4 × 10⁻⁷</td> <td>< 4 × 10⁻⁷</td> <td>0</td> </tr> <tr> <td>> 50°</td> <td>< 5 × 10⁻⁵</td> <td>> 20°</td> <td>< 3 × 10⁻⁵</td> <td>< 3 × 10⁻⁵</td> <td>0</td> </tr> <tr> <td></td> <td></td> <td>> 5°</td> <td>< 1.2 × 10⁻³</td> <td>< 1.2 × 10⁻³</td> <td>0</td> </tr> <tr> <td></td> <td></td> <td>> 2°</td> <td>< 1.5 × 10⁻²</td> <td>< 1.3 × 10⁻²</td> <td>< 0.2 × 10⁻²</td> </tr> <tr> <td></td> <td></td> <td>> 1°</td> <td>< 2.5 × 10⁻²</td> <td>< 1.8 × 10⁻²</td> <td>< 0.7 × 10⁻²</td> </tr> </tbody> </table>	Angle	Point Source Transmittance (PST)	Angle	PST	Scatter	Ghosts	> 30°	< 2 × 10 ⁻⁴	> 80°	< 4 × 10 ⁻⁷	< 4 × 10 ⁻⁷	0	> 50°	< 5 × 10 ⁻⁵	> 20°	< 3 × 10 ⁻⁵	< 3 × 10 ⁻⁵	0			> 5°	< 1.2 × 10 ⁻³	< 1.2 × 10 ⁻³	0			> 2°	< 1.5 × 10 ⁻²	< 1.3 × 10 ⁻²	< 0.2 × 10 ⁻²			> 1°	< 2.5 × 10 ⁻²	< 1.8 × 10 ⁻²	< 0.7 × 10 ⁻²	
Angle	Point Source Transmittance (PST)	Angle	PST	Scatter	Ghosts																																	
> 30°	< 2 × 10 ⁻⁴	> 80°	< 4 × 10 ⁻⁷	< 4 × 10 ⁻⁷	0																																	
> 50°	< 5 × 10 ⁻⁵	> 20°	< 3 × 10 ⁻⁵	< 3 × 10 ⁻⁵	0																																	
		> 5°	< 1.2 × 10 ⁻³	< 1.2 × 10 ⁻³	0																																	
		> 2°	< 1.5 × 10 ⁻²	< 1.3 × 10 ⁻²	< 0.2 × 10 ⁻²																																	
		> 1°	< 2.5 × 10 ⁻²	< 1.8 × 10 ⁻²	< 0.7 × 10 ⁻²																																	
Spectral Range		\leq 400–1050 nm																																				
Color Bands		1 panchromatic area and 6 color bands (see Table 7)																																				
Pixels per Image		Framing imaging area: 4032 × 1536 cross-track × along-track (XT × AT) Pushbroom: 4032 XT × variable length AT																																				
Field of View (FOV)	2.3° × 1.2° (XT × AT)	48° × 24° (XT × AT)																																				
Instantaneous (IFOV)	10 μ rad	218 μ rad																																				

Table 5 (Continued)

Key Parameters	Narrow-Angle Camera (NAC)	Wide-Angle Camera (WAC)
Pointing	nadir $\pm 30^\circ$ AT & XT	nadir
Image and stereo DTM properties @ 50-km altitude	0.5-m pixel-scale 2-km-wide cross-track swath 4-m ground sample distance (GSD) 0.5-m vertical precision	11-m pixel-scale 44-km-wide cross-track swath 32-m GSD 4-m vertical precision
Data rate	FPM to DPU: Maximum rate of 19.53 MHz, 312 Mpixels/second with maximum effective data rate, but ~ 284 Mpixels/s accounting for overhead in transmission DPU to spacecraft BDS: 150 Mb/second	
Mass (not including harness)	44.1 kg (sensor assembly, DPU, inductor box)	15.4 kg (sensor assembly, DPU)
Power (for a subset of cases)	40.5 W (imaging, average) 127.9 W (1 axis gimbal slew, peak) 13.4 W (standby idle, average)	33.3 W (imaging, average) 16.1 W (standby idle, average)

3.3 Common Elements

Both NAC and WAC have identical imaging electrical chains from the detector through the DPU digital board. The following sections describe these subassemblies.

3.3.1 Focal Plane Module (FPM)

The FPM consists of the imaging sensor, the substrate with six broadband color filters, the DIB, cold-head, trim heater, and packaging. Each camera has a trim heater, powered and controlled by the respective DPU, to stabilize the operational temperature of $-60\text{ }^{\circ}\text{C} \pm 1\text{ }^{\circ}\text{C}$. The FPM has a mechanical interface with the telescope and an electrical interface to the Detector Electronics (DE).

Frontside-illuminated (FSI) complementary metal-oxide semiconductor (CMOS) detectors (Table 6) are the imaging sensors for EIS NAC and WAC. The chip design is based on the SRI International $M_k \times N_k$ CMOS active pixel sensor modular architecture (Janesick et al. 2014). An earlier version of the detector was used in the Solar Orbiter SoloHI (Howard et al. 2013; Korendyke et al. 2013) and Parker Solar Probe (PSP) WISPR (Vourlidis et al. 2016) instruments. This 8-Megapixel detector design features low read noise, high MTF, wide spectral range, and a large dynamic range (Janesick et al. 2006, 2009, 2010, 2013, 2014). Advantages of CMOS detector technology include very fast readout times, low readout noise, and low power. TID tolerance (no measurable degradation after 100 krad from 2-MeV electrons (McEwen et al. 2012; Janesick et al. 2013)) far exceeds the detector's <50 -krad environment (Sect. 3.2.6) behind shielding.

On-chip correlated double sampling eliminates row-settling time, and 16 fast readout ports (up to 20 Mpixels/s/port) enable pushbroom imaging when the ground line time is shortest near closest approach at ~ 4.5 km/s ground speed. DPU processing provides TDI capabilities to increase SNR.

3.3.2 Color Filters

The NAC and WAC both have six broadband color filters (Table 7, Figs. 2 and 4). Six color stripes are deposited on a single fused silica substrate using photolithography techniques and dichroic thin film coatings (Ryan et al. 2018). The substrate is mounted directly into the FPM packaging 0.3 mm in front of the CMOS chip. Each filter is 320 microns (32 pixels) wide allowing up to ~ 30 rows of TDI imaging. Opaque stripes and boundaries allow for pixel noise characterization throughout the life of the mission.

3.3.3 Detector Electronics (DE)

The DE interface to the detector via three DIB rigid flex cables. Each cable has three layers of metallic overwrap to mitigate internal electrostatic discharge (iESD) effects. The DIB flex cables are mechanically clamped to reduce the 19.5-MHz detector clock emissions. An RTAX2000SL field-programmable gate array (FPGA) programs the digital-to-analog converters (DACs) that provide low-voltage detector biases, executes row selection and order to configure the CMOS imaging sensor, and the 16 ADCs digitize the FPM output voltage, sending the digital counts to the DPU. The 16 detector channels are digitized with 12-bit ADCs at a speed close to 20 MHz. The DE is based on CRISM architecture (Murchie et al. 2007). The FPM trim heater telemetry circuit located on the DE board provides temperature telemetry to the DPU.

Table 6 EIS detector characteristics

Key Parameters	Characteristics/Performance
Detector type	CMOS, frontside illuminated (FSI)
Detector area	4096 (cross-track) × 2048 (along-track) pixels (32 rows and columns are masked along each edge)
Pixel type	5 Transistor Pinned Photodiode (5T PPD) (Janesick et al. 2006)
Pixel size	10 μm
Pixel full well*	Requirement: ≥10,000 e ⁻ (high gain); ≥50,000 e ⁻ (low gain) NAC (flight model “FM04” detector): 21,500 e ⁻ (high gain); 156,000 e ⁻ (low gain) WAC (flight model “FM03” detector): 22,000 e ⁻ (high gain); 160,000 e ⁻ (low gain) (both at the 3% non-linearity threshold)
Quantum efficiency*	NAC (“FM04”): 38% @ 505 nm, 34% @ 545 nm WAC (“FM03”): 32% @ 505 nm, 29% @ 545 nm
Read noise* (50% of pixels)	Requirement: ≤25 e ⁻ (high gain); ≤85 e ⁻ (low gain) NAC (“FM04”): 12 e ⁻ (high gain) or 95 e ⁻ (low gain) WAC (“FM03”): 11 e ⁻ (high gain) or 83 e ⁻ (low gain)
Quantization	12 bits
Gain	6.7 e ⁻ /DN (high gain); 53.0 e ⁻ /DN (low gain)
Exposure range	0.01 ms to 10 s manual (without TDI) (spacecraft stability may limit the maximum practical exposure time to 0.5–1 s)
Data compression	real-time wavelet compression (Hayes et al. 2009)
Imaging types	pushbroom with TDI, framing (rolling shutter)
Modes	imaging, warmup, decontamination, standby, off
Detector operating, survival T	Nominal operating temperature: −60° ± 1 °C; survival: −90° to +80 °C
Dark-current at EOL	<30 e ⁻ /pixel/s at −60 °C (post-radiation exposure)
Readout rate	≤20 Mpixels/s/port × 16 ports Full panchromatic frame readout: 20 ms (Entire 4k × 2k detector readout, including filters and masked rows: 26 ms)

*Averaged over all 16 ports

3.3.4 Data Processing Unit (DPU)

The WAC and NAC DPUs supply power to and receive image data from their respective DEs, receive commands from and send telemetry to the spacecraft, and perform image processing prior to transmission to the spacecraft BDS. The NAC DPU provides power and controls the gimbal rotary actuators. Both DPUs are located inside the electronics vault. Approximately 6 m of harnessing connects each DPU to its sensor assembly mounted on the nadir deck.

The DPU assemblies consist of the Digital Board (DB), the Power Gimbal Board (PGB), and packaging. The DPU supplies secondary power to the DE, FPM, the FPM trim heater, and gimbal. The EIS Flight Software (FSW) and DB FPGA manage the CMOS imaging parameters, the digital data received from the DE, and NAC gimbal commanding. The

Table 7 EIS broadband filter wavelength ranges based on the system full width half maximum (FWHM) points measured during NAC and WAC final ground calibration (see Fig. 2)

Filter	Key Uses	Wavelength (nm)	
		NAC	WAC
PAN	Surface observations, stereo, context imaging, best SNR for faint targets, e.g., plume searches	367–801*	434–838*
NUV	Surface color; plumes w/ Rayleigh scattering	~375–395 low transmission (Fig. 2)	(very low transmission**)
BLU	Surface color; Rayleigh scattering w/ NUV	381–470	398–470**
GRN	Surface color; airglow (eclipse, nightside)	519–589	513–581
RED	Surface color	635–696	632–691
IR1	Surface color; continuum for H ₂ O band	776–887	766–875
1MC (1- μ m)	Surface color; coarse-grained ice H ₂ O band	958–994*	937–986*

*Panchromatic and 1-micron filters extend to 1050 nm with sensitivity below half maximum (Fig. 2)

**WAC transmission at wavelengths shorter than ~400 nm is limited by transmission through the refractive optics

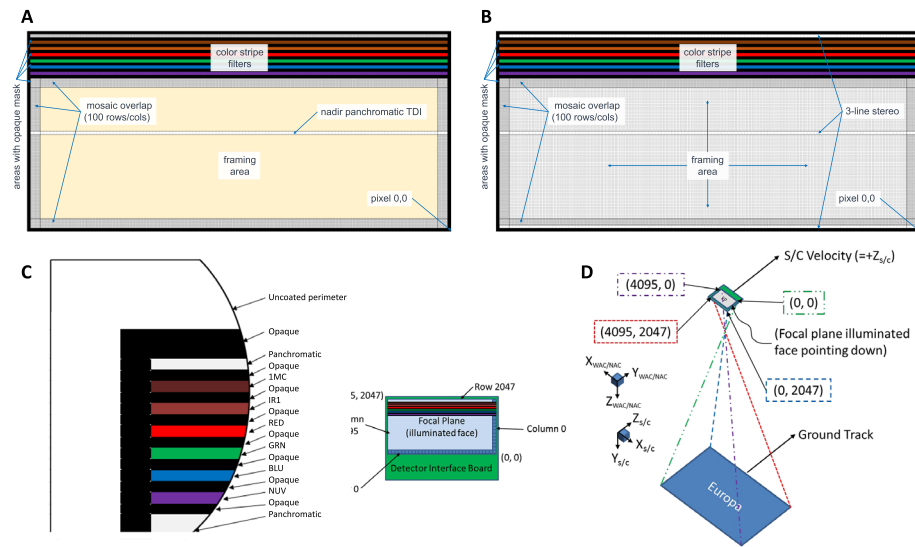


Fig. 4 EIS NAC and WAC filter layouts and imaging applications for (A) NAC and (B) WAC, with (C) zoom view of color filters and opaque masking. The filter stripes and the opaque masks between them are each 32-rows wide. (D) shows the detector orientation on the spacecraft. (Transmission through the color filters is shown in Fig. 2)

CMOS imaging parameters, such as row selection and integration time are uplinked from the ground, stored in memory and written to the DE FPGA registers for execution. After data collection, the flight software and DB FPGA manage the data by labeling, compressing, packaging and sending the packets to the spacecraft BDS system over SpaceWire. The DPU collects instrument telemetry and delivers it to the spacecraft in the health and safety (H&S) packets.

Digital Board (DB) The DB is identical between the NAC and WAC. It receives commands from and sends telemetry to the spacecraft over SpaceWire, to the DE over Universal Asynchronous Receiver/Transmitter (UART), and to the PGB over General Purpose In and Out (GPIO). The DE sends image data over the SERDES to the DB, where it is processed and compressed. The FPGA, a Xilinx Virtex-5QV, controls much of each camera's functions and the pixel-processing pipeline. The SpaceWire telemetry link operates at 200 Mbps and the commanding link at 80 Mbps.

Power Gimbal Board (PGB) The PGB design slightly differs between the NAC and the WAC. The WAC DPU uses a 5-A service, and the NAC DPU uses 5- and 10-A services. The 10-A service supplies power to the gimbal actuators. The PGB generates secondary power for the DB and switched secondary power for the DE and the NAC gimbal actuators. Trim heaters for both cameras are controlled by the PGB. The NAC DPU commands the gimbal and receives gimbal position feedback from the position contact sensors.

Flight Software Instrument flight software is based on JHU APL Integrated Universal Sub-orbital (JANUS) Platform, Multi-mission Bus Demonstration (MBD), Solar TERrestrial RELations Observatory (STEREO), and MERcury Surface, Space ENvironment, GEOchemistry and Ranging (MESSENGER). TDI, compression, and hardware-dedicated software are specific to EIS. The boot software is considered mission critical because it is common between NAC and WAC. The common software handles packet telemetry and commands, provides memory management functions, executes stored command sequences, performs fault management monitoring and response, and generates housekeeping/telemetry packets. EIS flight software supports macro-based commanding for simplified ground operations. Macros are stored command sequences which can nest with 32 macros operating concurrently.

3.4 NAC Sensor Assembly

The NAC has five major subassemblies (Fig. 5): the two-axis gimbal assembly (Sect. 3.4.1), the optical telescope assembly (OTA; Sect. 3.4.2), the FPM (Sect. 3.3.1), the DE (Sect. 3.3.3), and the DPU (Sect. 3.3.4). Four of these assemblies are located on the spacecraft nadir deck, and the DPU is located in the spacecraft electronics vault. The gimbal assembly (Sect. 3.4.1) includes: the along-track (AT) and cross-track (XT) rotary actuators, bearings, gimbal rings, position contact sensor assembly, launch lock mechanism, and flexible harness. The gimbal has mechanical interfaces to the OTA, the DE, and the spacecraft nadir deck, and an electrical interface to the DPU. The gimbal moves the integrated OTA, FPM, and DE assemblies to create a $\sim 60^\circ \times \sim 60^\circ$ optical field of regard (FOR). The NAC OTA (Sect. 3.4.2) consists of the optical telescope, baffle, one-time deployable flight cover assembly (FCA), and FPM heat straps. The OTA mechanically integrates into the gimbal ring. Before the FCA is opened, it protects the OTA from contamination and from direct solar illumination during flight. The NAC DE assembly is mounted mechanically to the XT gimbal ring and has electrical interfaces with the FPM and DPU.

3.4.1 NAC Gimbal Design and Nadir Deck Interface

The NAC is articulated by a two-axis gimbal system (Fig. 5) consisting of two rotary actuators providing $\pm 30^\circ$ cross-track (outer ring) and along-track (inner ring) motion in $\sim 0.05^\circ$ increments. Each actuator contains a single winding stepper motor and a harmonic drive. The actuators are driven by the NAC DPU PGB motor control circuitry, DB FPGA, and

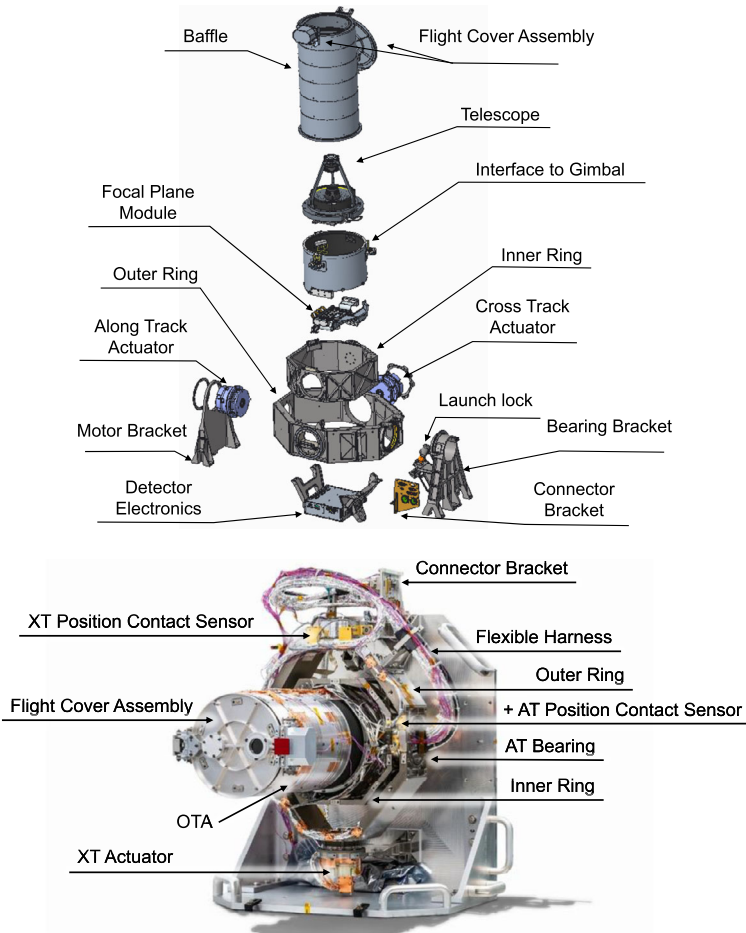


Fig. 5 NAC expanded diagram (top) and assembled flight hardware (bottom)

flight software. The NAC only images after gimbal motion has stopped and settled; jitter due to motion of the spacecraft or the gimbal would affect image quality. Targeting the NAC to acquire very high-resolution stereo imaging during high-speed (4.5 m/s) flybys at altitudes as low as 50 km drives the NAC gimbal slew rate. In order to meet operational requirements supporting global, regional, small-scale, and local-scale mapping, gimbal settling must occur within four seconds. The contributions of gimbal settling to telescope stability are required to be $\leq 1.2 \mu\text{rad}$ while an image is collected.

The AT and XT motors are commanded one at a time due to power constraints. The EIS flight software stores gimbal rate profile tables in magnetoresistive random-access memory (MRAM). Gimbal commanding uses lookup tables for full speed and a slower rate for homing the gimbal. If necessary, modification of lookup tables throughout the NAC lifetime can occur with a memory upload. Gimbal acceleration is set at either $80^\circ/\text{s}^2$ or $15^\circ/\text{s}^2$ to limit power draw, provide short settling times, or limit coupling forces to the spacecraft. The gimbal velocity starts at 50 steps/s, accelerates to 300 steps/s, and then decelerates back to 50

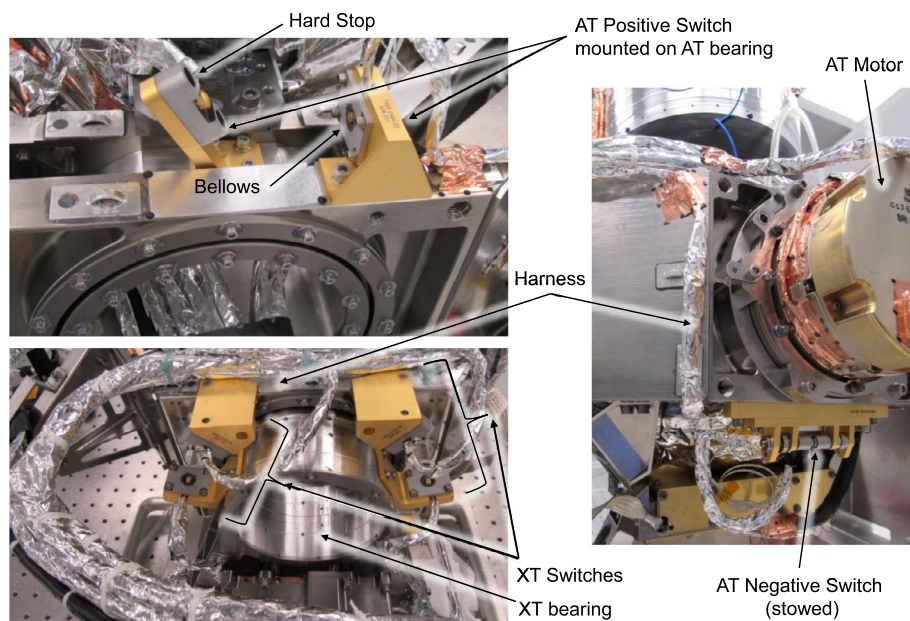


Fig. 6 Gimbal bearings, PCS, and hard stops

steps/s. If motion along both axes is required, flight software defaults to commanding the AT gimbal first and then the XT gimbal.

The gimbal determines its position by counting steps and a system of electrical Position Contact Sensors (PCS). Each PCS has precisely mounted metallic bellows (Fig. 6) that produce an electrical signal when touched by a nut on the moving member. The bellows produce a signal within two steps (0.1°) and can be compressed to a maximum of 22 steps (1.1°). The flight software counts the steps after the signal is sensed to determine the position of the gimbal on that axis. There is a hard stop around the bellows to keep the bellows from being crushed by an over travel. Both XT PCS and one AT PCS interface to the bearings and the AT motor. The second AT PCS is mounted on a flip mechanism, which moves the sensor into place after the gimbal launch lock is released to prevent motion beyond 30° .

At launch, the gimbal is stored with a launch lock at 32° (Fig. 3), which is outside the operational FOR. The launch lock is a mechanism with a shape memory alloy enclosure that stretches under thermal load to fracture an internal 0.25" bolt. The launch lock uses spacecraft powered heaters and platinum resistance thermistors (PRTs) and does not provide electronic telemetry when released. A load spreader, pre-crushed honeycomb, and nutil epoxy attenuate the shock of the breaking bolt. The launch lock release occurs soon after launch.

The flexible harness winds from the DE through both axes of the gimbal to the nadir deck connector bracket. The harness bundle consists of data, clock, power, and high-speed SERDES image data cables. Each cable is shielded from radiation as well as electrical static build up with several layers of metallic shielding. The bundle is routed to minimize effects on gimbal movement. A 0.3-m loop of harness exits the gimbal along the XT bearing bracket and feeds into the nadir-deck connector bracket. It is unsupported, but the shielding provides enough stiffness to survive launch.

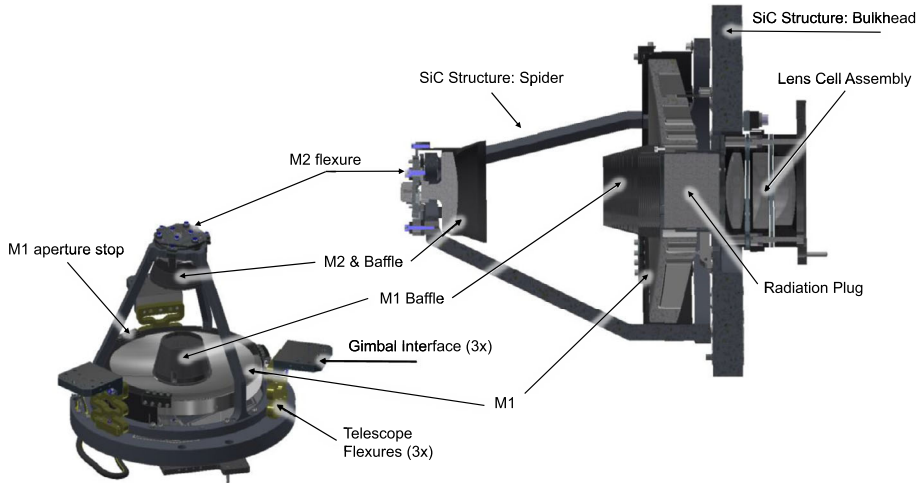


Fig. 7 Schematic illustration of the NAC telescope

3.4.2 NAC Optical Design

The NAC OTA is a Ritchey-Chrétien telescope with a three-lens cell assembly (Fig. 7), stray-light baffles, and a one-time deployable cover. The telescope design is derived from the New Horizons LORRI OTA, procured from the same vendor. Both mirror substrates and the metering structure are composed of Silicon Carbide (SiC). SiC is ~ 4.5 times as stiff as aluminum and has a low thermal expansion (~ 4 ppm/K), ensuring focus over the operational thermal range.

The metering structure consists of the spider and the bulkhead (Fig. 7), which are bolted together and painted with Aeroglaze Z307 for stray light mitigation. The spider supports the secondary mirror (M2) and the M2 baffle. The M2 is attached to the spider by a flexurized invar mount. The aperture stop, the primary mirror (M1), and the M1 baffle are mounted to the bulkhead. M1 is attached to the bulkhead via invar bipods. The metering structure is integrated into the graphite composite optical bench that contains titanium flexures to dynamically isolate the telescope from the gimbal interface.

Both mirrors are coated with a proprietary high reflectance $\text{TaO}_5/\text{SiO}_2$ dielectric coating. This reflective coating provides an average of $>99\%$ reflectivity across the spectral range at an angle of incidence (AOI) of 0° with limited spectral dispersion out to an AOI of 30° . Reflective and anti-reflective coatings were irradiated with gamma rays, 10–100 keV electrons, and 200 keV protons at varying fluences to demonstrate radiation hardness. All irradiated samples passed adhesion, humidity, and moderate abrasion testing. Maximum reflectivity loss was minimal, approximately 0.9% over AOI $5\text{--}12^\circ$. Although the ~ 10 μm coating thickness causes some wave-front error (WFE) deterioration at operational temperatures, OTA performance meets science requirements.

The lens assembly mitigates chromatic aberration and astigmatism inherent to the Ritchey-Chrétien design using three fused silica powered lenses (i.e., lenses that converge or diverge optical rays). The fourth element is a thick unpowered fused silica plug protecting the detector from radiation entering along the optical axis. The Corning 7980 fused silica is resistant to radiation darkening. Each fused silica optic is coated with radiation tolerant,

anti-reflective (AR) coating. The post-radiation AR sample only gained $<0.01\%$ reflectance at 10° AOI.

3.4.3 NAC Flight Cover Assembly (FCA)

The FCA (Fig. 5) is a one-time deployable mechanism consisting of an aluminum cover, a latch assembly, and a hinge assembly. The cover protects the optics from contamination and prevents damage to the OTA and detector in the event of unintended solar pointing during cruise. The NAC cover will be opened during cruise at ≥ 3 AU. The NAC cover contains two ports: a fused silica window for optical stimulation and a witness sample mount used to determine exposure to contamination during pre-launch testing. A labyrinth interface on the baffle tube hinders any particulate path, protecting sensitive optics. The latch assembly contains redundant, resettable, commercial off-the-shelf (COTS) pin-pullers providing a retracting force of 25 lbs without the use of pyrotechnics. Each pin-puller can be activated using separate spacecraft electronics. The pin is commanded to release by the spacecraft, and a swing paddle releases the flight cover. The spring-loaded hinge rotates the cover 270° , where it is caught with a hinge catch. A crush-block dampens the shock of the cover opening, and foreign object debris (FOD) is collected by a top hat cover. Redundant electrical switches provide cover position telemetry to the spacecraft electronics.

3.4.4 NAC Thermal Design

The detector operational temperature of $-60^\circ\text{C} \pm 1^\circ\text{C}$ and the rotary actuator and DE operational temperatures drive the powered portion of the NAC thermal design. Detector and DE power dissipation drive the radiative portion of the design. The NAC has nine thermal zones, of which eight are powered and controlled by the spacecraft and one by EIS. The trim heater, controlled by the DE and powered by the DPU, stabilizes the detector operational temperature. The OTA aperture, heat straps, and detector cold head provide cooling by radiating instrument-generated heat to space. Titanium brackets isolate the gimbal from the spacecraft nadir deck. The entire instrument is blanketed, from the FCA to the gimbal brackets. Consideration of the gimbal movement, PCS positions, and launch lock release drove the design and installation of the multi-layer insulation (MLI) blankets.

3.5 WAC Sensor Assembly

The WAC has four major subassemblies (Fig. 8; Centurelli et al. 2023; Lees et al. 2023): the OTA (Sect. 3.5.1), the FPM (Sect. 3.3.1), the DE (Sect. 3.3.3), and the DPU (Sect. 3.3.4). Three of the four assemblies are located on the spacecraft nadir deck, and the DPU is located in the spacecraft electronics vault.

The WAC OTA is mechanically integrated to the nadir deck via three titanium flexured feet, which have slots that accommodate nadir deck pins. The WAC DE has a separate mechanical interface to the nadir deck and an intra-instrument connector bracket.

3.5.1 WAC Optical Design and Performance

The WAC (Fig. 9) is an eight-lens refractive telescope, baffle, and a one-time deployable cover. The refractive element design contains four different materials: fused silica, CaF_2 , and two radiation resistant optical glasses. These materials were exposed to 1 Mrad of gamma radiation and the measured change in transmission was $<2\%$ (Centurelli et al. 2018). Each

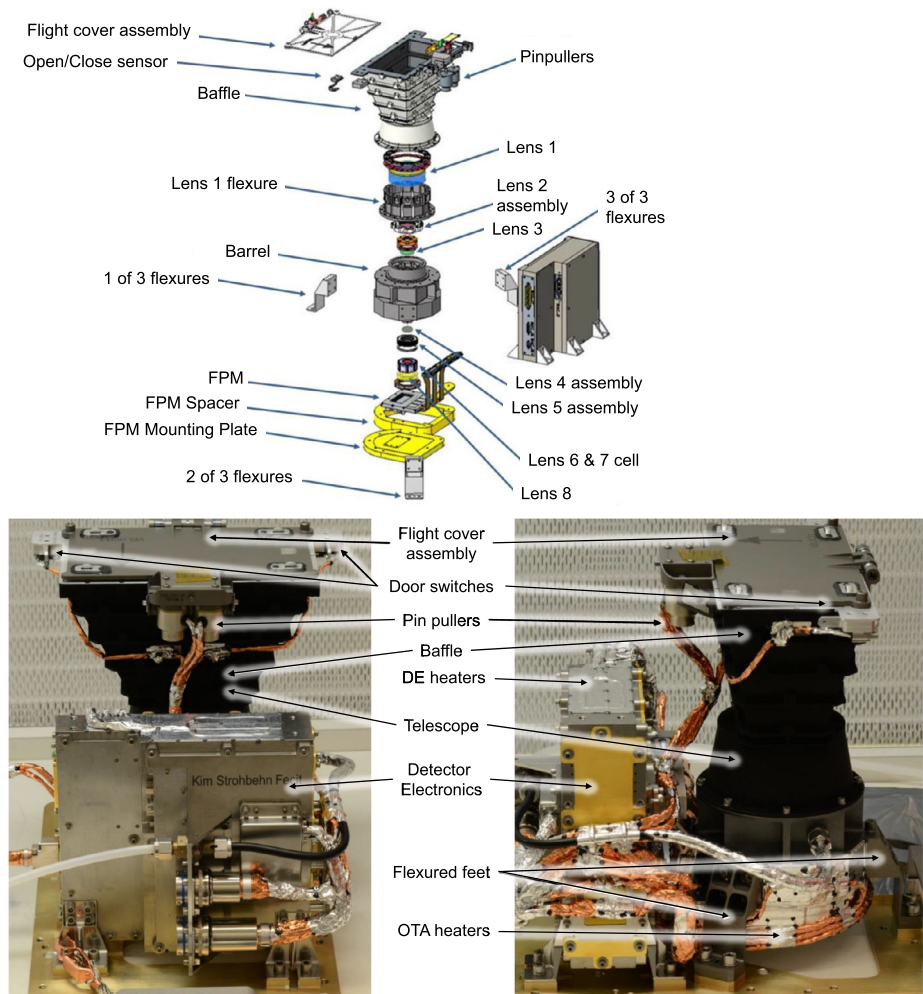


Fig. 8 WAC expanded diagram (top) and assembled flight hardware (bottom)

lens, except Lens 1 (L1), is AR coated with a prescription tested for durability and performance in varying temperature and radiation environments. L1 plays dual roles in the WAC telescope design: it is a powered lens, but it is also 25-mm thick fused silica, designed to protect the CMOS detector from radiation-induced noise. The outer surface is uncoated to limit darkening by the radiation environment.

The lens model designs vary depending on location in the stack and the size of the supported optic. Lenses 2, 4, and 5 (L2, L4, and L5) are bonded into titanium or stainless-steel flexures with NuSil CV4-2289-1, and L6 with MasterSil 973S-LO Silicone. Be-Cu axial springs position L1, L3, L7, L8 into titanium or stainless-steel flexures or retainers. An 8-mm-diameter stop located between L4 and L5 is machined into the L4 stainless-steel flexure. The L6 and L7 pair create the first stack, then that pair is nested into a secondary stack with L5 and L8. A titanium barrel surrounds the L2–L8 stack, and L1 sits on top of the barrel between the lower lenses and the baffle. The barrel protects the lenses and the CMOS detector

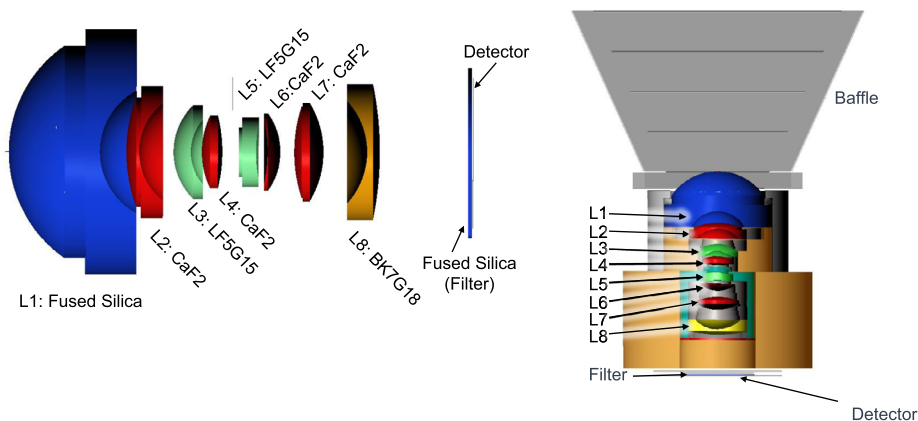


Fig. 9 Schematic illustration of the WAC telescope

from the radiation environment with ~ 35 -mm-thick Ti sides. Three flexed feet balance the barrel and interface with the nadir deck pins for precise positioning.

Although the edges of the FOV image observe at $\geq 24^\circ$ emission angle, the pixel scale is the same across the FOV (if we ignore planetary curvature). This design minimizes smear from the use of TDI.

3.5.2 WAC Flight Cover Assembly (FCA)

The one-time deployable cover consists of a light-weighted Ti alloy cover that interfaces to the baffle with a spring-loaded hinge. The cover protects the optics from contamination and prevents damage to the OTA and detector in the event of unintended solar pointing during cruise. The WAC cover will be opened during cruise at ≥ 2 AU. Redundant pin-pullers lock the cover. Each is individually wired to separate spacecraft electronics boxes. The spacecraft commands the pin pullers, and electric switches provide telemetry indicating the cover has opened completely.

3.5.3 WAC Thermal Design

Power dissipation of the detector and DE drive the radiative portion of the WAC thermal design. Aeroglaze 307 paint covers the inside and outside of the WAC baffle structure in order to radiate heat to space during operation. The WAC has three thermal zones: the spacecraft commands the OTA and the DE, and EIS commands the detector trim heater. The OTA has two pairs of heaters, one for survival and one for decontamination. The decontamination heaters serve three purposes: decontamination, warm up of the instrument from survival, and survival heater redundancy. The thermal gradient through the telescope is limited to $\sim 2^\circ\text{C}$ due to the mass of the barrel. The WAC has two blankets: the flight cover assembly blanket covers the pin pullers and the cover itself; the DE blanket surrounds the DE packaging and some of the harnessing.

4 Instrument Calibration and Predicted Performance

EIS science objectives require accurate ground calibration of both the NAC and WAC as well as continuing updates in flight during cruise and systematic measurements during science operations in Jupiter orbit.

4.1 Pre-Flight Calibration

The EIS team executed thorough ground calibration campaigns with each engineering and flight model instrument addressing the following major components: detector performance and validation, photon transfer analysis, bias levels, dark imaging, flat-field imaging, absolute and relative radiometric response, distortion, focus, MTF, stray light, and command parameter sensitivity (Table 8). Calibration measurements were acquired through both detector-level and instrument-level testing. Thorough detector characterization and command parameter sensitivity tests were conducted on the flight detectors prior to instrument integration, providing a robust assessment of the detector performance as well as any defects and artifacts for follow up during final calibration. Detector-level testing took place at APL with the detectors in a compact custom vacuum system, and instrument-level calibration was conducted at the APL Optical Calibration Facility (OCF) in two large custom vacuum systems. Both instrument- and detector-level testing were conducted at nominal operating temperatures ($-60\text{ }^{\circ}\text{C}$) with additional data collected at ambient (instrument level) and $-50\text{ }^{\circ}\text{C}$, $-70\text{ }^{\circ}\text{C}$, and $-90\text{ }^{\circ}\text{C}$ (detector level). Obtaining these reference data enables the conversion of the raw instrument data in engineering units (i.e., DN) to calibrated data in scientific units (i.e., radiance in $\text{W}/\text{m}^2/\text{sr}/\mu\text{m}$).

Because the flight DPUs and the cameras were tested independently in parallel, a frame grabber computer was used during calibration testing. However, during final calibration, extensive dark images and images of an MTF target were taken before and after integrating the flight DPUs for both instruments to ensure the validity of data taken with the frame grabber computer. No anomalies or additional noise were observed in this end-to-end test.

The WAC passed all Level-4 requirements levied on calibration, while the NAC passed all but one Level-4 requirement; a near-field stray light issue was identified during NAC final calibration. Optical modeling was able to reproduce the stray light issue, which occurs when the near-field region ($1.3\text{--}2.3^{\circ}$ off-axis) is illuminated by an extended source. A correction algorithm is under development. This issue affects the outermost two detector ports on either side along the cross-track axis. Despite the near-field issue, the NAC Level-2 requirements (and thus Level-1 requirements) are met or can be met with operational mitigations. The results of the ground calibration will be detailed in a separate, dedicated publication.

4.2 In-Flight Calibrations

The NAC and WAC largely share the same in-flight calibration plan with a few differences. NAC and WAC calibrations planned during cruise are summarized in Table 9. Point Spread Function (PSF) measurements will be taken from images of star fields in framing and color pushbroom mode for comparison to preflight data. Star observations during cruise will also be used to verify that the optical distortion models based on preflight data are still applicable, and to update estimates of the focal length and principal point coordinates. In-field stray light tests are planned, using distant Jupiter and/or Saturn in framing and color pushbroom mode. Out-of-field stray light and linearity tests will be done by pointing off Jupiter (by $\pm 1.5^{\circ}$, 5° , and 15° , NAC) and/or the Sun (by $\pm 10^{\circ}$, 25° , 40° , 55° , and 80° , WAC/NAC). Framing

Table 8 Summary of the performance of the NAC and WAC flight cameras in ground calibration

Title	Requirement	NAC Performance	WAC Performance
Bandpass	The EIS wavelength range shall cover the spectral passband between 400 nm to 1050 nm.	358 nm to > 1050 nm	370 nm to > 1050
Focal Length	The NAC shall have a focal length of 1000 mm \pm 1.0%. The WAC shall have a focal length of 46.0 mm \pm 0.5%.	NAC effective focal length (EFL) = 1003.55 mm (0.35%)	WAC EFL = 46.0078 mm (0.017%)
MTF	The system MTF shall be greater than 5.0% at all spatial frequencies less than or equal to 50 cycles per millimeter.	MTF performance >6.0% across the focal plane	MTF performance >7.0% across the focal plane
Distortion	The radial distortion shall be less than 1.0% NAC / 10.0% WAC across the entire FOV.	Avg residual distortion = 0.16% Max residual distortion = 0.90%	Max residual distortion = 3.11%
RGB Color SNR	For RGB color datasets, the SNR shall be 100:1 for I/F greater than or equal to 0.2.	Flight-like cases meet SNR requirements	Flight-like cases meet SNR requirements
Plume Search SNR	For Plume Search dataset, the SNR shall be 10:1 for I/F greater than or equal to 0.01.		
Panchromatic SNR	For panchromatic datasets, excluding Plume Search, the SNR shall be 50:1 for I/F greater than or equal to 0.2.		
NUV, IR1, IMC Color SNR	For NUV, IR1, and IMC color datasets, the SNR shall be 20:1 for I/F greater than or equal to 0.2.		
Radiometric Uncertainty	The NAC radiometric uncertainty of the final NAC data product shall be less than or equal to 10.0%.	Flight-like cases meet most requirements; binning or along-track summing may be needed in some cases ¹	Flight-like cases meet most requirements; binning or along-track summing may be needed in some cases ²
Radiance Precision	The NAC radiance measurement precision, which is defined by the ratio of the radiance of one data product to the radiance of a contiguous data product, shall be less than or equal to \pm 2.0%.	Radiometric uncertainty of the NAC final data product = 6.6% All observed radiance precision measurements <1.7%	Radiometric uncertainty of the WAC data products =2.5% All observed radiance precision measurements \leq 1.9%

Table 8 (Continued)

Title	Requirement	NAC Performance	WAC Performance
In-field Stray Light (framing)	The in-field stray light, including scatter and ghosting, shall not exceed 3% NAC / 6% WAC of the average signal within an extended source when measured 5 pixels from the edge in the illuminated region.	Positions in the framing area exhibit stray light across the knife edge $\leq 2.75\%$	Positions in the framing area exhibit stray light across the knife edge $\leq 2.85\%$
In-field Stray Light (filters)	The in-field stray light, including scatter and ghosting, shall not exceed 8% NAC / 10% WAC of the average signal within an extended source when measured 5 pixels from the edge of the illuminated region.	All filters exhibit stray light across the knife edge $< 4.4\%$	All filters exhibit stray light across the knife edge $< 5.47\%$
Out-of-field Stray Light	The point source transmission (PST; defined as irradiance averaged over the focal plane divided by the irradiance at the aperture) for out-of-field stray light shall be as indicated in the following table, Out of Field PST for NAC: Angle of point source from boresight $> 30^\circ$, $PST < 2 \times 10^{-4}$ Angle of point source from boresight $> 50^\circ$, $PST < 5 \times 10^{-5}$	Not met under some illumination conditions – correction in development	Performance verified against requirements

¹Where NAC SNR requirements are not met for the NUV and IMC filters for the small-scale color dataset, pixel binning or along-track summing can improve SNR while reducing resolution

²Due to low short-wavelength throughput with the WAC optics (Table 3), the NUV filter is excluded from WAC requirements. Where WAC SNR requirements are not met for the IMC filter for the regional-scale color dataset, pixel binning or along-track summing can improve SNR while reducing resolution

Table 9 NAC and WAC calibrations during cruise. (Frequency will typically be annually, but specific scheduling depends on spacecraft activities)

Calibration and Target	Mode* & Camera Parameters	NAC Calibration Spacecraft (S/C) & Gimbal Behavior	WAC Calibration S/C behavior
Geometric	Framing	Gimbal pointing	S/C pointing
Radiometric	Framing, Color pushbroom 3 detector temperatures	S/C and/or gimbal pointing S/C scanning	S/C pointing S/C scanning
PSF + in-field stray light	Framing, Color pushbroom	S/C and/or gimbal pointing S/C scanning	S/C pointing S/C scanning
MTF + in-field stray light	Framing 2 exposure times	S/C and/or gimbal pointing 6 positions on detector, including some covering the color filters	S/C pointing 6 positions on detector, including some covering the color filters
Out-of-field stray light	Framing 2 exposure times	S/C and/or gimbal pointing: $\pm 25^\circ, 40^\circ, 55^\circ, 80^\circ$ from Sun $\pm 0^\circ, 1.5^\circ, 2^\circ, 2.5^\circ, 5^\circ, 15^\circ$ from distant Jupiter cross- and along-track	S/C pointing: $\pm 10^\circ, 25^\circ, 40^\circ, 55^\circ, 80^\circ$ from Sun cross- and along-track
Linearity	Framing 5 exposure times	S/C and/or gimbal pointing: 1.5° from Jupiter	S/C pointing 40° from Sun
Darks (can be done with cover closed)	Framing 5 detector Ts, 2 exp times 5 exposure times	S/C and/or gimbal pointing S/C scanning	S/C pointing S/C scanning
Gimbal repeatability	Framing	S/C and/or gimbal pointing, gimbal stepping	N/A

*Framing calibrations also apply to pushbroom images

images of the limb of Jupiter will provide both MTF and in-field stray light measurements to assess true flight performance in comparison with ground data. Well-characterized calibration stars will be used to update the radiometric calibration and to track radiometric performance over the course of the mission. The same stars will be re-imaged at regular intervals and at varying detector temperatures during cruise and in Jupiter orbit in framing and color pushbroom modes. Dark current will be monitored both as a function of exposure time and temperature, and dark images will be collected at regular intervals in framing mode to provide an updated dark table. Bias frames will also be taken. NAC gimbals geometric and repeatability calibrations will be conducted using star fields in framing mode. These flight calibrations provide the basis for any additional corrections and/or updates to the calibration tables implemented in the calibration pipeline. All calibrations are generally planned to be repeated at least annually.

After Jupiter orbit insertion (JOI), additional calibration opportunities will be possible before Europa flybys begin. NAC and WAC calibrations planned in orbit at Jupiter and during satellite flybys are summarized in Table 10. Early pushbroom observations of extended targets will be used to refine the focal length corrections for the color filters. Radiometric, PSF, linearity, and gimbal calibrations will be repeated regularly during flybys to ensure that performance is monitored and any degradation in performance can be accommodated with calibration table updates or operational mitigations where possible. The flat fields are the most complicated calibration tests in flight, involving slewing across Jupiter in framing mode. MTF and in-field stray light measurements will be done using framing images of Jupiter (WAC) and a Jovian moon (NAC). Out-of-field stray light and linearity tests are repeats of the cruise calibrations. Dark current is monitored more closely in orbit at Jupiter, with framing dark images taken at different temperatures, exposures, and distances from Jupiter to capture the variation in radiation environments. With the exception of the flat-fields, all calibrations are planned to be repeated at least once per year, and up to four times per year for the radiometric calibrations.

5 Science Operations

EIS Science User Guidelines The purpose of this section is to help EIS science data users understand how the cameras work to the level needed to understand and analyze the resulting data products. A more detailed EIS Science users' manual is also available. EIS is a very capable digital camera system with tremendous flexibility, but there are limitations.

Definitions

- Line time: The time it takes for the image of a point on the target to move from one detector row to the next detector row. May be called “ground line time” for extra clarity. Line time varies as altitude changes during a flyby.
- Row time: The readout time for a detector row. May be called “detector row time” for extra clarity.
- Digital time delay integration (TDI): The DPU adds a specified number of detector rows (L) that image the same target point in L sequential frames, thereby increasing SNR by \sqrt{L} , with minimal additional smearing. (See also Sect. 5.2.)
- Detector exposure time (DET): The time a detector row is sensitive to light, before TDI.
- Summed exposure time (SET): The time a summed set of TDI lines is sensitive to light (i.e., with the TDI multiplier).

Table 10 NAC and WAC calibrations in Jupiter orbit. (Frequency varies depending on the type of correction, ranging from darks acquired during each flyby to flat fields taken only once or twice in Jupiter orbit, and specific scheduling depends on other observations and spacecraft activities)

Calibration and Target	Mode* & Camera Parameters	NAC Calibration S/C & Gimbal Behavior	WAC Calibration S/C behavior
Geometric	Star fields	Framing	S/C pointing
Radiometric	Calibration stars	Framing, Color pushbroom 3 detector temperatures	S/C pointing S/C pointing S/C scanning
Flat field	Slew across Jupiter (>5° diameter, at <30° phase)	Framing	S/C pointing
PSF	Star fields	2 exposure times for NAC	S/C scanning
MTF + in-field stray light	NAC: Bright limb of Jovian moon (subtending > 1000 pixels) WAC: Jupiter disk	Framing, Color pushbroom	S/C pointing S/C scanning S/C scanning
Out-of-field stray light	NAC & WAC: Deep space off Sun NAC: Deep space off Jupiter (<3.6° diameter, ≤90° phase)	Framing 2 exposure times	S/C pointing: ±10°, 25°, 40°, 55°, 80° from Sun cross- and along-track
Linearity	NAC: Deep space off Jupiter WAC: Deep space off Sun	Framing 5 exposure times	S/C pointing 40° from Sun
Darks	Star fields	Framing 5 detector Ts, 2 exp times 5 exposure times 5 orbital radii (different radiation), 3 exp times 1/flyby	S/C pointing S/C scanning
Gimbal repeatability	Star fields	Framing	N/A

*Framing calibrations also apply to pushbroom images

- Detector frame: The detector is always read out in “frames” consisting of a certain set of image rows, even for pushbroom images. This should not be confused with “framing mode” imaging.
- Frame time: The time between readout of subsequent detector frames. This is also the time between repeat samples of a detector row for TDI, so typically frame time is designed to match line time for pushbroom imaging.
- Framing mode (Sect. 5.1): Rolling shutter exposure and readout of multiple rows (typically the panchromatic framing area) in rapid succession. There is not a global shutter mode in which multiple rows are exposed simultaneously.
- Pushbroom mode (Sect. 5.2): Exposure and readout of rows as they pass over the surface. Can be used with or without TDI.

5.1 Framing Mode

Typical framing images are 4030×1536 -pixel, panchromatic-bandpass images, although smaller areas can be returned if the target of interest is small. The color areas could also be read out in framing mode, but with only 32 rows per color they are not very useful in this mode. To acquire frames, the detector is exposed and read out in rolling shutter readout mode, not simultaneously as instantaneous (global shutter) frames. As each row is exposed, it is read out with essentially no delay, minimizing radiation-induced noise. An entire panchromatic frame (1536 rows) can be read out in just 26 ms, so if the pointing is stable over 26 ms (or longer for longer exposure times) there would be no extra geometric distortions due to pointing jitter. However, spacecraft vibrations can result in jitter-induced image distortions, which can be corrected using the flexibility of the EIS detector readout (see discussion of check lines in Sects. 6.2.1 and 6.3.1).

5.2 Pushbroom Mode with TDI

EIS can use digital TDI for pushbroom imaging. In the standard mode of operation, the frame time and the line time are the same, allowing the digital processing unit (DPU) to add a number of neighboring detector rows, L , imaging the same target point in L sequential frames, increasing SNR by \sqrt{L} with minimal additional image smearing. L is the number of TDI lines or rows. There is some additional along-track smearing if the frame time and the line time are not matched, and cross-track smearing if there is misalignment of the direction of image motion with the detector columns. Pointing jitter can produce smear in both directions. The standard case is the same concept as charge-transfer analog TDI in a CCD (e.g., McEwen et al. 2007). However, there is an additional amount of read noise for every line summed for digital TDI rather than just one read noise hit via on-chip TDI; at best, the SNR after summing lines in the DPU is equal to $\text{SNR}(\text{single line}) \times \sqrt{L}$.

Digital TDI has the advantage of increased flexibility in frame time versus analog TDI. A useful mode of operation is along-track summing, which can also be called along-track undersampling. Along-track oversampling is also possible but only recommended for single-line pushbroom images.

Along-track summing uses frame time = $M \times$ line time, where M is an integer. It can be used to increase SNR near closest approach when line time is extremely short because the ground speed is fast and the ground sampling dimension is small, and where L is limited by the detector readout speed limit (see below). Image lines have M times the separation of image columns, since the sampling time is M times what's needed to take full advantage of the along-track detector resolution, and the raw image pixels have $M:1$ aspect ratio. Image

processing on the ground restores the correct aspect ratio for fully calibrated and higher-level data products. For a non-TDI detector, along-track summing would only gain a factor of \sqrt{M} in SNR, but the digital TDI detector gains a factor of M , because not only is the exposure time per pixel doubled, but the detector can read out M times as many TDI stages at the slower frame time without violating the detector readout speed limit (see Sect. 5.3). To match the image motion with the frame time, along-track summing TDI must add lines spaced by M lines in subsequent frames, rather than neighboring lines as in standard TDI. For example, for $M=2$, instead of reading out lines 100–107 for 8-line TDI, we read out lines 100, 102, . . . 130 (for $M \times 8 = 16$ TDI stages), so each line covers the same part of the scene and can be summed while producing a sharp image. EIS can read out twice as many TDI lines at this lower rate. However, this method will smear equivalent to 31 TDI stages if there are pointing jitter or alignment (twist) errors.

Oversampling uses frame time = $(1/N) \times$ line time, where N is an integer. Oversampling increases resolution a little bit in the along-track direction, to the degree resolution is limited by pixel sampling rather than the point-spread function from the optics/detector or pointing jitter. The MRO/CRISM team calls this along-track oversampling (ATO) mode (Fox et al. 2016). Data volume increases by N , but EIS can compensate with greater wavelet compression. This mode only works well for single-line pushbroom images because the DPU does not shift and sum lines as needed in this mode using TDI.

In general, the WAC will need fewer TDI lines or stages than the NAC for high SNR because the line time is $\sim 21 \times$ longer at the same range to target (and the F number is similar; Table 5). The WAC optical distortion is 3.11%, which means ~ 0.03 pixel of added smear per TDI line, strongly concentrated in the corners.

5.3 EIS Speed and Storage Limitations

EIS imaging and commanding must stay within multiple limits while trying to achieve the best performance. There are speed limits (detector readout, wavelet compression, and Spacewire data rate) plus on-board data storage and downlink limits.

The first speed limit is how fast data can be read out from the detector, ~ 19.5 MHz from each of 16 readout ports, for a theoretical maximum of ~ 312 Mpixels/s, although the actual limit is expected to be 284 Mpixels/s accounting for overhead in transmission (the packet protocol). This limitation is most severe near closest approach in a high-speed flyby (~ 4.5 m/s ground speed). Because the line time is very short for the NAC (Table 11), we need to use TDI lines even for bright scenes, so the SNR is limited unless we use the along-track summing described above, sacrificing along-track resolution. Each of the 16 readout ports covers 256 columns of the detector, so acquiring narrower images (such as only 2048 rather than 4096 pixels) does not have any detector speed advantage but can be used to reduce data volume to transmit to Earth.

The DPU is designed to keep up in real time for standard, anticipated imaging modes, including full-resolution panchromatic NAC imaging with 7 TDI lines at a ground speed of 4.5 km/s below 100-km altitude (sufficient for 50:1 SNR if scene $I/F > 0.2$). Ideally, the DPU processing can always keep up given the detector speed limit. However, there is a wavelet compression limit of ~ 115 Mpixel/s. For NAC stereo images acquired at < 100 -km altitude we need jitter correction, so rather than acquire a single image with 9 TDI lines, for example, we may choose to acquire three panchromatic images each with 3 TDI lines and separated by an appropriate number of rows (to be determined based on spacecraft stability in flight) to measure jitter. The images would then be summed on the ground to increase SNR. The wavelet limit of 115 Mpixel/s allows us to compress images with at least 3 TDI

Table 11 TDI constraints on a typical 4:1 resonance Europa flyby, for I/F = 0.2 (~70° incidence and phase angle (Dhingra et al. 2021)); some portions of the tour may be in a 6:1 resonance, with longer orbits and slightly faster flybys

Range (km)	FOV ground speed (km/s)	NAC			WAC		
		Pixel scale (m)	Max # lines from detector	Example image choice	Pixel scale (m)	Max #lines from detector	Example image choice
25	4.3	0.25 (or 0.5 × 0.25 with 2× summing)	4 (or 8 with 2× along-track summing; or 12 with 3×)	Clear only, 2× along-track sum, 8 TDI	5.43	96 (3 TDI clear × 3; 87 TDI lines for 5 colors)	3-line stereo, 3–5 colors (SNR low for IMC, assume no NUV image)
50	4.2	0.5	7 (or 15 with 2× sum)	Clear only, trade SNR vs. smear	10.9	384	3-line stereo, 5 colors, trade SNR vs smear
100	3.9	1	19	Clear only 7 TDI lines, plus jitter lines for stereo	22	many	3-line stereo, 5 colors, trade SNR vs smear
200	3.5	2	43	Clear, GRN, IR1	44	many	Same as above
400	2.5	4	120	Clear, BLU, GRN, RED, IR1, IMC	88	many	3-line stereo, 5 colors
800	1.9	8	320	Clear + 6 colors (SNR low for NUV)	174	many	3-line stereo, 5 colors (SNR very low for NUV)
1600	1.05	16	many	Same as above, or panchromatic framing images	349	many	Same as above
3200	0.45	32	many	Same as above	698	many	Same as above, or framing images
6400	0.16	64	many	Same as above	1395	many	Framing images
12,800	0.04	128	many	Framing images	2790	many	
25,600	0.023	256	many		5581	many	

lines collected at the maximum rate from the detector, and because observations will likely use ≥ 3 TDI lines to ensure sufficient SNR to make matches for jitter corrections, this rate is not expected to be limiting.

The second major speed limit is the transfer from the DPU to spacecraft BDS via Spacewire, limited to 130 Mbit/s for each camera. (Spacewire can operate faster, but there is a CPU margin limit in the DPU that limits us nominally to 130 Mbps.) Since the wavelet compression is not determinate (we can only estimate how many bits will result from various compression settings), margin will be needed. Exceeding the Spacewire speed limit results

in overwriting data, so we plan to stay within ~ 100 Mbps (depending on experience in estimating the compression ratio). Near closest approach we need to use wavelet compression to < 4 bits/pixel (or < 2 bits/pixel for stereo at 50-km altitude with two full images for jitter) for the NAC to keep the rate below 100 Mbps. A software tool will estimate data volume per observation, with the goal of $\ll 1\%$ chance of overwriting data.

Another major limit is total data volume, given the downlink rate and contact time from the spacecraft to the ground. Total data volume estimates during the tour for required science observations and calibrations are 760 Gb for NAC and 700 Gb for WAC (assuming compression to ~ 3 bits/pixel), or ~ 30 Gb per flyby, not including calibration data.

BDS end-of-life capacity is 537 Gb, but only ~ 100 Gb is currently estimated per flyby from all instruments to meet requirements. Data acquired during a flyby can be carried over for later playback, but hopefully BDS margins will always be high enough that the total storage space will not limit observations.

5.4 Balancing Exposure Times, TDI, and Gain States for Color Imaging

Detector exposure time (DET) is defined as the time a detector row is sensitive to light, before the TDI multiplier. TDI results in a Summed Exposure Time (SET). DET may be commanded to the value $(I \times \text{row time} - \text{overhead})$, where I is an integer between 1 and J , the total number of detector rows read out, and the overhead is $8.86 \mu\text{s}$. The row time can vary from $13.62 \mu\text{s}$ to 3.369 ms . Since $\text{frame time} = J \times \text{row time}$, the maximum DET is the frame time minus the overhead. The DET determines the total signal in electrons (e^-) on the detector, which we typically want to keep below detector full well ($\sim 21,000 e^-$ for high gain or $\sim 156,000 e^-$ for low gain (Table 6)). The SET determines the total DN value after TDI summing, which we typically want to keep below digital saturation ($16 \text{ bits/pixel} = 65,536$).

The sensitivities through color filters differ by a factor $> 10x$ from each other and $> 50x$ compared to panchromatic (clear) images. This wide range presents a challenge because every row must use the same DET. Ideally, we would achieve a high SNR (≥ 100) for every color filter, and we usually want unsaturated panchromatic images. Each image can have only one frame time and one DET (max = frame time), but we can vary the number of TDI lines to help balance SNR, up to the maximum of ~ 30 lines (there are 32 detector rows under each color filter, but we leave one row margin to avoid potential edge effects), and we can use high gain for the panchromatic image to alleviate saturation. For NAC color, the main limitation is detector readout speed, enabling fewer TDI (or jitter-correction) lines at lower altitudes and high ground speed, and the altitude limits to achieve a good SNR vary with scene brightness. A typical sequence for different altitude ranges is shown in Table 11. The WAC is only limited by detector speed at the lowest altitudes ($< 50 \text{ km}$) and over dark scenes such as near the terminator (or Jupiter-shine imaging).

Resolution can be reduced to increase SNR, which can be a useful trade for color imaging, especially for the NUV and IMC bandpasses. If SNR is so low that pixel summing on the ground will be needed for color analysis, then smearing over that pixel summing size is not a problem. Such smeared images should compress more efficiently, reducing data volume to the ground, analogous to acquiring pixel-binned images (but less lossy). EIS does not have the capability for binning pixels in the DPU because using wavelet compression is always more efficient and less lossy for the same compression ratio.

The EIS requirement for measuring Europa's subtle color variations is to achieve at least 100:1 SNR in the RED, GRN, and BLU filters and 20:1 in the NUV (NAC only), IR1, and IMC filters. We usually have ample margin on resolution requirements, so this can be

Table 12 Range to target, pixel scale, typical ground speed (4:1 resonance tour), and time to acquire 1000-line pushbroom (PB) image (with spacecraft nadir-pointed, i.e. not slewing)

Range (km)	Ground velocity (km/s)	NAC pixel scale (m)	Ground Line Time (ms)	Time to acquire NAC 1000-line PB image	WAC pixel scale (m)	Time to acquire WAC1000-line PB image
25	4.3	0.25	0.058	0.058 s	5.45	1.27 s
50	4.2	0.5	0.12	0.12 s	10.9	2.6 s
100	3.9	1	0.26	0.26 s	22	5.6 s
200	3.5	2	0.57	0.57 s	44	12.6 s
400	2.5	4	1.6	1.6 s	88	35.2 s
800	1.9	8	4.2	4.2 s	174	91.6 s
1600	1.05	16	15.2	15.2 s	349	332 s
3200	0.45	32	71.1	71 s	698	25.8 min
6400	0.16	64	400	400 s	1395	145 min
12,800	0.04	128	3200	53.3 min	2790	19.4 hr
25,600	0.023	256	11,130	185.5 min	5581	67 hr

traded with SNR. There is smear (along- and cross-track) from jitter, twist misalignment, orbit determination errors, and WAC optical distortion and planetary curvature, all of which can be exacerbated with more TDI lines. There is also smear from line time changes within each image segment. About 0.05-pixel smear per TDI line is a rough estimate for this trade. Thus, an observation with 28 TDI lines leads to 1.4-pixel of smear, or an effective ground resolution of 2.4 pixels. This means summing can be performed over 2.4×2.4 -pixel areas (on average) on the ground, increasing SNR by a factor of 2.4. A strategy for color image planning is to calculate the number of TDI lines needed to reach the desired SNR at the effective (smear) resolution. Since we can calculate single-line SNR (S1) from the predicted information, the optimal number of TDI lines (#TDI) can be determined by:

$$\#TDI \text{ lines} = 463 \times S1^{-1.3}$$

#TDI lines is then rounded up to the nearest integer. This strategy provides a preliminary automated method to choose the optimal number of TDI lines for each color in the WAC and NAC. The panchromatic stereo images can use the minimum number of TDI lines to get at least 50:1 SNR to preserve the best spatial resolution.

We will design sequences like the example in Table 11 as a function of I/F (which changes along a flyby as illumination and phase angles change) and line time. However, choosing to take fewer colors to manage data volume to the ground must also be considered.

5.5 Pushbroom Vs Framing Mode Selection

During fast, close flybys we need to use pushbroom imaging with TDI to get high SNR without major smear, and we must use this mode for color imaging and WAC ground-track stereo. When distant from the target and there is little relative motion, framing is best, unless the spacecraft is slewing. There are intermediate altitudes when either mode could be used. Once the time to acquire 1000-line pushbroom images (Table 12) exceeds more than a few minutes, framing mode is more reasonable. This effectively puts an upper limit on altitude for color imaging, except when the spacecraft scans across the target, for example the joint

scans at $>25,000$ km range (Sect. 6.3.2). Framing is reasonable at lower altitudes, as long as the line time is sufficient for a well-exposed and unsmear image. We must choose between pushbroom and framing mode when between ~ 1000 – 6000 km range with the NAC, and we could use framing mode even at very small ranges with the WAC (but this would interrupt pushbroom color and stereo).

5.6 Wavelet Compression

The wavelet compression algorithm is described in Hayes et al. (2009). The 16 data streams from the ports are processed in parallel and require 256×256 blocks of data to compress. Wavelet level and quantization parameters can be selected, but the actual data volume for each playback unit image (or Accountability Identifier (AID)) is indeterminate and estimates will depend on experience for different types of target scenes.

This wavelet compression is much better than the integer cosine transfer (ICT) compression used on Galileo SSI images. A test image (HiRISE polar ice image of Mars with high contrast) has been compressed to multiple levels and examined qualitatively. Compression artifacts are not obvious from side-by-side comparisons even at compression ratios up to 16:1 (1 bit/pixel), but effects on quantitative processing and analysis also need to be considered, as well as what effect it has on altering radiation-induced noise hits, thus making them harder to identify and remove.

Many cameras have 2×2 , 4×4 , etc. pixel binning capabilities. It makes sense for EIS to effectively bin along-track via frame times ($2 \times$, $3 \times$, etc.) greater than the line times because that increases SNR significantly. Digital binning in the DPU would result in much less effective compression than the wavelet algorithm, losing more information per degree of compression: e.g., 2×2 binning ($4 \times$ compression) produces an obvious loss of resolution, whereas $4 \times$ wavelet compression produces an imperceptible change, mostly compressing out random noise.

5.7 Science Planning and EIS Instrument Science Operations Center (ISOC)

5.7.1 Uplink Operations

Mission science planning and operations are discussed in Pappalardo et al. (2024, this collection) and Cangauala et al. (2024, this collection). Planning, sequencing, and commanding for EIS will be predominantly automated, although subject to approval and modification at each step. There are three elements to the EIS uplink process: 1) scheduling, 2) sequencing, and 3) generating commands. The scheduling process sets out the time periods that NAC and WAC will be observing, along with the associated resources (e.g., power, data volume, etc.) to allow the coordination of EIS observations with the activities of other instruments and spacecraft subsystems. Sequencing sets out the specific instrument configurations for each observation. The commanding process implements the sequences into products that can be uploaded to the spacecraft.

The automated scheduling process for EIS is done in cooperation with the planning tools developed for the entire mission. Before JOI, the mission will formulate a timeline, which will define (in a preliminary sense) the schedule of activities for the entire mission. The mission software will interface with the EIS automated scheduling software, SIMPLEX, to ensure compatibility of the NAC and WAC observations, the activities of the other instruments, and those of the spacecraft subsystems. The mission will provide information regarding timing and available resources. The completed NAC and WAC schedules will

detail each of the images that each instrument will take, along with the instrument mode (pushbroom or framing) and the gimbal positions for the NAC, if necessary. SIMPLEX will produce an automated schedule that can be modified by the EIS team.

Sequencing refines the scheduled observations by adding the detailed instrument configuration information necessary to take observations. The SIMPLEX sequencing software uses the geometry of the observation, modeled radiances, and a model of the instrument performance to determine optimal settings. These settings include gains, exposure times, lines to be read out / TDI, compression, downlink bins, etc. SIMPLEX records these settings and other observation metadata in the EIS iSOC database via an AID interface that receives and records the metadata and, in return, sends a list of unique AIDs back to SIMPLEX. SIMPLEX then associates each AID with a given sequence such that every image generated by the instrument for a given set of parameters will contain that AID. The results of automated sequencing can then be optimized by the EIS team. The result of the sequencing process contains all the information necessary to command the instrument and ensure every downloaded image will contain an AID that can be traced back to the original sequence.

Commanding is the automated process of transforming sequences into commands that can be uploaded to the spacecraft. This step will be fully automated, and the resulting commands will be tested on either an engineering model or the EIS software simulator developed by the EIS DPU team.

For each flyby, there will be a final ephemeris update ~ 2 days before closest approach. Any changes in altitude will inform final line times for EIS imaging, and updated tables will be uploaded to the spacecraft.

5.7.2 Downlink Operations

The EIS iSOC Database is an integral part of the Uplink and Downlink software and allows the iSOC to correlate downloaded images with planned observations. In order to do this, the Uplink software records EIS sequences and compiled commands via the AID Interface; the AID and associated metadata are then stored together in an AID table in the database. There is a unique AID for each raw image archived in NASA's publicly accessible Planetary Data System (PDS) as a raw data product. In cases where images are collected simultaneously, such as with pushbroom imaging (e.g., multiple colors, three-line stereo, jitter-correction images), each color, line (of the three-line stereo), and jitter-correction image is associated with a unique AID. On the downlink side, all packets containing the same AID are grouped together into an Accountable Data Product (ADP) file and sent to the iSOC. Upon receipt of the ADP file, the downlink software registers it in the iSOC Database where it will await automated processing into a raw image. Once created, the raw image is also registered into the iSOC Database to await automated processing into a calibrated image. The database also records intermediate states of the image during processing to enable the calibration pipeline to restart at an intermediate step in the event of an interruption or error in processing.

The database is also used to track the relationship between planned activities and the command sequences generated from those activities. As an example, a planned pushbroom observation may result in a command sequence that generates seven images, one for each color filter plus the panchromatic image (or up to 9 images for the WAC with three-line stereo). The database will track the pushbroom images from received ADP files, to raw images, and through to calibrated data products. The science team will then use a web interface that can query the database, determine the AIDs associated with the observation, and return the status of the images.

Table 13 EIS Quick-look Data Products

Data Product	Science Objectives	PDS4 Category*	Description
Raw data	all	Raw	Uncompressed images with PDS4 labels.
Framing images	all	Calibrated	Radiometric calibration applied to raw framing images; no pixel resampling (preserves full resolution).
Pushbroom image segments	geology, recent activity	Calibrated	Radiometric calibration applied to raw pushbroom images; no pixel resampling (preserves full resolution). Images through different color filters are not co-registered.
Map-projected framing images	all	Derived	Radiometric and geometric calibrations applied, including jitter corrections if needed; map projected.
Map-projected pushbroom image segments	geology, recent activity	Derived	Radiometric and geometric calibrations applied, including jitter corrections if needed; map projected.
Map-projected regional mosaics	geology, preview	Browse	Uncontrolled regional mosaics of overlapping NAC frames from within a flyby (matching illumination).
Plume-search database	recent activity	Derived	Table of plume-search results and detection limits, archived as a CSV file and in publications.

*PDS4 processing levels: Raw: uncompressed data with no processing; Calibrated: radiometric calibration applied in raw image geometry; Derived: radiometrically calibrated + map projected, and higher-level products; Browse: reduced resolution or special products

6 Data Products and Archiving

6.1 Overview

In this section we describe baseline and potential EIS data products, including how the data products will be produced and utilized. We also define which baseline products will be considered Quick-look Data Products (produced within two weeks of receipt of both science data and the ancillary data needed to generate them; Table 13) and which will be considered Collaborative Data Products, which are shared with the full Europa Clipper team prior to PDS archiving (Table 14). The EIS team plans a comprehensive set of data products (Patterson et al. 2019), but potential additional data products (Table 15) could be generated. Data release and archiving are briefly discussed at the end of this section.

6.2 Quick-Look Data Products

Quick-look Data Products (Table 13) will be produced by automated pipeline processing software that pulls data products from the Mission Operations Center and triggers processing as soon as the data for a particular product are complete. Most of the pipeline processing procedures are mature and used by other projects (e.g., McEwen et al. 2010; Perry et al. 2022). Much of the data processing will rely on the USGS Integrated Software for Imagers and Spectrometers (ISIS) software package (Sides et al. 2017, <https://zenodo.org/record/7644616>), which has been updated to process EIS images.

Table 14 EIS Collaborative Data Products (in addition to Quick-look products in Table 13)

Data Product	Science Objectives	PDS4 Category	Description
WAC DTMs	ice shell, geology	Derived	Preliminary DTMs from WAC 3-line stereo, plus orthoimages and slope maps.
NAC DTMs	geology	Derived	Using planned stereo (good convergence angles and matching illumination), plus orthoimages and slope maps.
NAC color image sets	composition, recent activity	Derived	Pushbroom image segments with up to 6 colors plus clear bandpass co-registered to subpixel level. No geometric control.
Joint scan NAC color products	composition, recent activity	Derived	Same as color image sets above but with absolute jitter corrections and preliminary geometric control.
WAC color image sets	composition	Derived	Pushbroom image segments with up to 6 colors plus clear bandpass co-registered to subpixel level. Orthorectified to preliminary WAC DTMs. Cover flyby strip at scales of 5, 10, 20, 40, 80, 160, or 320 m/pixel.
Global panchromatic mosaic at 50-100 m/pixel	geology	Derived	Global mosaic incrementally improved after each flyby, preliminary geometric control.
Global color mosaic at 300 m/pixel	composition	Derived	Global mosaic in ≤ 6 colors and clear, preliminary geometric control, NAC and WAC color.
Shape of Europa	ice shell	Derived	Limb fit solutions: tables of line-sample coordinates in images, tables of lat-lon-radius values per profile, and local control networks for each set of images used to make a multi-image profile; can be combined with REASON altimetry and UVS occultations to model low-frequency shape of Europa; spherical harmonic coefficients.

6.2.1 Standard Data Products: Raw, Calibrated, and Derived Images

EIS image data products are organized based on PDS4 data processing level. Raw image data products consist of a binary file containing the unprocessed image as a 2D array with PDS labels that contain ancillary data describing the detector state, e.g., gain, imaging mode, temperature of the focal plane module. Raw image refers to either a raw framing or a raw pushbroom image. In addition to traditional framing images, separate images are created from extra rows of data taken for jitter measurement, referred to as Check-line images (Kirk et al. 2018). Framing images taken at the masked top and bottom edges of the detector (referred to as masked-row images) are taken regularly to be used in the radiometric calibration pipeline; data from the masked columns at the edge of each row are always used as part of the calibration pipeline. NAC pushbroom observations may include discrete narrow (256-pixel wide) pushbroom images for jitter measurement, which are produced and archived as separate images at the raw processing level.

NAC pushbroom observations will be acquired in relatively short time periods with little change in ground line time. However, the WAC pushbroom sequence will be very long, acquired nearly continuously along the flyby ground-track, with pixel scale varying from as much as ~ 500 m to a little as ~ 5 m. For these sequences, the line readout time must be re-calculated at intervals to match the rate of motion of the ground to minimize smearing,

Table 15 Potential Additional EIS Data Products

Data Product	Science Objectives	PDS4 Category	Description
NAC and WAC regional panchromatic mosaics	geology	Browse	Mosaic data from multiple flybys to cover regions of interest at better resolution than global mosaic.
Global mosaic for morphology	geology	Browse	Global mosaic of best images with high incidence angles to accentuate topography.
Non-standard NAC DTMs	geology	Derived	Using additional stereo images with non-ideal geometry for more coverage, plus orthoimages and slope maps.
Improved WAC DTMs	ice shell, geology	Derived	Reprocess DTMs from WAC 3-line stereo manually to improve quality, plus orthoimages and slope maps.
Global map of Bond Albedo	recent activity	Derived	Bond albedo used with E-THEMIS data to identify subtle endogenic thermal anomalies; requires MISE data along with EIS.
Legacy datasets	all	Derived	Precision geodesy to recreate global and regional maps and DTMs with most accurate control at end of mission.
Stereo anaglyphs	outreach	Browse	Qualitative viewing of topography.
3-color outreach products	outreach	Browse	RGB natural color; 1MC, IR1, NUV for extended color and to map coarse-grained ice.
Merged color	outreach	Browse	Merge color mosaics with higher-resolution panchromatic mosaics.
WAC flyover movies	outreach	N/A	Zoom movies towards and away from Europa for each flyby using WAC color and stereo anaglyphs.
Interpolated altimetry data	geology	Derived	Interpolated altimetry data which preserve more local detail than spherical harmonics (e.g., Corlies et al. 2017).

especially when using TDI. Each reconfiguration of the EIS instrument to reset line times (and other parameters such as the number of colors and TDI lines) results in the generation of separate images; the instrument cannot generate a single raw image where line time is varying from row to row. So, the pushbroom sequence is created as a series of separate raw images (referred to as raw image segments to reflect that each raw image is part of a contiguously acquired pushbroom sequence), thus resulting in short gaps (<300 ms) in the otherwise continuous WAC pushbroom imaging for each flyby. However, these coverage gaps can be arranged to occur in different locations on the surface for each of the three WAC panchromatic lines (fore, nadir, aft), such that every location along the WAC strip will be imaged by at least one line and almost always two lines for stereo coverage. With three clear images for stereo and up to 5–6 colors, divided into perhaps two dozen segments, there will be a total of up to ~200 raw WAC pushbroom raw images per flyby.

The Standard Data Products are produced automatically by a data-driven software pipeline running at the EIS iSOC at APL. These include the Raw and Calibrated Data Products, and normally require no manual intervention to be generated. Instead, they are executed periodically and their tasks are determined by the arrival of new downlinked data, updated calibration tables, or updated SPICE kernels. The first task is the creation of the raw data products.

The following raw image data products are all reassembled from downlinked compressed image packets; each product is designated based on the content of the image data. These include raw images taken in framing or pushbroom mode (see 5.1 and 5.2); raw check-lines, images consisting of rows of the detector read out multiple times (check-line rows) and used in the geometric calibration process to correct very high frequency jitter; and masked-

rows, images containing the masked rows of the detector. Additionally for every framing, check-line, or masked-row image there is an ASCII, comma-separated value (CSV) lookup table that contains the index of the raw image row in relation to the index in the detector row. Lookup tables are not created for pushbroom images as each row in the pushbroom image consists of the same detector rows summed in TDI. Information on which regions of the detector were used to create the raw image is contained in the PDS4 XML label. The creation of all raw image products depends on the arrival of complete ADP files. If an incomplete ADP file is received, the iSOC will wait for a follow-up ADP file containing the rest of the AID packets. Once it is verified that an ADP file (or files) contains a full set of packets for a single image, the EIS iSOC can then generate the raw image data product.

A non-image raw housekeeping data product is also created by the software pipeline. The housekeeping data product consists of a time series of table records reporting the instrument health and status. Each table record is self-contained in a single housekeeping packet; therefore, it can be generated as soon as new housekeeping packets arrive at the iSOC. Since housekeeping data can be arbitrarily organized, the choice was made to have each housekeeping data product contain the housekeeping data collected for a given day. In the event a housekeeping data product is incomplete, the automated pipeline will regenerate it as more data are downlinked for a given day.

Successive automated tasks generate the Calibrated Data Products. The iSOC calibration pipeline queries the database to determine if new raw image products exist. Every new raw image is then processed by the calibration pipeline to create radiometrically calibrated images. The geometric calibration and reprojection process is applied to the calibrated images as updated SPICE kernels become available. Geometric and higher-level image processing is done via ISIS applications, orchestrated by the pipeline processing system, and archived as derived data products. The automated pipeline will also check for the existence of new or updated raw housekeeping data and generate calibrated housekeeping data products containing values in engineering units converted from raw DN values.

Every Standard Data Product mentioned above is also registered in the database to provide feedback to the EIS Uplink and Science Teams and close the loop between the planned observations and actual data products generated from Uplink. This database also allows EIS Team Members to access and download current Standard Data Products via a web interface. The database is also used as needed in the production of higher-level data products.

6.2.2 Regional Mosaics

During each Europa flyby, mosaics will be generated from overlapping NAC frames, small-scale pushbroom segments, and the WAC pushbroom sequence (with many Standard Data Product segments). Quick-look regional mosaics are important as they will often provide the highest-resolution coverage to date of those areas and thus inform planning of future observations. These mosaics at 10–100 m/pixel scale will be incorporated into the global mosaic (Sect. 6.3.3).

The pipeline will search the database for NAC frames acquired close together in time, run the ISIS programs *findimageoverlaps* and *autoseed* to collect match points between overlapping frames (typically ~ 3 –100 m/pixel scale), then run ISIS *pointreg* to subpixel register the images using an area-based matching algorithm, then run ISIS *jigsaw* to adjust the camera pointing angles to provide good matches between frames, and finally create local (1–10 m/pixel) and regional mosaics (Fig. 10). No photometric correction is needed as the lighting conditions will be uniform when mosaicking images from a single flyby. See Perry et al. (2022) for description of this type of processing. Many of these NAC mosaics will be

Fig. 10 Example layout of a mosaic of NAC frames

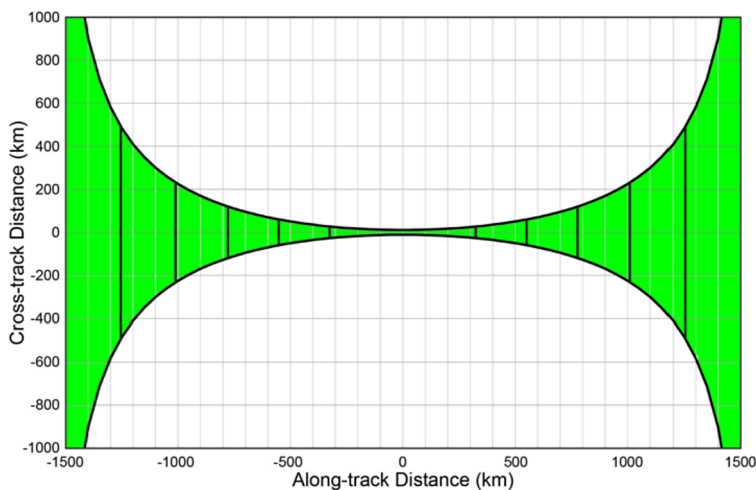
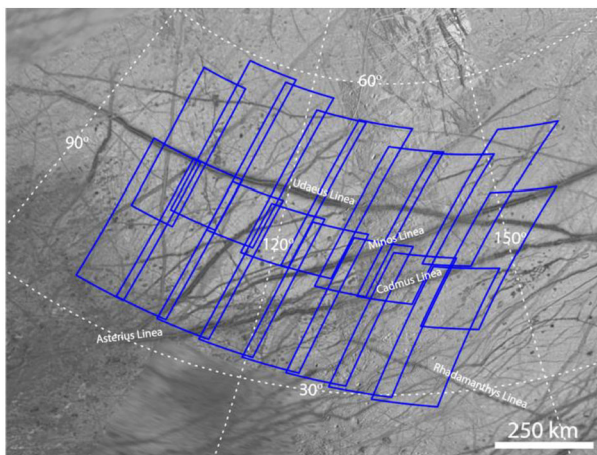


Fig. 11 Schematic of WAC imaging swath (green) showing planned mapping sections with standard scales of 5, 10, 20, 40, 80, 160, and 320 m/pixel. The data are oversampled by no more than 2× and file sizes are reasonable. The map sections are easily re-sized to combine into larger-scale mosaics

targeted to cover the closest-approach regions of future flybys to provide preview coverage needed to target the highest-resolution observations by EIS and MISE.

For the WAC, we will combine observation segments to create map-projected products. Because the imaging scale varies from 5 to ~500 m/pixel throughout a flyby, a single map projection of the entire strip at the scale at closest approach would be an enormous file containing mostly null values, and would be highly oversampled at the high-altitude ends. Thus, we plan to divide each strip into sections in which raw pixel-scales vary by a factor of two, with no more than 2× oversampling. These scales will be 5 m/pixel for raw data at ≤10 m/pixel, 10 m/pixel for raw data at 10–20 m/pixel, and so on for 20, 40, 80, 160, and 320 m/pixel (Fig. 11). Note that these map-projected *sections* are different from the raw image *segments* with different row times (Sect. 6.2.1). For a single flyby, WAC sections will use an oblique cylindrical projection, which is equivalent to a Mercator projection that is aligned

to the great circle that approximates the flyby trajectory. We will also use an equirectangular projection to mosaic or compare data from multiple flybys. The Quick-look product will be panchromatic only, as co-registered color products require extra processing time.

6.2.3 Plume-Search Database

EIS will systematically search for plumes as a function of latitude, longitude, and true anomaly, as described in Sect. 2.3.1. The results will be tabulated including image ID, sub-spacecraft latitude and longitude, image scale, true anomaly, phase angle, color band (usually clear), and whether or not a plume is detected. If a plume is detected, the vent latitude and longitude can be estimated (with uncertainties), as well as plume height and brightness. It may also be possible to predict the dimensions of a potential surface deposit. The database will be updated frequently and shared with the full Europa Clipper team for planning and correlation with other observations.

6.3 EIS Collaborative Data Products

In addition to the Quick-look Data Products, there are collaborative data products that may take longer than two weeks to produce (Table 14).

6.3.1 DTMs and Jitter Correction

EIS DTMs will be valuable products for geologic and geophysical analyses, decluttering simulations for REASON, and planning observations on subsequent flybys. They will also be essential for providing control for mosaics, and for orthorectifying non-stereo images and data from other instruments. DTMs will be generated using a combination of automated and interactive procedures. Multiple versions of control may be needed: 1) Relative control of the images of a stereo pair or three-line triplet will be needed to make matching possible for even the quickest processing; 2) a WAC strip could be controlled vertically and maybe also horizontally to a simultaneously acquired REASON profile as soon as a version of that is released; 3) the best absolute accuracy will be attained by controlling DTMs to a global controlled image mosaic base (for horizontal coordinates) and shape model (for elevation). Global control is anticipated to evolve throughout the mission as coverage for the image mosaic/control network is accumulated and shape information is acquired through limb fits (e.g., White et al. 2014; Sect. 6.3.4) and via REASON altimetry.

EIS can acquire stereo images in pushbroom or framing mode, and does so either within a single flyby (thus with matching illumination) or on different flybys. Targeting and acquiring NAC stereo in framing mode can be achieved by using the gimbal to achieve a good convergence angle. In pushbroom mode, the WAC acquires three-line stereo along the ground-track (Fig. 12), and the NAC gimbal can be used in the along-track direction for targeting very-high-resolution stereo pairs near closest approach (Fig. 13). For stereo on different flybys, it will be best to minimize illumination differences between images to reduce the need to manually edit the DTM; differences in shadows can cause artifacts that require correction, and poorly matched illumination can also degrade the quality of the DTM (Becker et al. 2015; Kirk et al. 2016).

High-quality terrain models can be produced at ~ 4 times the source image pixel scale. Therefore, EIS NAC DTMs could be produced at a GSD of as low as $\sim 2\text{--}4$ m up to 1 km. WAC images and DTMs will provide context for the NAC and other remote sensing data

Fig. 12 Illustration of WAC three-line pushbroom stereo with 12° convergence angle between forward, nadir, and aft lines to achieve ~ 4 -m vertical precision over 32-m GSD from 50-km altitude

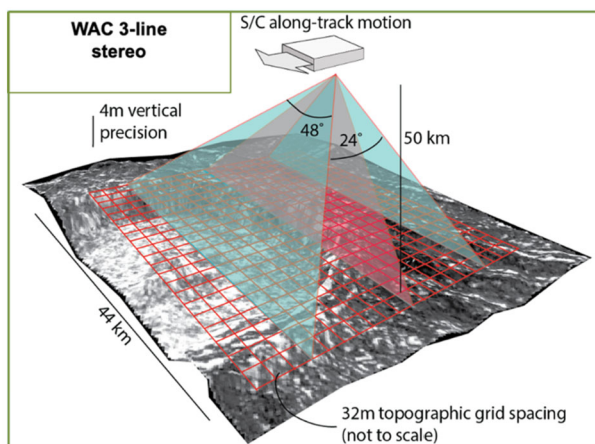


(Fig. 14), as well as providing a source of mapping control as the coverage of WAC DTMs increases during the mission.

WAC three-line pushbroom and the 24° along-track FOV allows for stereo observations to be made during the same flyby and with a consistent convergence angle (Fig. 12). Because of the large changes in pixel scale during a flyby, WAC DTMs will need to be processed in sections and resampled to a uniform pixel scale (Sect. 6.2.2; Fig. 11). These section boundaries will be determined by optimizing the rescaling so that image pixels are not under-sampled. DTMs will be produced at a GSD of 3–4 times the pixel scale of each section. Overlapping sections will ensure continuous coverage in the final DTM products. A complication to the WAC DTM production is the need to reset line times during the flyby to match the ground speed (Sect. 6.2.1), which will lead to small gaps at the image segmentation boundaries. The gaps will have two-line stereo (instead of three-line stereo), which could degrade terrain quality over these areas. The resulting WAC DTMs will have GSDs from 20–32 m up to ~ 1 km.

Pointing jitter corrections will be needed to produce high-quality DTMs from NAC pushbroom images and may also be needed for WAC pushbroom images and for framing images. Vibrations on the spacecraft (i.e., jitter) can cause geometric distortions in the image from line to line. Jitter sources on Europa Clipper may come from solar panel and antenna articulation, reaction wheels, or vibration from the thermal pump or cryocoolers for MISE or MASPEX. The nominal plan is to pause motions of the solar arrays before (accounting for spacecraft settling time) and during any EIS imaging. Although the distortions caused by jitter may not be readily visible in the images, they can introduce errors in stereo matching, leading to systematic artifacts in DTMs (Sutton et al. 2019).

We anticipate that the NAC will be especially sensitive to spacecraft jitter due to the small IFOV ($10 \mu\text{rad}$) and use of TDI during low-altitude, high-velocity flybys. The WAC, with a larger IFOV ($218 \mu\text{rad}$) is not anticipated to be as strongly affected by spacecraft jitter. However, if jitter were to be an issue for the WAC, similar correction strategies to those for the NAC could be applied. Early characterization of jitter can identify possible sources, and potentially lead to in-flight mitigation strategies (McEwen et al. 2010; Henriksen et al. 2016). The image line time and time between acquiring multiple lines on the same focal plane are used to derive the frequencies of spacecraft vibrations that affect the images (Sutton et al. 2019). Color filter lines as well as clear filter lines will be selected to optimize the frequencies that can be detected for correction (see detector layout in Fig. 4). The jitter

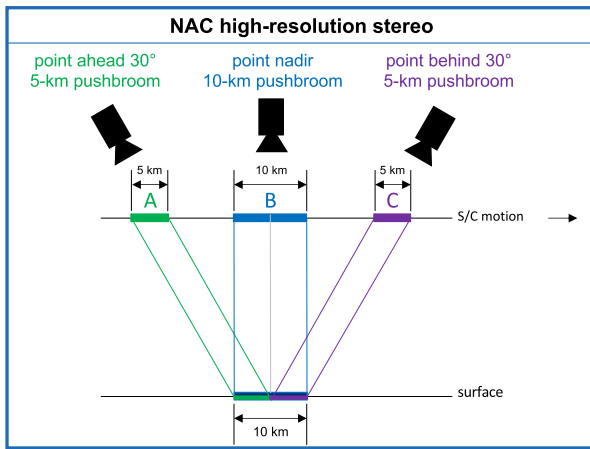


Fig. 13 Illustration of the NAC along-track pushbroom stereo sequence at an altitude of 50 km: the NAC is targeted 30° forward to acquire a 5-km-long pushbroom image; the NAC is then targeted nadir to acquire a 10-km-long pushbroom image, half of which overlaps with the forward image; finally, the NAC is targeted 30° aft to acquire a 5-km-long pushbroom image that overlaps with the second half of the nadir image. The three images combine to make two 5-km-long stereo pairs that will be used to generate a DTM with a GSD of 4 m and a vertical precision of ≤ 0.5 m

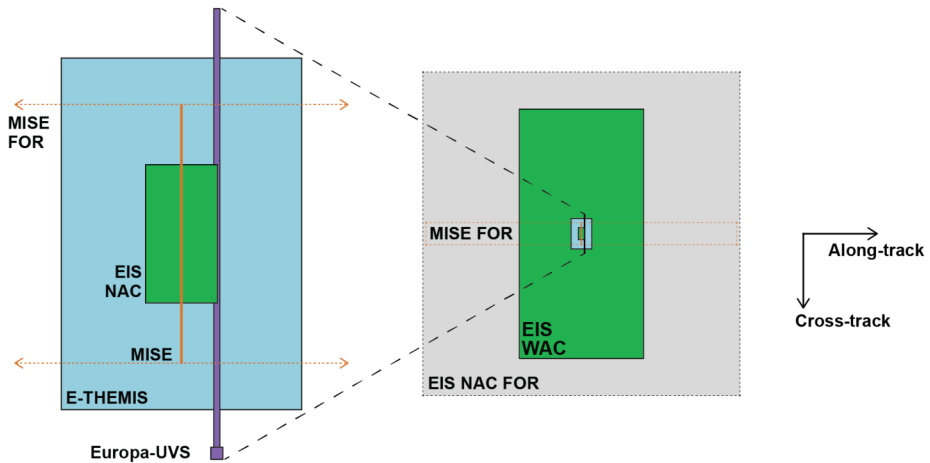


Fig. 14 Schematic of the relative footprint sizes and boresight alignment for the Europa Clipper optical remote sensing instruments. Pushbroom imaging by EIS, Europa-UVS, E-THEMIS, and MISE enables variable along-track image lengths. The NAC field of regard (FOR) is enabled by the $\pm 30^\circ$ along- and cross-track gimballs. The MISE FOR is enabled by a $\pm 30^\circ$ scan mirror

measurement and correction pipeline will be based on the operational end-to-end jitter correction process for HiRISE (Sutton et al. 2019), and the jitter characterization efforts will be similar to those adapted from HiRISE for the Lunar Reconnaissance Orbiter Narrow Angle Camera (LROC NAC) (Mattson et al. 2010, 2011).

The local-scale imaging (including stereo for candidate landing sites) presents a special challenge. Because of the high ground speed and detector readout limits (Sect. 5), we need

every line for TDI to achieve 50:1 SNR and therefore cannot acquire color images or extra lines of clear imaging to model jitter. We therefore will use an alternate strategy, such as acquiring two or three images each with 3 or 4 TDI lines, separated as needed to measure key jitter frequencies. Once the images have been carefully correlated, the data will be summed on the ground to produce a higher SNR image. To optimize this process, we will need testing in flight to understand what jitter frequencies to expect. The concurrent WAC imaging may provide some additional low-frequency jitter information but cannot resolve high-frequency jitter.

The framing mode of the EIS detector is implemented as rolling shutter readout of one line at a time, which minimizes radiation-induced noise but is subject to spacecraft jitter over the time the frame is read out (26 ms). Motions on the order of 1.5 NAC pixels could occur during imaging and readout of a frame, which would be undetectable in WAC images but would compromise science goals (geodetic control and limb profiling) that require subpixel precision measurements in NAC framing images. The NAC rolling shutter readout can be modified to obtain additional data that can be used to correct jitter distortions (see also discussion of check lines in Sects. 6.2.1). The sequential readout of detector lines will be interrupted periodically to read out one or more check lines repeatedly. Ground processing will include cross-correlation of these check lines with the primary image, yielding a time history of how the image shifted within the field of view. Coefficients describing the jitter will be stored in the image label and used to correct the internal distortions. Kirk et al. (2018) implemented this technique and showed that simulated jitter distortions added to real images of Europa could be modeled and corrected to an RMS accuracy of 0.1 pixel or better. Some experimentation will be necessary at the start of the tour at Jupiter to determine the optimal check-line locations on the detector and how often they should be read out to sample the jitter. These parameters may differ based on the vibration sources on the spacecraft that are active while the image is being exposed.

6.3.2 Color Products

The calibrated pushbroom image segments will be separate products for the panchromatic and color bandpasses, each covering a slightly different portion of Europa. In theory, the map projections will account for these offsets, but probably not to the sub-pixel level based on only the spacecraft engineering data. This whole-image offset plus any pointing jitter will result in color fringing. We will correct these offsets in the NAC by along-track shifting and warping to make each color match one of the original images such as the clear bandpass, as done for HiRISE (McEwen et al. 2010). This method assumes that parallax differences between colors are insignificant, which is likely true for NAC images but not WAC images. The WAC color therefore requires DTMs to produce orthoimages in each color, at least at higher resolutions, which may then need additional processing to reach subpixel co-registration.

Of special interest are the NAC full-disk color observations produced from the joint scans at ~ 250 – 400 m/pixel (Fig. 15), because this is the best dataset to look for color or photometric anomalies or changes over time that suggest recently or currently active processes. In order to compare scans from different flybys, the datasets must be controlled to the best available global map.

6.3.3 Global Mosaics

Creation of the global mosaic of Europa will make use of the best panchromatic NAC and WAC images acquired over the course of the mission. The eventual control network for this

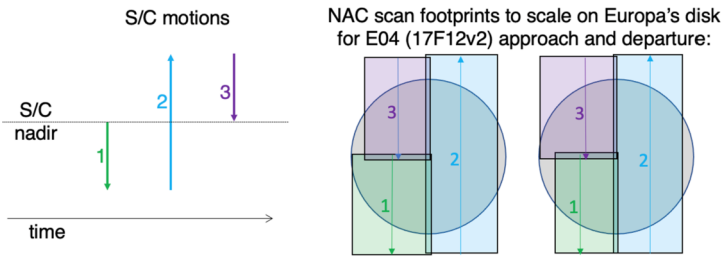


Fig. 15 NAC can cover nearly the full disk of Europa at 25,000–40,000 km range for the joint scans with other remote-sensing instruments by using gimbal pointing to offset the FOV during 1) the initial spacecraft slew to point off the edge of the disk of Europa, 2) the constant-rate spacecraft scan across Europa, and 3) the spacecraft slew back to the center of Europa's disk. Scans 1 and 3 have non-constant velocity, so image segments may be needed to change line time. (The example geometry is based on an earlier but similar version of the trajectory: 17F12_V2)

mosaic will be based on the geodesy dataset (Sect. 6.4). Global- and regional-scale images will be photogrammetrically tied to the geodesy dataset and to each other. In practice, semi-automated local and regional photogrammetric control of images will occur throughout the mission (e.g., after each flyby), with only periodic updates to the global solution. This approach ensures that image locations are accurate relative to one another (enabling geologic analysis throughout the mission), and approximately correct globally. Development of the final global photomosaic will then require a final photogrammetric solution after data acquisition is complete, based on the best available images at a given location. Images will be reprojected using the best available global shape model of Europa (Sect. 6.3.4). An equirectangular projection will be used at latitudes between $\pm 60^\circ$ and polar stereographic projections for higher latitudes. Although we expect the global photomosaic to be produced at a scale of 50–100 m/pixel, the approach will result in the photogrammetric control of nearly the entire EIS dataset. Higher-resolution images and color data can therefore be used seamlessly with the mosaic.

Of importance to the creation of the global mosaic is photometric correction of the images. Photometric correction preserves the scientific integrity of the radiometrically calibrated pixel values while accounting for changes in apparent surface brightness that result from differences in photometric angles (incidence, emission, and phase) during image acquisition. Given that the global image dataset will be acquired over multiple Europa flybys, large differences in illumination conditions are expected (see e.g., Bland et al. 2018 Fig. 17, for an example of a photometrically uncorrected mosaic of this sort). Application of an accurate photometric correction is therefore necessary to evaluate albedo or color differences across Europa's surface (e.g., McEwen 1986), to detect changes in albedo or color between two images of the same region taken at different times, to remove image seams within the mosaic, and to distinguish between topographic shading and surface albedo (McEwen 1991). Minnaert (Dhingra et al. 2021), Lunar-Lambert (McEwen 1986), Hapke (e.g., Belgacem et al. 2020), Lommel-Seelinger (e.g., Dhingra et al. 2021) and other photometric models (e.g., Buratti and Veverka 1983) have previously been applied to Europa; however, Europa's photometric behavior is complex, and may vary with region (Belgacem et al. 2020) and terrain type (Dhingra et al. 2021), so the details of the photometric model that will be applied to EIS images has not yet been determined. Substantial improvement in the fit to the photometric model will be enabled by the EIS data, especially the joint scans because they will cover large regions with a broad range of phase angles.

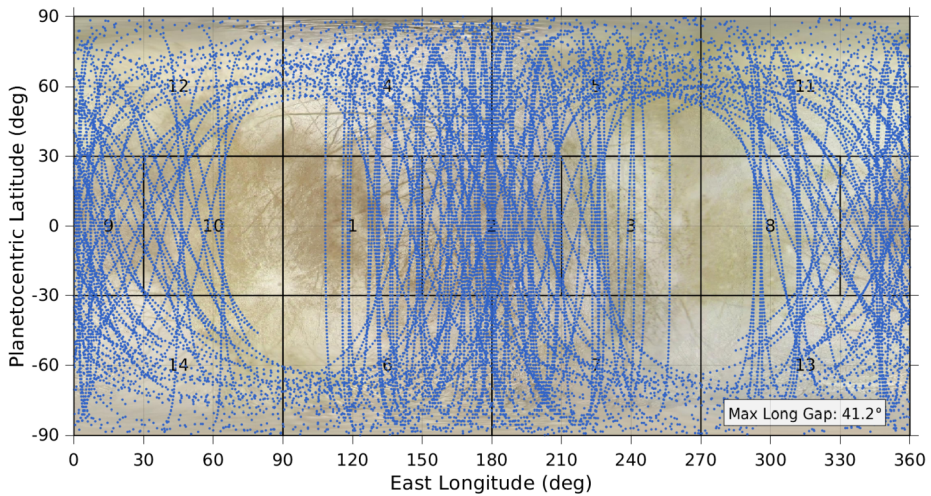


Fig. 16 Map of limb profiles observed by NAC and WAC in the baseline tour, 21F31_V6 (Pappalardo et al. 2024, this collection), at scales from 0.4 to 1 km/pixel, which are near ideal because the limb can be covered in a single image or small mosaics. The gaps near the apex and antapex of orbital motion can be filled in to some degree at lower resolution

The photogrammetrically relatively controlled, photometrically corrected mosaic must also be tied to the Europa cartographic coordinate system and geodetic reference frame. Europa's IAU-defined cartographic system is fixed by the location of the crater Cilix at a longitude of 182°W (178°E) (Archinal et al. 2018). Although the IAU-defined cartographic system for Europa (and all other satellites) is planetographic with west-positive longitudes (Hall et al. 1971), the Europa Clipper team has adopted a planetocentric, east-positive system. The EIS photomosaic will follow this standard; however, west-positive image labels will also be provided to the PDS to ensure consistency with older datasets. Note that because Europa's deviation from a sphere is small ($\sim 0.2\%$), the choice of planetographic or planetocentric coordinates does not affect latitudes. Out of necessity, the initial EIS photomosaic will utilize Europa's current geodetic reference frame (i.e., its reference ellipsoid and orientation relative to the International Celestial Reference Frame (ICRF)), which was derived from photogrammetric analysis of Galileo and Voyager images (Davies and Katayama 1981; Davies et al. 1998) and is summarized in Archinal et al. (2018); also noting that Bland et al. (2021) proposed a small modification to the location of Europa's prime meridian at J2000.0. However, the Europa geodetic reference frame is likely to be updated during the Europa Clipper mission as data from EIS, REASON (Blankenship et al. 2024, this collection), and the Gravity and Radio Science (GRS; Mazarico et al. 2023, this collection) investigations improve our understanding of Europa's shape and geoid. The final photomosaic will therefore use the best geodetic reference frame available at the end of the Europa Clipper mission.

In addition to the global panchromatic mosaic at 50–100 m/pixel, we will produce a global color mosaic at 300 m/pixel, using the best (smallest phase angle) NAC coverage from the joint scans, with photometric normalization. WAC color coverage may also be used to fill gaps or provide improved coverage such as over polar regions.

6.3.4 Global Shape Model

To derive long-wavelength global topography, the main datasets will be EIS limb profiles (Fig. 16) and REASON altimetry profiles (Blankenship et al. 2024, this collection). Roughly 20 individual REASON profiles are expected to be acquired and to have 2-km along-track resolution, 15-m vertical precision, and to extend for 1600 km. Supplementary information from Europa-UVS occultation point elevation measurements may also be included (Abrahams et al. 2021).

To generate a limb profile, the location of the local edge of the illuminated disk must be identified (Dermott and Thomas 1988), typically by scanning across a pixel row or column to where the DN value approaches within some fraction of the background (off-disk) value. Our approach will follow that used by New Horizons at Pluto and documented in Nimmo et al. (2017). Comparison of this approach with that of Thomas (2010) for Rhea images showed a median difference in limb location of 0.13–0.25 pixels. This is consistent with the expectation that the limb location can be fit to 1/5th of a pixel or better. In a single framing image that captures the full disk, the best expected limb profile pixel scale will be 0.8 km, implying a vertical precision of roughly 160 m at each pixel, but elevation trends over long distances can be estimated much more precisely based on multiple limb points. Using a mosaic of frames with smaller pixel scale to observe the limb would reduce both the local measurement error and the sensitivity to uncorrected jitter distortions, but could contribute long-wavelength distortions to the limb profile caused by mismatches in position and rotation between successive frames. Monte Carlo simulations (Steinbrügge et al. 2023) indicate that these errors are small compared to the expected slopes for mosaics with a moderate number of frames, particularly if extra images are centered to overlap each seam in the mosaic. Experiments early in the mission will be helpful to determine the optimal limb observation strategy.

Given a set of observations, the general approach to deriving the topographic spherical harmonic coefficients $C_{00}, C_{10}, C_{11}, S_{11}, C_{20}, C_{21}, S_{21} \dots$ is to solve the matrix equation:

$$X = (A_T \cdot A)^{-1} \cdot A_T \cdot Z$$

where $X = (C_{00}, C_{10}, C_{11} \dots)$, $Z = (h_1, h_2, h_3, \dots)$ are the observations of elevation at each measured point, and $A_{ij} = dZ_i / dX_j$. If the elevation data are sparse or have gaps, it may be necessary to include an extra regularization term, but this approach should be avoided if possible as it introduces biases into an otherwise closed-form problem. Further details may be found in Nimmo et al. (2011) and Abrahams et al. (2021).

6.4 Geodesy and Rotational Modeling

The primary approach to understanding Europa's rotation, needed both for mapping and as a potential constraint on geophysical modeling, is the construction of a global geodetic control network from overlapping images (Sect. 6.3.3). Once corresponding features have been measured in the image overlaps and any additional constraints such as elevations from a global shape model are available, photogrammetric bundle adjustment can be performed. This adjustment is a simultaneous least-squares estimation process for the ground coordinates of the features and improved camera pointing and/or position data for the images. Rotational parameters such as the amplitude of diurnal libration can also be solved for as part of the adjustment (e.g., Oberst et al. 2014). The images constituting the global image mosaic would be included in the adjustment, but the "backbone" of the global control network will be the images from the geodesy dataset, which are optimized for estimation of

the diurnal libration and obliquity. The delivered data products are the control network and the rotational parameters. The control network consists of image measurements, computed ground coordinates, improved camera orientation parameters, and uncertainty estimates for all of these. The rotational model consists of the pole orientation (including possible precession), rotation rate (possibly nonsynchronous), prime meridian definition tied to surface features, and amplitudes of the diurnal and possibly other librations. Properly estimating the precision with which these parameters can be recovered would require simulating the entire network, but simple scaling arguments give a rough idea of the precision that can be expected.

The geodesy dataset consists of a set of NAC framing mode images (corrected for internal jitter distortions as described above) forming a continuous “belt” through all longitudes at low latitude. Ideally, two independent belts would be acquired near the extremes of the diurnal libration (true anomalies 90° and 270°), but this is not achievable because of flyby geometry constraints. Using images with 10–50 m/pixel, along with some lower-resolution images where needed to fill coverage gaps (Table 2), a complete belt is planned for one sign of libration. Images with the opposite sign of libration will form an open belt spanning slightly less than the full 360° of longitude. Roughly 600 images would be needed to span the full longitude range at 10 m/pixel. Given that individual tie-points can be measured with about 0.2-pixel RMS precision (e.g., Kirk et al. 2016), neighboring images could be aligned to ~ 0.1 pixel by using several such features, but using a dense set of automatically measured tie-points (e.g., every 100 pixels) can reduce this to ~ 0.03 pixel. Relative errors in a belt of images accumulate as the square root of the number of seam offsets. Simulations (Steinbrügge et al. 2023) show that the maximum RMS error between the ends of an open belt is ~ 7 m, but the maximum error in a closed belt is only 3.5 m. The belt can also bend (by about 0.015° at each seam), leading to north-south errors of as much as 1 km (closed) to 3 km (open). These bending errors can be reduced by adding images to overlap seams or by broadening the belt; embedding the geodesy image belt in a global control network (as is planned) will effectively do the latter, reducing north-south errors to a level comparable to the east-west offsets, the expected internal precision relevant to cartography. Estimating libration amplitude rests instead on comparing the absolute positioning of images at different orbital phases by measuring large numbers of tie-points between the two belts. The absolute pointing knowledge for the NAC is 117 pixels (1σ) so the accuracy for measurements averaged over 600 linked images is $117/\sqrt{600} \sim 4.7$ pixels. Comparing two such image sets thus has a precision $\sqrt{2}$ as great, or 6.6 pixels, regardless of whether the sets close in longitude or not. Thus, if images could be obtained purely at the extremes of libration, the longitudinal shift could be measured with a precision of 66 m and the amplitude could be measured with a $1\text{-}\sigma$ uncertainty of 33 m. This uncertainty compares with the expected libration amplitude of ~ 150 m (Van Hoolst et al. 2013). The precision will be degraded somewhat by the practical need to use some images with larger pixel scales or at less-than-ideal true anomalies.

The precision of estimation for the obliquity is similar because obliquity also leads to an (apparent) variation in the location of surface features at the orbital period. The differences are 1) that at low latitudes the motions are primarily north-south rather than east-west, and 2) the true anomaly at which the excursions are greatest depends on the right ascension of the spin pole. If the images sample the optimal orbital phases, the motion could be measured to 66 m and the pole position to 33 m, equivalent to 0.0012° in declination, which may be compared with the expected obliquity of $\sim 0.05^\circ$ (Chen et al. 2014). A similar argument yields a rough estimate of the precision with which departures from synchronous rotation can be estimated. For a linear regression analysis of 600 apparent offsets spanning

the \sim four-year duration of the mission, the $1\text{-}\sigma$ uncertainty in the time derivative would be 6×10^{-6} degrees per day. This uncertainty may be compared with a precision of $\sim 10^{-5}$ degree per day needed to avoid aliasing of the degree-two gravitational field components (Mazarico et al. 2023, this collection). The apparent displacement caused by longer-period librations could potentially be measured at a similar level of precision, but if the Europa Clipper mission lasts only a fraction of a libration period, then the amplitude would be less well determined. In particular, it will not be possible to distinguish librations sampled over only a small fraction of a cycle from one another or from a purely secular nonsynchronous rotation rate. An alternative approach to estimating nonsynchronous rotation would be to compare the distance between local features and the terminator with those observed for the same features by Galileo or Voyager. This comparison provides a much longer temporal baseline, but the achievable precision is limited by the precision with which the terminator itself can be localized and does not benefit from the higher resolution achievable with EIS. Hoppa et al. (1999) found that the primary error source was the influence of local-scale topography on the terminator position and estimated a localization precision of 0.3° (8 km). It remains to be determined whether this precision could be improved by topographic mapping using EIS stereo pairs. If not, the rotational precision for terminator measurements would be several times 10^{-5} degrees per day.

6.5 Potential Additional EIS Data Products

6.5.1 Additional / Improved DTMs and Mosaics

The baseline plan is to produce DTMs from the best planned stereo sets of images, but there will be additional stereo coverage with non-ideal geometry that will provide unique coverage. In addition, the initial pipeline-produced WAC DTMs may be improved with better control and potentially by interactive editing to remove errors. Due to observing geometry and opportunities, the highest resolution images for the global mosaic are likely to include high-sun imaging that does not accentuate subtle topography. A low-sun only mosaic could also be produced, selecting only images with incidence angles greater than $\sim 50^\circ$ to best accentuate slopes. By combining images from multiple orbits and applying photometric normalization, mosaics could also be produced over regions of interest that are more complete than the regional mosaics from single orbits and higher in resolution than the global mosaic.

6.5.2 Bond Albedo Map

Bond albedo (or bolometric hemispheric albedo; Hapke 2012) is the fraction of solar power over all wavelengths that is scattered back into space, and it is essential for measuring or constraining internal heat flow from a planetary body and deriving the thermophysical properties of the surface. The observed thermal power (measured by E-THEMIS; Christensen et al. 2024, this collection) measures the sum of internal power released at the surface and re-radiated thermal power. Re-radiated thermal power is by far the largest term over all or most of Europa's surface, so mapping the internal power requires a very accurate Bond albedo map. A complete photometric model (how light is scattered in all directions over a hemisphere as a function of wavelength) is needed to derive Bond albedo from measurements of reflected light. The full-disk scans of Europa while approaching and departing from each encounter will provide an excellent dataset over most of Europa for deriving hemispheric albedo in each EIS color bandpass, accounting for $\sim 60\%$ of solar power, while

the MISE data (Blaney et al. 2024, this collection) can provide data from 0.8 to 5 microns. About 98% of the solar spectral power is thus covered by the combined EIS and MISE data. Bond albedo is then the weighted sum of hemispheric albedo in each wavelength region.

In theory, a Bond albedo map combined with E-THEMIS data (including derived thermal inertia) can be used to measure the internal heat flow over each surface resolution unit (limited by the local resolution of EIS, MISE, or E-THEMIS data). However, this result is the difference between two similar numbers, and that difference may be smaller than the errors. Very accurate radiometric calibrations and photometric and thermal inertia models are needed for robust results, as well as detailed knowledge of the solar spectrum, some parts of which are variable. If there are strong local thermal anomalies then this type of effort can quantify the local heat flow, as demonstrated for Enceladus (Howett et al. 2011). The Bond albedo map is also relevant to understanding a potential stable H₂O atmosphere on Europa's trailing hemisphere (Roth 2021).

6.5.3 Legacy Data Products

At end of mission, a final update to the global photogrammetric solution should be performed to provide a rigorously controlled, mission-encompassing image dataset that is tied to Europa's revised geodetic reference frame (including shape). The final control solution will permit reprocessing of DTMs such that they are spatially consistent with the updated image locations. When integrated with the final global shape model, the DTMs will enable the creation of a set of orthoimages that can then be photometrically corrected using revised photometric models (if necessary) and combined to generate a final orthoimage mosaic. These spatially consistent datasets, a geodetic coordinate reference frame, orthoimages and orthomosaic, and topography constitute a set of “foundational” (Laura and Beyer 2021) data products—a key spatial data infrastructure (SDI) component. The intent of these products would be to provide a set of legacy mission data that can easily be utilized for scientific analysis and future mission planning by the entire planetary scientific community without the need for extensive reprocessing of the data. As such they would be well suited to use through standard geospatial software (e.g., JMARS, <https://jmars.asu.edu>; Solar System Treks, <https://trek.nasa.gov>).

6.5.4 Outreach Data Products

Multiple additional products could be created for scientific visualization and public outreach. These include stereo anaglyphs (for WAC and NAC stereo); three-color products such as red-green-blue (RGB) natural color or 1MC-IR1-NUV for extended wavelengths; a merged global panchromatic mosaic (50–100 m/pixel) with the global color mosaic (300 m/pixel); and “family portraits” of Europa with Jupiter and other moons. All these products could be produced with automated pipelines for rapid release. In addition, the near-continuous WAC color/stereo coverage strip for each encounter could be used to produce movies zooming into, over, and away from Europa. These movies could be produced in RGB or other colors or with color stereo anaglyphs.

6.6 Data Release and Archiving

The data products generated by the EIS team fall into one or more of three main categories: archival data products, collaborative data products, and communications data products. The archival data products are validated and delivered to the Planetary Data System (PDS) as part

of a permanent archive of the mission dataset. Collaborative data products are data products shared among members of the Europa Clipper science team. These include Quick-look data products that must be delivered rapidly to plan future observations. Suitable Quick-look and Collaborative data products will also be delivered to PDS as archival data products, once final versions are available. Communications data products are created for release to the public through public outreach and can also be archived with PDS as browse products.

Generation of these three categories of data products follows the cadence defined by the Science Data Management Plan (Cangahuala et al. 2024 this collection). The communications data products will typically be generated as quickly as possible in order to make them available to the public. Data Analysis Tools developed by the EIS team will also be made available to the community, and the ISIS software is already publicly available and maintained (Laura et al. 2023; <https://zenodo.org/record/7644616>).

7 Summary

EIS will provide a comprehensive imaging dataset of Europa that will yield decades of discoveries and inform future exploration. The combined NAC and WAC accommodate variable geometry and illumination during rapid, low-altitude flybys, with both framing and pushbroom imaging capability to develop data products at scales ranging from distant plume searches, to global mapping at <100-m pixel-scale, to better than 1-m pixel scale high-resolution views, along with color and stereo. The cameras are designed to complement each other to address high-priority Europa science objectives and will also acquire important context images for the interpretation of data from the broad suite of investigations flying on Europa Clipper. Analysis of EIS data and collaborative science with other investigations will provide insight into Europa's global geology, the nature of the ice shell, and the potential for recent or even current activity, to explore Europa and advance our understanding of the habitability of this ocean world.

Acknowledgements The authors are deeply grateful to the team of hundreds of people who have worked on the design, build, testing, calibration, integration, and operational planning of the EIS cameras and the Europa spacecraft. We also wish to express our thanks to two anonymous reviewers whose careful reviews and suggestions improved the manuscript.

Funding This work was supported by the Europa Clipper mission, managed by JPL/Caltech under a contract with the National Aeronautics and Space Administration (80NM0018D0004). We also acknowledge the support of the NASA Instrument Concepts for Europa Exploration (ICEE) Program (NNX13AQ17G).

Declarations

Competing Interests The authors have no competing interests to declare that are relevant to the content of this article.

Open Access This article is licensed under a Creative Commons Attribution-NonCommercial-NoDerivatives 4.0 International License, which permits any non-commercial use, sharing, distribution and reproduction in any medium or format, as long as you give appropriate credit to the original author(s) and the source, provide a link to the Creative Commons licence, and indicate if you modified the licensed material. You do not have permission under this licence to share adapted material derived from this article or parts of it. The images or other third party material in this article are included in the article's Creative Commons licence, unless indicated otherwise in a credit line to the material. If material is not included in the article's Creative Commons licence and your intended use is not permitted by statutory regulation or exceeds the permitted use, you will need to obtain permission directly from the copyright holder. To view a copy of this licence, visit <http://creativecommons.org/licenses/by-nc-nd/4.0/>.

References

- Abrahams JNH, Nimmo F, Becker TM, Gladstone GR, Retherford KD, Steinbrügge G, Mazarico E (2021) Improved determination of Europa's long-wavelength topography using stellar occultations. *Earth Space Sci* 8(7):e2020EA001586. <https://doi.org/10.1029/2020EA001586>
- Archinal BA, Acton CH, A'Hearn MF, Conrad A, Consolmagno GJ, Duxbury T, Hestroffer D, Hilton JL, Kirk RL, Klioner SA, McCarthy D, Meech K, Oberst J, Ping J, Seidelmann PK, Tholen DJ, Thomas PC, Williams IP (2018) Report of the IAU working group on cartographic coordinates and rotational elements: 2015. *Celest Mech Dyn Astron* 130(3):22. <https://doi.org/10.1007/s10569-017-9805-5>
- Bart GD (2014) The quantitative relationship between small impact crater morphology and regolith depth. *Icarus* 235:130–135. <https://doi.org/10.1016/j.icarus.2014.03.020>
- Becker KJ, Brent A, Hare T, Kirk RL, Howington-Kraus E, Robinson M, Rosiek M (2015) Criteria for automated identification of stereo pairs. In: 46th Lunar and Planetary Science Conference, p 2703
- Becker HN, Lunine JI, Schenk PM, Florence MM, Brennan MJ, Hansen CJ, et al (2023) A complex region of Europa's surface with hints of recent activity revealed by Juno's Stellar Reference Unit. *J Geophys Res, Planets* 128:e2023JE008105. <https://doi.org/10.1029/2023JE008105>
- Becker TM, Zolotov MY, Gudipati MS, et al (2024) Exploring the composition of Europa with the upcoming Europa Clipper mission. *Space Sci Rev* 220:49. <https://doi.org/10.1007/s11214-024-01069-y>
- Belgacem I, Schmidt F, Jonniaux G (2020) Regional study of Europa's photometry. *Icarus* 338:113525. <https://doi.org/10.1016/j.icarus.2019.113525>
- Belton MJS Galileo Imaging Team (2000) Results of the Galileo solid state imaging (SSI) experiment. *Adv Space Res* 26(10):1641–1647. [https://doi.org/10.1016/S0273-1177\(00\)00110-1](https://doi.org/10.1016/S0273-1177(00)00110-1)
- Belton MJS, Klaasen KP, Clary MC, Anderson JL, Anger CD, Carr MH, Chapman CR, Davies ME, Greeley R, Anderson D, Bolef LK, Townsend TE, Greenberg R, Head JW, Neukum G, Pilcher CB, Veverka J, Gierasch PJ, Fanale FP, Ingersoll AP, Masursky H, Morrison D, Pollack JB (1992) The Galileo solid-state imaging experiment. *Space Sci Rev* 60(1):413–455. <https://doi.org/10.1007/BF00216864>
- Bierhaus EB, Zahnle K, Chapman CR (2009) Europa's crater distributions and surface ages. In: Pappalardo RT, McKinnon WB, Khurana K (eds) *Europa*. University of Arizona Press, Tucson, pp 161–180
- Bills BG, Nimmo F (2011) Rotational dynamics and internal structure of Titan. *Icarus* 214(1):351–355. <https://doi.org/10.1016/j.icarus.2011.04.028>
- Bland MT, Becker TL, Edmundson KL, Roatsch T, Archinal BA, Takir D, Patterson GW, Collins GC, Schenk PM, Pappalardo RT, Cook DA (2018) A new Enceladus global control network, image mosaic, and updated pointing kernels from Cassini's 13-year mission. *Earth Space Sci* 5(10):604–621. <https://doi.org/10.1029/2018EA000399>
- Bland MT, Weller LA, Archinal BA, Smith E, Wheeler BH (2021) Improving the usability of Galileo and Voyager images of Jupiter's Moon Europa. *Earth Space Sci* 8(12):e2021EA001935. <https://doi.org/10.1029/2021EA001935>
- Blaney DL, Hibbitts K, Diniega S, et al (2024) The Mapping Imaging Spectrometer for Europa (MISE). *Space Sci Rev* 220:80. <https://doi.org/10.1007/s11214-024-01097-8>
- Blankenship DD, Moussessian A, Chapin E, et al (2024) Radar for Europa Assessment and Sounding: Ocean to Near-surface (REASON). *Space Sci Rev* 220:51. <https://doi.org/10.1007/s11214-024-01072-3>
- Bray VJ, Collins GS, Morgan JV, Melosh HJ, Schenk PM (2014) Hydrocode simulation of Ganymede and Europa cratering trends - how thick is Europa's crust? *Icarus* 231:394–406. <https://doi.org/10.1016/j.icarus.2013.12.009>
- Buratti BJ, Veverka J (1983) Voyager photometry of Europa. *Icarus* 55:93–110. [https://doi.org/10.1016/0019-1035\(83\)90053-2](https://doi.org/10.1016/0019-1035(83)90053-2)
- Cangahuala LA, Campagnola S, Bradley B, et al (2024) Europa Clipper mission design, mission plan, and navigation. *Space Sci Rev* 220
- Cashion MD, Johnson BC, Gibson H, Turtle EP, Sori MM, Melosh HJ (2024) Europa's double ridges produced by ice wedging. *J Geophys Res, Planets* 129:e2023JE008007. <https://doi.org/10.1029/2023JE008007>
- Centurelli JL, Turtle ZP, Osterman SN, Slack KA, Roth DR (2018) Europa imaging system wide angle camera: the effect of gamma radiation on the refractive index and transmission of radiation resistant glasses. In: Proc. SPIE 10698, space telescopes and instrumentation 2018: optical, infrared, and millimeter wave, vol 106984D. <https://doi.org/10.1117/12.2313596>. (12 July 2018)
- Centurelli J, Slack K, Lees J, Turtle Z, McDermott J, Hawkins SE, Mize J, Meyer H, Ocasio Milanes A, Morgan P (2023) Europa Imaging System wide angle camera (EIS WAC) optical design, fabrication, and test. In: Proc. SPIE 12676, UV/optical/IR space telescopes and instruments: innovative technologies and concepts XI, vol 126760T. <https://doi.org/10.1117/12.2677462>
- Chen EMA, Nimmo F, Glatzmaier GA (2014) Tidal heating in icy satellite oceans. *Icarus* 229:11–30. <https://doi.org/10.1016/j.icarus.2013.10.024>

- Cheng AF, Weaver HA, Conard SJ, et al (2008) Long-Range Reconnaissance Imager on new horizons. *Space Sci Rev* 140:189–215. <https://doi.org/10.1007/s11214-007-9271-6>
- Choudhary P, Holt JW, Kempf SD (2016) Surface clutter and echo location analysis for the interpretation of SHARAD data from Mars. *IEEE Geosci Remote Sens Lett* 13(9):1285–1289. <https://doi.org/10.1109/LGRS.2016.2581799>
- Christensen PR, Spencer JR, Mehall GL, et al (2024) The Europa Thermal Emission Imaging System (E-THEMIS) investigation for the Europa Clipper mission. *Space Sci Rev* 220:38. <https://doi.org/10.1007/s11214-024-01074-1>
- Corlies P, Hayes AG, Birch SPD, et al (2017) Titan's topography and shape at the end of the Cassini mission. *Geophys Res Lett* 44(23):11,754–11,761. <https://doi.org/10.1002/2017GL075518>
- Costello ES, Ghent RR, Lucey PG (2018) The mixing of lunar regolith: vital updates to a canonical model. *Icarus* 314:327–344. <https://doi.org/10.1016/j.icarus.2018.05.023>
- Daubar IJ, Hayes AG, Collins GC, et al (2024) Planned geological investigations of the Europa Clipper mission. *Space Sci Rev* 220:18. <https://doi.org/10.1007/s11214-023-01036-z>
- Davies ME, Katayama FY (1981) Coordinates of features on the Galilean satellites. *J Geophys Res Space Phys* 86(A10):8635–8657. <https://doi.org/10.1029/JA086iA10p08635>
- Davies ME, Colvin TR, Oberst J, Zeitler W, Schuster P, Neukum G, McEwen AS, Phillips CB, Thomas PC, Veverka J, Belton MJS, Schubert G (1998) The control networks of the Galilean satellites and implications for global shape. *Icarus* 135(1):372–376. <https://doi.org/10.1006/icar.1998.5982>
- Dermott SF, Thomas PC (1988) The shape and internal structure of Mimas. *Icarus* 73(1):25–65. [https://doi.org/10.1016/0019-1035\(88\)90084-X](https://doi.org/10.1016/0019-1035(88)90084-X)
- Dhingra R, Buratti B, Seignovert B (2021) Europa Clipper preparatory photometry to constrain surface properties. *Planet Sci J* 2:144. <https://doi.org/10.3847/PSJ/ac06d6>
- Dombard AJ, McKinnon WB (2006) Folding of Europa's icy lithosphere: an analysis of viscous-plastic buckling and subsequent topographic relaxation. *J Struct Geol* 28(12):2259–2269. <https://doi.org/10.1016/j.jsg.2005.12.003>
- Dombard AJ, Patterson GW, Lederer AP, Prockter LM (2013) Flanking fractures and the formation of double ridges on Europa. *Icarus* 223(1):74–81. <https://doi.org/10.1016/j.icarus.2012.11.021>
- Elder CM, Douglass B, Ghent RR, Hayne PO, Williams J-P, Bandfield JL, Costello E (2019) The sub-surface coherent rock content of the Moon as revealed by cold-spot craters. *J Geophys Res, Planets* 124:3373–3384. <https://doi.org/10.1029/2019JE006128>
- Fagents SA, Greeley R, Sullivan RJ, Pappalardo RT, Prockter LM, The Galileo SSI Team (2000) Cryomagmatic mechanisms for the formation of rhadamanthys linea, triple band margins, and other low-albedo features on Europa. *Icarus* 144(1):54–88. <https://doi.org/10.1006/icar.1999.6254>
- Figueredo PH, Chuang FC, Rathbun J, Kirk RL, Greeley R (2002) Geology and origin of Europa's "Mitten" feature (murius chaos). *J Geophys Res, Planets* 107(E5):2-1–2-13. <https://doi.org/10.1029/2001JE001591>
- Fox VK, Arvidson RE, Guinness EA, McLennan SM, Catalano JG, Murchie SL, Powell KE (2016) Smectite deposits in Marathon Valley, Endeavour Crater, Mars, identified using CRISM hyperspectral reflectance data. *Geophys Res Lett* 43(10):4885–4892. <https://doi.org/10.1002/2016GL069108>
- Geissler PE, McMillan MT (2008) Galileo observations of volcanic plumes on Io. *Icarus* 197(2):505–518. <https://doi.org/10.1016/j.icarus.2008.05.005>
- Geissler P, McEwen A, Porco C, Strobel D, Saur J, Ajello J, West R (2004) Cassini observations of Io's visible aurorae. *Icarus* 172(1):127–140. <https://doi.org/10.1016/j.icarus.2004.01.008>
- Golombek M, Rapp D (1997) Size-frequency distributions of rocks on Mars and Earth analog sites: implications for future landed missions. *J Geophys Res, Planets* 102(E2):4117–4129. <https://doi.org/10.1029/96JE03319>
- Golombek MP, Huertas A, Marlow J, McGrane B, Klein C, Martinez M, Arvidson RE, Heet T, Barry L, Seelos K, Adams D, Li W, Matijevic JR, Parker T, Sizemore HG, Mellon M, McEwen AS, Tamppari LK, Cheng Y (2008) Size-frequency distributions of rocks on the northern plains of Mars with special reference to Phoenix landing surfaces. *J Geophys Res, Planets* 113(E3). <https://doi.org/10.1029/2007JE003065>
- Greenberg R, Hoppa GV, Tufts BR, Geissler P, Riley J, Kadel S (1999) Chaos on Europa. *Icarus* 141(2):263–286. <https://doi.org/10.1006/icar.1999.6187>
- Hall JS, Sagan C, Middlehurst B, Pettengill GH (1971) Physical Study of Planets and Satellites (L'étude Physique des Planètes et des Satellites). In: De Jager C, Jappel A (eds) Proceedings of the fourteenth general assembly brighton 1970. Reidel Publishing Company, Dordrecht, pp 128–137
- Hand KP, Phillips CB, Murray A, Garvin JB, Maize EH, Gibbs RG, Reeves G, et al (2022) Science goals and mission architecture of the Europa Lander Mission concept. *Planet Sci J* 3(1):22. <https://doi.org/10.3847/PSJ/ac4493>
- Hansen CJ, Esposito LW, Hendrix AR (2019) Ultraviolet observation of Enceladus' plume in transit across Saturn, compared to Europa. *Icarus* 330:256–260. <https://doi.org/10.1016/j.icarus.2019.04.031>

- Hapke B (2012) Theory of reflectance and emittance spectroscopy, 2nd edn. Cambridge University Press, Cambridge. <https://doi.org/10.1017/CBO9781139025683>
- Hayes JR, Strohbehn K, Murphy GA (2009) Low-cost wavelet image compression for FPGAs. In: Proc. SPIE 7455: satellite data compression, communication, and processing V 74550D. <https://doi.org/10.1117/12.826322>
- Head JW, Pappalardo RT (1999) Brine mobilization during lithospheric heating on Europa: implications for formation of chaos terrain, lenticula texture, and color variations. *J Geophys Res, Planets* 104(E11):27143–27155. <https://doi.org/10.1029/1999JE001062>
- Hedman MM, Gosmeyer CM, Nicholson PD, Sotin C, Brown RH, Clark RN, Baines KH, Buratti BJ, Showalter MR (2013) An observed correlation between plume activity and tidal stresses on Enceladus. *Nature* 500(7461):182–184. <https://doi.org/10.1038/nature12371>
- Henriksen MR, Manheim MR, Speyerer EJ, Robinson MS (LROC Team) (2016) Extracting accurate and precise topography from LROC narrow angle camera stereo observations. *Int Arch Photogramm Remote Sens Spat Inf Sci XLI-B4:397–403*. <https://doi.org/10.5194/isprs-archives-XLI-B4-397-2016>
- Hibbitts CA, Stockstill-Cahill K, Wing B, Paranicas C (2019) Color centers in salts - evidence for the presence of sulfates on Europa. *Icarus* 326:37–47. <https://doi.org/10.1016/j.icarus.2019.02.022>
- Hoppa G, Greenberg R, Geissler P, Tufts BR, Plassmann J, Durda DD (1999) Rotation of Europa: constraints from terminator and limb positions. *Icarus* 137(2):341–347. <https://doi.org/10.1006/icar.1998.6065>
- Hörz F, Cintala M (1997) Impact experiments related to the evolution of planetary regoliths. *Meteorit Planet Sci* 32(2):179–209. <https://doi.org/10.1111/j.1945-5100.1997.tb01259.x>
- Howard RA, Vourlidis A, Korendyke CM, Plunkett SP, Carter MT, Wang D, Rich N, McMullin DR, Lynch S, Thurn A, Clifford G, Socker DG, Thernisien AF, Chua D, Linton MG, Keller D, Janesick JR, Tower J, Grygon M, Hagood R, Bast W, Liewer PC, DeJong EM, Velli MMC, Mikic Z, Bothmer V, Rochus P, Halain J-P, Lamy PL (2013) The solar and heliospheric imager (SoloHI) instrument for the Solar Orbiter mission. In: Solar physics and space weather instrumentation V. SPIE, Bellingham, pp 155–167
- Howett CJA, Spencer JR, Pearl J, Segura M (2011) High heat flow from Enceladus' south polar region measured using $10\text{--}600\text{ cm}^{-1}$ Cassini/CIRS data. *J Geophys Res, Planets* 116(E3). <https://doi.org/10.1029/2010JE003718>
- Janesick J, Andrews JT, Elliott T (2006) Fundamental performance differences between CMOS and CCD imagers: part 1. In: High energy, optical, and infrared detectors for astronomy II. SPIE, Bellingham, pp 208–226
- Janesick J, Pinter J, Potter R, Elliott T, Andrews J, Tower J, Cheng J, Bishop J (2009) Fundamental performance differences between CMOS and CCD imagers: part III. In: Astronomical and space optical systems. SPIE, Bellingham, pp 47–72
- Janesick J, Pinter J, Potter R, Elliott T, Andrews J, Tower J, Grygon M, Keller D (2010) Fundamental performance differences between CMOS and CCD imagers, part IV. In: High energy, optical, and infrared detectors for astronomy IV. SPIE, Bellingham, pp 112–141
- Janesick JR, Elliott T, Andrews J, Tower J, Pinter J (2013) Fundamental performance differences of CMOS and CCD imagers: part V. In: Sensors, cameras, and systems for industrial and scientific applications XIV. SPIE, Bellingham, p 865902
- Janesick J, Elliott T, Andrews J, Tower J, Bell P, Teruya A, Kimbrough J, Bishop J (2014) Mk x Nk gated CMOS imager. In: Target diagnostics physics and engineering for inertial confinement fusion III. SPIE, Bellingham, pp 8–20
- Jia X, Kivelson MG, Khurana KK, Kurth WS (2018) Evidence of a plume on Europa from Galileo magnetic and plasma wave signatures. *Nat Astron* 2(6):459–464. <https://doi.org/10.1038/s41550-018-0450-z>
- Jiang X, Yang B, Li S (2018) Overview of China's 2020 Mars mission design and navigation. *Astrodynamic* 2(1):1–11. <https://doi.org/10.1007/s42064-017-0011-8>
- Johnson A, Cheng Y, Montgomery J, Trawny N, Tweddle B, Zheng J (2015) Real-time terrain relative navigation test results from a relevant environment for Mars landing. AIAA Guid Navig Control Conf. <https://doi.org/10.2514/6.2015-0851>
- Johnston SA, Montési LGJ (2014) Formation of ridges on Europa above crystallizing water bodies inside the ice shell. *Icarus* 237:190–201. <https://doi.org/10.1016/j.icarus.2014.04.026>
- Kirk R, Howington-Kraus E, Hare T, Jorda L (2016) The effect of illumination on stereo DTM quality: simulations in support of Europa exploration. *ISPRS Ann Photogramm Remote Sens Spatial Inf Sci* III-4:103–110. <https://doi.org/10.5194/isprs-annals-III-4-103-2016>
- Kirk RL, Shepherd M, Sides SC (2018) A novel technique for precision geometric correction of jitter distortion for the Europa imaging system and other rolling-shutter cameras. *Int Arch Photogramm Remote Sens Spat Inf Sci XLII-3:735–739*. <https://doi.org/10.5194/isprs-archives-XLII-3-735-2018>
- Kirk RL, Mayer DP, Ferguson RL, et al (2021) Evaluating stereo digital terrain model quality at Mars rover landing sites with HRSC, CTX, and HiRISE images. *Remote Sens* 13:1–40. <https://doi.org/10.3390/rs13173511>

- Koh Z-W, Nimmo F, Lunine JI, Mazarico E, Dombard AJ (2022) Assessing the detectability of Europa's seafloor topography from Europa Clipper's gravity data. *Planet Sci J* 3:197. <https://doi.org/10.3847/PSJ/ac82aa>
- Korendyke CM, Vourlidis A, Plunkett SP, Howard RA, Wang D, Marshall CJ, Waczynski A, Janesick JJ, Elliott T, Tun S, Tower J, Grygon M, Keller D, Clifford GE (2013) Development and test of an active pixel sensor detector for heliospheric imager on Solar Orbiter and Solar Probe Plus. In: *Solar physics and space weather instrumentation V*. SPIE, Bellingham, pp 178–191
- Laura JR, Beyer RA (2021) Knowledge inventory of foundational data products in planetary science. *Planet Sci J* 2(1):18. <https://doi.org/10.3847/PSJ/abcb94>
- Laura J, et al (2023) Integrated Software for Imagers and Spectrometers 7.2.0. Zenodo. <https://doi.org/10.5281/zenodo.2563341>
- Lauretta DS, Balram-Knutson SS, Beshore E, Boynton WV, Drouet d'Aubigny C, DellaGiustina DN, Enos HL, et al (2017) OSIRIS-REx: sample return from asteroid (101955) Bennu. *Space Sci Rev* 212(1):925–984. <https://doi.org/10.1007/s11214-017-0405-1>
- Lauretta DS, DellaGiustina DN, Bennett CA, Golish DR, et al (2019) The unexpected surface of asteroid (101955) Bennu. *Nature* 568(7750):55–60. <https://doi.org/10.1038/s41586-019-1033-6>
- Lees WJ, Centurelli J, Slack K, Turtle Z, Lewis D, Morgan P (2023) Optomechanical design of the Europa Imaging System Wide Angle Camera (EIS WAC). In: *Proc. SPIE 12669, optomechanical engineering 2023*, p 1266906. <https://doi.org/10.1117/12.2679483>
- Leonard E, Senske D, Patthoff D (2021) Analyzing Europa's global geology. In: *AGU Fall Meeting abstracts*, pp P51C-01
- Liu J, Zeng X, Li C, Ren X, Yan W, Tan X, Zhang X, Chen W, Zuo W, Liu Y, Liu B, Liu D, Zhou Q, Ouyang Z (2021) Landing site selection and overview of China's lunar landing missions. *Space Sci Rev* 217(1):6. <https://doi.org/10.1007/s11214-020-00781-9>
- Manga M, Michaut C (2017) Formation of lenticulae on Europa by saucer-shaped sills. *Icarus* 286:261–269. <https://doi.org/10.1016/j.icarus.2016.10.009>
- Mattson S, Robinson M, McEwen A, Bartels A, Bowman-Cisneros E, Li R, Lawver J, Tran T, Paris K, Team L, et al (2010) Early assessment of spacecraft jitter in LROC-NAC. In: *41st Annual Lunar and Planetary Science Conference*, p 1871
- Mattson S, Kirk R, Heyd R, McEwen A, Eliason E, Hare T, Beyer R, Howington-Kraus E, Okubo C, Herkenhoff K (2011) Release of HiRISE digital terrain models to the planetary data system. In: *42nd Annual Lunar and Planetary Science Conference*, p 1558
- Mazarico E, et al (2023) The Europa Clipper gravity and radio science investigation. *Space Sci Rev* 219(30). <https://doi.org/10.1007/s11214-023-00972-0>
- McEwen AS (1986) Exogenic and endogenic albedo and color patterns on Europa. *J Geophys Res, Solid Earth* 91(B8):8077–8097. <https://doi.org/10.1029/JB091iB08p08077>
- McEwen AS (1991) Photometric functions for photogrammetry and other applications. *Icarus* 92(2):298–311. [https://doi.org/10.1016/0019-1035\(91\)90053-V](https://doi.org/10.1016/0019-1035(91)90053-V)
- McEwen AS, Eliason EM, Bergstrom JW, Bridges NT, Hansen CJ, Delamere WA, Grant JA, Gulick VC, Herkenhoff KE, Keszthelyi L, Kirk RL, Mellon MT, Squyres SW, Thomas N, Weitz CM (2007) Mars Reconnaissance Orbiter's High Resolution Imaging Science Experiment (HiRISE). *J Geophys Res, Planets* 112(E5). <https://doi.org/10.1029/2005JE002605>
- McEwen AS, et al (2010) The High Resolution Imaging Science Experiment (HiRISE) during MRO's Primary Science Phase (PSP). *Icarus* 205(1):2–37. <https://doi.org/10.1016/j.icarus.2009.04.023>
- McEwen AS, Janesick J, Elliot ST, Turtle EP, Strohhahn K, Adams E (2012) Radiation-hard camera for Jupiter system science. International workshop on instrumentation for planetary missions, held October 10–12, 2012 in Greenbelt, Maryland. *LPI Contrib* 1683:1041.
- Murchie S, et al (2007) Compact Reconnaissance Imaging Spectrometer for Mars (CRISM) on Mars Reconnaissance Orbiter (MRO). *J Geophys Res, Planets* 112(E5). <https://doi.org/10.1029/2006JE002682>
- Nelessen A, Sackier C, Clark I, Brugarolas P, Villar G, Chen A, Stehura A, Otero R, Stilley E, Way D, Edquist K, Mohan S, Giovingo C, Lefland M (2019) Mars 2020 entry, descent, and landing system overview. In: *2019 IEEE Aerospace Conference*, pp 1–20
- Nelson ML, McCord TB, Clark RN, Johnson TV, Matson DL, Mosher JA, Soderblom LA (1986) Europa: characterization and interpretation of global spectral surface units. *Icarus* 65(1):129–151. [https://doi.org/10.1016/0019-1035\(86\)90068-0](https://doi.org/10.1016/0019-1035(86)90068-0)
- Nelson RM, Smythe WD, Hapke BW, Hale AS (2002) Low phase angle laboratory studies of the opposition effect: search for wavelength dependence. *Planet Space Sci* 50(9):849–856. [https://doi.org/10.1016/S0032-0633\(02\)00059-4](https://doi.org/10.1016/S0032-0633(02)00059-4)
- Nimmo F, Gaidos E (2002) Strike-slip motion and double ridge formation on Europa. *J Geophys Res, Planets* 107(E4):5-1–5-8. <https://doi.org/10.1029/2000JE001476>


- Nimmo F, Schenk P (2006) Normal faulting on Europa: implications for ice shell properties. *J Struct Geol* 28(12):2194–2203. <https://doi.org/10.1016/j.jsg.2005.08.009>
- Nimmo F, Giese B, Pappalardo RT (2003a) Estimates of Europa's ice shell thickness from elastically-supported topography. *Geophys Res Lett* 30(5). <https://doi.org/10.1029/2002GL016660>
- Nimmo F, Pappalardo RT, Giese B (2003b) On the origins of band topography. *Europa Icarus* 166(1):21–32. <https://doi.org/10.1016/j.icarus.2003.08.002>
- Nimmo F, Thomas PC, Pappalardo RT, Moore WB (2007) The global shape of Europa: constraints on lateral shell thickness variations. *Icarus* 191(1):183–192. <https://doi.org/10.1016/j.icarus.2007.04.021>
- Nimmo F, Bills BG, Thomas PC (2011) Geophysical implications of the long-wavelength topography of the Saturnian satellites. *J Geophys Res, Planets* 116(E11). <https://doi.org/10.1029/2011JE003835>
- Nimmo F, Umurhan O, Lisse CM, Bierson CJ, Lauer TR, Buie MW, Throop HB, Kammer JA, Roberts JH, McKinnon WB, Zangari AM, Moore JM, Stern SA, Young LA, Weaver HA, Olkin CB, Ennico K (2017) Mean radius and shape of Pluto and Charon from new horizons images. *Icarus* 287:12–29. <https://doi.org/10.1016/j.icarus.2016.06.027>
- Oberbeck VR, Quaide WL (1967) Estimated thickness of a fragmental surface layer of oceanus procellarum. *J Geophys Res* 72:4697–4704. <https://doi.org/10.1029/JZ072i018p04697>
- Oberst J, Zubarev A, Nadezhkina I, Shishkina L, Rambaux N (2014) The Phobos geodetic control point network and rotation model. *Planet Space Sci* 102:45–50. <https://doi.org/10.1016/j.pss.2014.03.006>
- Ojakangas GW, Stevenson DJ (1989) Thermal state of an ice shell on Europa. *Icarus* 81(2):220–241. [https://doi.org/10.1016/0019-1035\(89\)90052-3](https://doi.org/10.1016/0019-1035(89)90052-3)
- Paganini L, Villanueva GL, Roth L, Mandell AM, Hurford TA, Retherford KD, Mumma MJ (2020) A measurement of water vapour amid a largely quiescent environment on Europa. *Nat Astron* 4(3):266–272. <https://doi.org/10.1038/s41550-019-0933-6>
- Pappalardo RT, Vance S, Bagenal F, Bills BG, Blaney DL, Blankenship DD, Brinckerhoff WB, Connerney JEP, Hand KP, Hoehler TM, Leisner JS, Kurth WS, McGrath MA, Mellon MT, Moore JM, Patterson GW, Prockter LM, Senke DA, Schmidt BE, Shock EL, Smith DE, Soderlund KM (2013) Science potential from a Europa lander. *Astrobiology* 13(8):740–773. <https://doi.org/10.1089/ast.2013.1003>
- Pappalardo RT, et al (2024) Science Overview of the Europa Clipper Mission. *Space Sci Rev* (this collection)
- Paranicas C, Ratliff JM, Mauk BH, Cohen C, Johnson RE (2002) The ion environment near Europa and its role in surface energetics. *Geophys Res Lett* 29(5):18. <https://doi.org/10.1029/2001GL014127>
- Patterson W, McEwen AS, Turtle E, Ernst C, Kirk RL (2019) Data products from the Europa Imaging System (EIS) on Europa Clipper. *Astron Data Anal Softw Syst XXVIII* 523:605
- Perry JE, Heyd R, Read M, Tornabene LL, Sutton SS, Byrne S, Thomas N, Fennema A, McEwen A, Berry K (2022) Geometric processing of TGO Cassini observations. *Planet Space Sci* 223:105581. <https://doi.org/10.1016/j.pss.2022.105581>
- Phillips CB, McEwen AS, Hoppa GV, Fagents SA, Greeley R, Klemaszewski JE, Pappalardo RT, Klaasen KP, Breneman HH (2000) The search for current geologic activity on Europa. *J Geophys Res, Planets* 105(E9):22579–22597. <https://doi.org/10.1029/1999JE001139>
- Phillips CB, et al A reconnaissance strategy for landing on Europa, based on Europa Clipper data. *Planet Sci J*. in review
- Porco CC, West RA, McEwen A, Del Genio AD, Ingersoll AP, Thomas P, Squyres S, et al (2003) Cassini imaging of Jupiter's atmosphere, satellites, and rings. *Science* 299(5612):1541–1547. <https://doi.org/10.1126/science.1079462>
- Porco CC, West RA, Squyres S, McEwen A, Thomas P, Murray CD, Delgenio A, Ingersoll AP, Johnson TV, Neukum G, Veverka J, Dones L, Brahic A, Burns JA, Haemmerle V, Knowles B, Dawson D, Roatsch T, Beurle K, Owen W (2004) Cassini imaging science: instrument characteristics and anticipated scientific investigations at Saturn. *Space Sci Rev* 115(1):363–497. <https://doi.org/10.1007/s11214-004-1456-7>
- Quick LC, Hedman MM (2020) Characterizing deposits emplaced by cryovolcanic plumes on Europa. *Icarus* 343:113667. <https://doi.org/10.1016/j.icarus.2020.113667>
- Quick LC, Barnouin OS, Prockter LM, Patterson GW (2013) Constraints on the detection of cryovolcanic plumes on Europa. *Planet Space Sci* 86:1–9. <https://doi.org/10.1016/j.pss.2013.06.028>
- Rambaux N, Hoolst TV, Karatekin Ö (2011) Librational response of Europa, Ganymede, and Callisto with an ocean for a non-Keplerian orbit. *Astron Astrophys* 527:A118. <https://doi.org/10.1051/0004-6361/201015304>
- Rathbun JA, Spencer JR (2020) Proposed plume source regions on Europa: no evidence for endogenic thermal emission. *Icarus* 338:113500. <https://doi.org/10.1016/j.icarus.2019.113500>
- Rennison J, Dragg J, Morris E, Shoemaker E, Turkevich A (1966) Lunar surface topography. In: Surveyor I Mission Report Part II. Scientific data and results, NASA technical report, vol 32-1023, pp 7–44
- Retherford KD, et al (2024) Europa Ultraviolet Spectrograph (Europa-UVS). *Space Sci Rev* 220
- Rhoden AR, Hurford TA, Roth L, Retherford K (2015) Linking Europa's plume activity to tides, tectonics, and liquid water. *Icarus* 253:169–178. <https://doi.org/10.1016/j.icarus.2015.02.023>

- Rhoden AR, Mohr KJ, Hurford TA, Henning W, Sajous S, Patthoff DA, Dubois D (2021) Obliquity, precession, and fracture mechanics: implications of Europa's global cycloid population. *JGR Planets* 126(3):e2020JE006710. <https://doi.org/10.1029/2020JE006710>
- Roberts JH, et al (2023) Exploring the interior of Europa with the Europa Clipper. *Space Sci Rev* 219:46. <https://doi.org/10.1007/s11214-023-00990-y>
- Roth L (2021) A stable H₂O atmosphere on Europa's trailing hemisphere from HST images. *Geophys Res Lett* 48(20):e2021GL094289. <https://doi.org/10.1029/2021GL094289>
- Roth L, Saur J, Retherford KD, Strobel DF, Feldman PD, McGrath MA, Nimmo F (2014) Transient water vapor at Europa's south pole. *Science* 343(6167):171–174. <https://doi.org/10.1126/science.1247051>
- Ryan KJ, Pool J, Lovelady H, Osterman SN (2018) Design, fabrication, and test of a patterned optical filter array for the Europa Imaging System (EIS). In: Proc. SPIE 10706, advances in optical and mechanical technologies for telescopes and instrumentation III, vol 1070655. <https://doi.org/10.1117/12.2312754>. (10 July 2018)
- Schenk PM (2002) Thickness constraints on the icy shells of the Galilean satellites from a comparison of crater shapes. *Nature* 417(6887):419–421. <https://doi.org/10.1038/417419a>
- Schenk PM, McKinnon WB (2009) One-hundred-km-scale basins on Enceladus: Evidence for an active ice shell. *Geophys Res Lett* 36(16). <https://doi.org/10.1029/2009GL039916>
- Schmidt BE, Blankenship DD, Patterson GW, Schenk PM (2011) Active formation of "chaos terrain" over shallow subsurface water on Europa. *Nature* 479(7374):502–505. <https://doi.org/10.1038/nature10608>
- Sides S, Becker T, Becker K, Edmundson K, Backer J, Wilson T, Weller L, Humphrey I, Berry K, Shepherd M, et al (2017) The USGS Integrated Software for Imagers and Spectrometers (ISIS 3) instrument support, new capabilities, and releases. In: 48th Annual Lunar and Planetary Science Conference, p 2739
- Shoemaker EM, Morris EC (1970) Physical characteristics of the lunar regolith determined from Surveyor television observations. *Radio Sci* 5(2):129–155
- Sparks WB, Hand KP, McGrath MA, Bergeron E, Cracraft M, Deustua SE (2016) Probing for evidence of plumes on Europa with HST/STIS. *Astrophys J* 829(2):121. <https://doi.org/10.3847/0004-637X/829/2/121>
- Sparks WB, Schmidt BE, McGrath MA, Hand KP, Spencer JR, Cracraft M, Deustua SE (2017) Active cryovolcanism on Europa? *Astrophys J* 839(2):L18. <https://doi.org/10.3847/2041-8213/aa67f8>
- Spitale JN, Hurford TA, Rhoden AR, Berkson EE, Platts SS (2015) Curtain eruptions from Enceladus' south-polar terrain. *Nature* 521(7550):57–60. <https://doi.org/10.1038/nature14368>
- Steinbrügge G, Schroeder DM, Haynes MS, Hussmann H, Grima C, Blankenship DD (2018) Assessing the potential for measuring Europa's tidal Love number h₂ using radar sounder and topographic imager data. *Earth Planet Sci Lett* 482:334–341. <https://doi.org/10.1016/j.epsl.2017.11.028>
- Steinbrügge G, Park RS, Roberts JH, Castillo-Rogez JC, Nimmo F, Trinh KT, Tobie G, Bland MT (2023) Geodetic investigations of the Europa Clipper Mission. In: AGU Fall Meeting abstracts, pp P41F-3243
- Sutton SS, Boyd AK, Kirk RL, Cook D, Backer J, Fennema A, Heyd R, McEwen A, Mirchandani S (2019) Correcting spacecraft jitter in HiRISE images. In: Wu B, Di K, Oberst J, Karachevtseva I (eds) Planetary remote sensing and mapping. Taylor & Francis, London, pp 91–106
- Thomas PC (2010) Sizes, shapes, and derived properties of the saturnian satellites after the Cassini nominal mission. *Icarus* 208(1):395–401. <https://doi.org/10.1016/j.icarus.2010.01.025>
- Thomas PC, Tajeddine R, Tiscareno MS, Burns JA, Joseph J, Loredó TJ, Helfenstein P, Porco C (2016) Enceladus's measured physical libration requires a global subsurface ocean. *Icarus* 264:37–47. <https://doi.org/10.1016/j.icarus.2015.08.037>
- Turtle EP, Pierazzo E (2001) Thickness of a european ice shell from impact crater simulations. *Science* 294:1326–1328. <https://doi.org/10.1126/science.1062492>
- Van Hoolst T, Baland R-M, Trinh A (2013) On the librations and tides of large icy satellites. *Icarus* 226(1):299–315. <https://doi.org/10.1016/j.icarus.2013.05.036>
- Vance SD, Craft KL, Shock E, et al (2023) Investigating Europa's habitability with the Europa Clipper. *Space Sci Rev* 219:81. <https://doi.org/10.1007/s11214-023-01025-2>
- Villaneuva GL, Hammel HB, Milam SN, et al (2023) Endogenous CO₂ ice mixture on the surface of Europa and no detection of plume activity. *Science* 381:1305–1308
- Vourlidas A, Howard RA, Plunkett SP, Korendyke CM, Thernisien AFR, Wang D, Rich N, et al (2016) The Wide-Field Imager for Solar Probe Plus (WISPR). *Space Sci Rev* 204(1):83–130. <https://doi.org/10.1007/s11214-014-0114-y>
- White OL, Schenk PM, Nimmo F, Hoogenboom T (2014) A new stereo topographic map of Io: implications for geology from global to local scales. *J Geophys Res, Planets* 119(6):1276–1301. <https://doi.org/10.1002/2013JE004591>
- Wilcox B, Robinson M, Thomas P, Hawke B (2005) Constraints on the depth and variability of the lunar regolith. *Meteorit Planet Sci* 40(5):695–710. <https://doi.org/10.1111/j.1945-5100.2005.tb00974.x>

- Zahnle K, Dones L, Levison HF (1998) Cratering rates on the Galilean satellites. *Icarus* 136(2):202–222. <https://doi.org/10.1006/icar.1998.6015>
- Zahnle K, Alvarellos JL, Dobrovolskis A, Hamill P (2008) Secondary and sesquinary craters on Europa. *Icarus* 194(2):660–674. <https://doi.org/10.1016/j.icarus.2007.10.024>

Publisher's Note Springer Nature remains neutral with regard to jurisdictional claims in published maps and institutional affiliations.

Authors and Affiliations

E.P. Turtle¹  · A.S. McEwen² · G.W. Patterson¹ · C.M. Ernst¹ · C.M. Elder³ · K.A. Slack^{1,4} · S.E. Hawkins¹ · J. McDermott¹ · H. Meyer¹ · R. DeMajistre¹ · R. Espiritu¹ · H. Seifert¹ · J. Niewola¹ · M. Bland⁵ · M. Becker¹ · J. Centurelli¹ · G.C. Collins⁶ · P. Corlies⁷ · H. Darlington¹ · I.J. Daubar⁸ · C. Derr¹ · C. Detelich⁹ · E. Donald^{1,10} · W. Edens¹ · L. Fletcher¹¹ · C. Gardner¹ · F. Graham¹ · C.J. Hansen¹² · C. Haslebacher¹³ · A.G. Hayes⁹ · D. Humm¹ · T.A. Hurford⁴ · R.L. Kirk⁵ · N. Kutsop⁹ · W.J. Lees¹ · D. Lewis¹ · S. London¹ · A. Magner¹ · M. Mills² · A.C. Barr Mlinar¹² · F. Morgan¹ · F. Nimmo¹⁴ · A. Ocasio Milanes¹ · S. Osterman¹⁵ · C.B. Phillips³ · A. Pommerol¹³ · L. Prockter¹ · L.C. Quick⁴ · G. Robbins¹ · J.M. Soderblom⁷ · B. Stewart¹ · A. Stickle¹ · S.S. Sutton² · N. Thomas¹³ · I. Torres⁷ · O.J. Tucker⁴ · R.B. Van Auken^{1,2} · K.A. Wilk^{4,8}

✉ E.P. Turtle
Elizabeth.Turtle@jhuapl.edu

- ¹ Johns Hopkins Applied Physics Laboratory, Laurel, MD, USA
- ² University of Arizona, Tucson, AZ, USA
- ³ Jet Propulsion Laboratory, California Institute of Technology, Pasadena, CA, USA
- ⁴ NASA Goddard Space Flight Center, Greenbelt, MD, USA
- ⁵ U.S. Geological Survey (USGS), Flagstaff, AZ, USA
- ⁶ Wheaton College, Norton, MA, USA
- ⁷ Massachusetts Institute of Technology, Cambridge, MA, USA
- ⁸ Brown University, Providence, RI, USA
- ⁹ Cornell University, Ithaca, NY, USA
- ¹⁰ Main Engineering, Silver Spring, MD, USA
- ¹¹ University of Leicester, Leicester, UK
- ¹² Planetary Science Institute, Tucson, AZ, USA
- ¹³ University of Bern, Bern, Switzerland
- ¹⁴ University of California, Santa Cruz, CA, USA
- ¹⁵ Southwest Research Institute, Boulder, CO, USA